# Engineering Exotic Baths for Superconducting Quantum Circuits Using Parametric Drives

by

**Maria Mucci**

Bachelor of Arts, Boston University, 2017

Submitted to the Graduate Faculty of

the Dietrich School of Arts and Sciences in partial fulfillment

of the requirements for the degree of

**Doctor of Philosophy**

University of Pittsburgh

2024

UNIVERSITY OF PITTSBURGH

DIETRICH SCHOOL OF ARTS AND SCIENCES

This dissertation was presented

by

Maria Mucci

It was defended on

August 1, 2024

and approved by

Michael Hatridge, Department of Physics and Astronomy, University of Pittsburgh

Rachel Bezanson, Department of Physics and Astronomy, University of Pittsburgh

Benjamin Hunt, Department of Physics, Carnegie Mellon University

Roger Mong, Department of Physics and Astronomy, University of Pittsburgh

Thomas Purdy, Department of Physics and Astronomy, University of Pittsburgh

**Engineering Exotic Baths for Superconducting Quantum Circuits Using Parametric Drives**

Maria Mucci, PhD

University of Pittsburgh, 2024

Quantum bits, or qubits, must be coupled to their environmental bath in order for us to measure and manipulate their delicate quantum states. This qubit-bath interaction introduces irreversible decay in superconducting circuits where information is lost to dissipations. While loss and decay are inevitable, loss need not be our enemy. The work described in this thesis focuses on engineering losses and effective baths for quantum systems to, for instance, gain in-situ control of the effective temperature/populations and relaxation rates of a multilevel transmon qubit. We create fully engineered baths where the user can modulate the couplings between qubits and their environment, determining how energy is gained and lost by the qubit through a designed loss channel.

We achieve an engineered qubit-reservoir exchange by dispersively coupling a single transmon qubit to a SNAIL mode. The SNAIL has two functions: first to be the source of three- (and sometimes four-) wave mixing that allows us to drive parametric operations to create and exchange photons among the qubit and SNAIL modes at a rate of our choosing, and second to be a source of loss that converts these coherent processes to controlled heating and cooling of the transmon.

This thesis will highlight two experimental use cases for such a multimode system. First, a fully controllable quantum bath where we can push the qubit towards states with positive, negative, and infinite temperature, and even make 'unnatural' relaxation states such as a transmon that relaxes equally from $|e\rangle$ to $|g\rangle$ and $|f\rangle$. These transmons may have applications in problems like cavity arrays and quantum simulators because the computers that simulate quantum behavior should themselves be quantum mechanical in nature.

Second, we use parametric transmon heating to realize a single-atom micro-maser as a very narrow cryogenic light source. We generate a maser that is emits a narrow bandwidth of high amplitude light with indirect, far-detuned microwave drives that excite our transmon

artificial atom. This is an ideal platform for studying quantum optics in a microwave circuit setting, for instance realizing a recent proposal to build a maser far narrower than the Schawlow-Townes limit.

*To my family*

♡

## Table of Contents

## List of Tables

## List of Figures

## Acknowledgements

As my PhD comes to a close, I only have fond memories because despite the ups and downs, it all came together and I had the time of my life doing it. If you told that to 2017 me taking graduate E&M and moving to a new city without any friends or family, or 2022 me in the throes of broken experiments and broken spirits, I wouldn't have believed you. Yet here I am, finally at the end, and all I can do is look back and feel proud and happy that I went through it all.

It truly does take a village. My growth as a scientist and as a person has largely been shaped by the people mentioned here, and I would be remiss if I didn't thank them all. The day I met Professor Michael Hatridge was the day I decided I was doing this quantum thing. He has fostered an environment of caring deeply about what you do, an unrelenting dedication to science, and the importance of grit. I thank him for the countless times he has pulled us out of equipment failure, mismatched fonts, confusion on scientific concepts both minor and major, and desperate attempts at making experiments work. Michael makes us strive for better because we can see him doing the same. It's hard to not enjoy what you do when your advisor is also having fun in the lab. I am also grateful for Michael's personal support through some rough times in my life. I haven't used my 'bail out of jail only once' card but I have used the 'make sure she's not dying' card more times than I would care for.

I thank Professor David Pekker for leading the theory efforts for my projects and for working with what we have, rather than what we don't. He can quickly catch a $2\pi$ error and turn a coffee conversation into a PhD project. I would like to express thanks to my graduate committee for their time and efforts: Professors Rachel Bezanson, Benjamin Hunt, Roger Mong, and Thomas Purdy. Additionally, I am very grateful to our wonderful machine shop for making all of our projects come to life and providing above and beyond help to our lab. In particular I thank Bill Strang, Jeff Tomaszewski, and Shawn Artman.

The Hatlab has fortunately been home to many wonderful scientists that I am lucky to call my colleagues and friends. Gangqiang Liu is thorough and thoughtful in his actions and led by example as our post doc. His 'tsk'-ing is highly effective at curbing mistakes. Olivia Lanes taught me how to manage people performing different tasks to come together as a whole, as well as provided solid advice for navigating graduate school, the lab, and being

an adult. My bad choices are the reason the brown water came out. Tzu-Chiao Chien can adapt and help in any situation you throw him while remaining encouraging and smiling throughout. His favorite color is purple, duh. Xi Cao taught me how to be a researcher. He is deliberate in what he says and does, is highly organized, and thinks before acting. He let me try even if it slowed us down and I am eternally grateful for the opportunity to learn.

Pinlei Lu is the most enthusiastic person I have met in the lab. When I first joined he was leaving the theory world, and it was great to watch him quickly become an excellent experimentalist. Chao Zhou is the physicist we should all strive to be. He is patient, sees tasks through to the end no matter the timeline, and able to keep a lot going on at once. Both Pinlei and Chao (maybe one learned it from the other or they were destined to work together) can give you these powerful looks that tell you it's time to stop doing wrong things.

Ryan Kaufman is always happy to work through any problem, even a silly lunch conversation. It was impressive to watch him quickly stand on his own and lead our lab's amplifier team. Mingkang Xia makes his moves in silence, but they are powerful. He can diagnose and fix your problem before you even knew you had one. Our lab's fabrication efforts would not have grown without Param Patel. He gets things done and is willing to try whatever crazy science idea is presented to him.

Israa Yusuf is the hardest working graduate student I know. It's not uncommon to find her working at any hour of the day or night. She taught me to be more flexible and open to change, and I am grateful for her patience and friendship. Boris Mesits is a reminder that you should have hobbies and talents outside of the lab. Yet he still puts in the hours and can juggle multiple experiments at once. Jake Repicky stepped into the role of post doc and quickly picked up the ways of the lab. He has the tough job of herding us cats and whatever facilities problem arises, but remains compassionate and caring for those around him. Evan McKinney is genuinely excited to learn something new. He serves as a reminder that we should never stop being curious and that collaboration is the key to success and innovation. Maria Nowicki is a team player, organized, and three steps ahead of you. Whatever you're about to say, she's already thought, analyzed, and set into motion. I appreciate her candor, warmth, and help in times of need.

Girish Kumbhar can pick up concepts and skills quickly. He is eager to learn and con-

tribute his time to helping the lab. Gaurav Agarwal has happily taken on all of the many tasks assigned to him and willing to offer a helping hand with whatever comes his way. His insight is always much appreciated. Last but not least, Chun-Che Wang has dutifully taken on the maser project and ran with it. He can always point out a different way of thinking about a problem and an efficient solution. I am grateful for his hard work, willingness to listen, and help in carrying out whatever antics I come up with.

My family has been hugely supportive throughout my entire life, especially so during this endeavor. I would not be where I am in life without their love and encouragement in all that I do. My parents, Paula and David Mucci, have given me every opportunity in the world and I am so grateful for their years of continual hard work. My mom is selfless, a go-getter, and reminds me every day to get back up. My dad believes in me when I don't believe in myself and has a fix for everything. I appreciate both of your perspectives on my best and worst days. My sister Alexandra is the smartest person I have ever met and perfect in every way. That is not a biased statement. Thank you for being my best friend. My brother Louis is the hardest worker I know and cares so deeply for his friends and family. Thank you for reminding me to enjoy life and those in it. Finally to Dr. Anthony Lovat. Thank you for listening to every thought that crosses my mind and bringing endless laughter to my life. I am so grateful for you taking a leap of faith, and letting me be me and you be you. I love you all dearly. Thank you.

## List of Abbreviations

| | |
|---|---|
| AC | alternating current |
| ADC | analog to digital converter |
| AWG | arbitrary waveform generator |
| CQED | Cavity quantum electrodynamics |
| cQED | Circuit quatnum electrodynamics |
| DAC | digital to analog converter |
| DC | direct current |
| EPR | energy participation ratio |
| FWHM | full width at half maximum |
| HEMT | high electron mobility transistor |
| HFSS | high frequency structure simulator |
| JJ | Josephson junction |
| JRM | Josephson ring modulator |
| QHO | quantum harmonic oscillator |
| QND | quantum non-demolition |
| QuTiP | quantum toolbox in python |
| RF | radio frequency |
| RWA | rotating wave approximation |
| SC | superconducting |
| SEM | scanning electron microscopy |
| SNAIL | Superconducting Nonlinear Asymmetric Inductive eLement |
| SQUID | Superconducting Quantum Interference Device |
| STL | Schawlow-Townes limit |
| Transmon | transmission line shunted plasma oscillation |
| TWPA | Travelling Wave Parametric Amplifier |
| VNA | Vector network analyzer |

## List of Symbols

| | |
|---|---|
| $a$ | annihilation mode operator |
| $a^\dagger$ | creation mode operator |
| $\alpha_q$ | transmon anharmonicity |
| $\alpha_s$ | SNAIL inductive energy ratio |
| $C$ | Capacitor |
| $\gamma_d$ | drive frequency detuning |
| $\Gamma_c$ | cavity linewidth |
| $\Gamma_{ij}$ | rate of transition from state $i$ to state $j$ |
| $\delta$ | parametric cooling process |
| $\|e\rangle$ | qubit excited state |
| $E_C$ | capacitive energy |
| $E_J$ | Josephson energy |
| $f_i$ | frequency of $i^{\text{th}}$ mode $= 2\pi\omega_i$ |
| $\|f^+\rangle$ | qubit second excited state and all levels beyond |
| $g_{ij}$ | direct energy exchange rate for modes $i$ and $j$ |
| $\|g\rangle$ | qubit ground state |
| $H_{JC}$ | Jaynes-Cummings Hamiltonian |
| $I_c$ | critical current |
| $\kappa_i$ | decay rate for $i^{\text{th}}$ mode |
| $K$ | Kelvin |
| $L$ | Inductor |
| $L_J$ | Josephson inductance |
| $\|n\rangle$ | Fock basis eigen state |
| $\langle n\rangle$ | mean photon number |
| $P_c$ | power amplitude of cavity |
| $Q_{int}$ | internal quality factor |

| | |
|---|---|
| $Q_{ext}$ | external/coupling quality factor |
| $Q_{tot}$ | total quality factor = $(\sum \frac{1}{Q_l})^{-1}$ for all loss channels |
| $Q_{ZPF}$ | zero-point fluctuation charge |
| $\Sigma$ | parametric heating process |
| $T$ | temperature |
| $\Phi_{ZPF}$ | zero-point fluctuation phase |
| $V$ | voltage |
| $\rho$ | density operator |
| $\omega_i$ | angular frequency of $i^{\text{th}}$ mode |

## List of Constants

| | |
|---|---|
| $e$ | electron charge — 1.602176634 x $10^{-19}$ C |
| $h$ | Planck's constant — 6.62607015 x $10^{-34}$J s |
| $\hbar = \frac{h}{2\pi}$ | reduced Planck's constant —1.054571817 x $10^{-34}$J s |
| $k_B$ | Boltzmann's constant — 1.380649 x $10^{-23}$ J $K^{-1}$ |
| $\Phi_0 = \frac{h}{2e}$ | magnetic flux quantum — 2.067833848 x $10^{-15}$ Wb |
| $\varphi_0 = \frac{\Phi_0}{2\pi}$ | reduced magnetic flux quantum — 3.291059784 x $10^{-16}$ Wb |

# 1.0 Introduction

## 1.1 The Principles of Quantum Computing

Classical computers have come tremendously far and are now a vital part of our everyday lives. Transistors are the building blocks for classical computers and work to control current and voltage flow, gate signals, and amplify in an integrated circuit using binary states 0 and 1. The problems we ask classical computers to solve are relatively simple and can be broken down into addition, subtraction, multiplication, and division of binary strings. However if the problem became too great in size or complexity, the computer hardware would have to follow. Yet even in some cases, the problem is still too great to be solved with semiconductor transistors. This motivates the need for a computer that can go beyond present computational limits - one that uses the laws of quantum mechanics to solve problems probabalistically with exponential speedup [3].

The basis for a quantum computer is the quantum bit, or qubit, whose state is probabilistic and may be entangled with other qubits and/or in a superposition of many states. A qubit's wave function which defines its states and behaviors as $|\Psi\rangle = \alpha\,|g\rangle + \beta\,|e\rangle$ shows the probabilities of a measurement resulting in its ground state $|\alpha|^2$ and excited state $|\beta|^2$. When an observer performs a measurement, the qubit wave function collapses to one of the definite eigen states $|g\rangle$ or $|e\rangle$ [4]. In all future measurements, where no further actions are taken on the qubit, the qubit will remain in whatever state it collapsed to. This change to the qubit state upon measurement is one of the fundamental laws of quantum mechanics. A two qubit system has a joint wave function $|\Psi\rangle = c_{gg}\,|gg\rangle + c_{ge}\,|ge\rangle + c_{eg}\,|eg\rangle + c_{ee}\,|ee\rangle$, where we now see a computational basis with a total of four basis states and four probability coefficients that can be used within an algorithm. The available size of the computational basis, or the Hilbert space we may span, goes as $2^N$ for $N$ qubits. This exponential increase in space means that with more qubits, more computations may be performed as the quantum system evolves. These computations must be specially formulated to be worth performing on quantum hardware, creating the need for quantum gates and smart algorithm design.

Quantum gates are logical transformations of one or more pieces of information that rotate the system's state vector. Along some new axis, further rotations may be performed to achieve a desired final state which elucidates the intended outcome. Multiple gates may be sequenced together in a quantum algorithm, where input information of qubits is churned through to produce output information [5]. Algorithms must be carefully designed to produce speed up over classical systems, and usually rely on the superpositions and entanglements of multi-qubit systems. One such example was proposed by Feynman who argued that complex systems can be modeled with a quantum computer [6]. Specifically, the components of a computer used to simulate and model an inherently quantum mechanical problem should also scale and behave like that system.

Building a useful and robust quantum computer is no easy feat. The problem of noise must be addressed. Because qubits are probabilistic, they cannot filter out noise in the same way a classical bit would, because classical bits are collapsed to 0 or 1 by simply considering which state its voltage is closer to despite any additional noise. Superposition of qubit states means that one cannot simply take a nearest-state guess. Noise can be dealt with in quantum systems by decreasing the coupling to noise sources such as control electronics and the environment. Qubits have finite information lifetimes which limit the number of faithful, high fidelity gates we may perform before losing quantum coherence completely. Additionally, because of the measurement collapse postulate, we require many logical qubits to carry a large amount of information. These qubits must be well understood, interconnected, and readily controllable by users in a laboratory [7].

## 1.2 Quantum Baths

The quantum systems built for computation can take on many modalities, including superconducting circuits and the circuit QED platform [8]. These circuits operate by driving microwave signals to manipulate and measure the superconducting circuit at cryogenic temperatures. Circuit QED allows for strong interactions between the qubits, cavities, and other circuit elements that make up such a system where microwave frequency photons are the

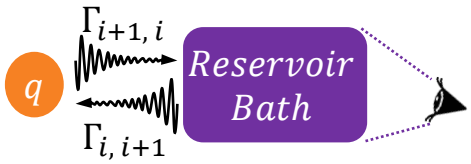


Figure 1: **Bath engineering** A generic mode $q$ exchanges information with a reservoir, losing information at rate $\Gamma_{i+1,i}$ and gaining energy at rate $\Gamma_{i,i+1}$. The bath is directly observed, so all $q$ interactions are mediated through this bath coupling.

quanta of energy. This means that all other degrees of freedom, including phonons, should not participate in our system. Rather, qubits are readily coupled and entangled with the elements around them, including their environment.

A circuit's bath is made up of the channels that couple to its modes, which typically describes the ambient environment or mode structure that the circuit is embedded in and interacts with. This means the reservoir with which our circuit interacts becomes, itself, a mode in the circuit. These couplings can be weak or strong and are the source of noise and loss that create finite coherence times in quantum memories. In superconducting quantum circuits, our qubits are embedded in larger circuits that include one or more cavities, transmission lines, tunable couplers, and even other qubits. The elements made of superconductors and Josephson junctions are themselves inherently lossless. However, examples of some sources of loss are their couplings to their transmission lines, cables leading to the sample, magnetic flux bias lines, defects in their composition, and excessive heating. Qubits' wave functions collapse with these unmonitored channels, making information lost to the observer. The total rate of information transfer into or out of a particular state is the sum of each loss channel's individual rate.

Figure 1 shows how a mode $q$ thermalizes with its bath. It gains energy at rate $\Gamma_{i,i+1}$ for the rate of transfer between adjacent levels $i$ and $i+1$, and loses energy at rate $\Gamma_{i+1,i}$. Thermalization occurs because of the bath coupling. The reservoir is lossy and measured, causing a non-zero overlap of the mode $q$'s wave function and the reservoir's wave function,

leading to irreversible loss in $q$ with dissipations to the bath.

Qubits cannot be completely decoupled from their environment. An isolated qubit would live infinitely long, but be useless for any quantum computing application if we cannot access its information. We would prefer all of the information of a system come back to a single photon detector, but inevitably some is lost to bath channels we cannot monitor.

Heat is a source of loss in a circuit. If the effective mode temperature is not 0, a qubit will not be found in its ground state, have decreased lifetimes, and we will see a degradation in gate fidelities. This means information is lost or dissipated to the hot environment which we cannot control or read. We can measure the probability of the qubit being in a state $n$ at some time as:

$$P_n = \frac{e^{-E_n/k_BT}}{Z} \tag{1}$$

where $Z$ is the partition function:

$$Z = \sum_{n=1}^{N} e^{-E_n/k_BT}. \tag{2}$$

This means that for mode temperatures $|T| > 0$, qubits will thermalize to energy states $E_n > 0$, which is not ideal for most experiments where we want excitations to be deliberate and controlled. Harmonic oscillators at frequency $\omega$ should ideally be operated in the limit

$$\hbar\omega \gg k_BT \tag{3}$$

where $T$ is low enough to freeze out all degrees of freedom except photon excitations. In this ideal limit, qubits should cool naturally to their ground state. Notable examples that violate this property are low frequency transmons and fluxonium qubits [9, 10]. For the majority of experiments, however, we strive for a lossless and efficient circuit to avoid unwanted system-bath couplings.

### 1.3 Engineering Exotic Baths for Transmons

We cannot, realistically, completely uncouple our qubits from their bath. In fact, we can use this loss as a controllable mode of the circuit, making it a resource to fully characterize our quantum system. An engineered bath is one that obeys some manufactured set of loss operations or Lindbladian. Bath engineering has become increasingly important as computers have become more complex and robust to noise. We should be able to detect and stabilize a qubit's state, despite decoherence [11]. The short time scales needed to perform gates means we should also be able to create states quickly and with high fidelity, despite the bath's initial conditions [12]. We may use designed qubit dissipations to determine how our qubits decay, or rather at what rate they thermalize from $|g\rangle$ to $|e\rangle$, $|e\rangle$ to $|g\rangle$, and so on. Additionally, we may determine the population occupancy per state in a multi-level qubit. This is achieved with a handful of broad-band microwave drives which induce parametric mixing processes and a deliberate dump mode. This dump mode is not monitored, but it does not have to be because the qubit's rates and populations inform us of the bath states.

If a system were physically heated just right, and we waited long enough, we could achieve population configurations and temperatures within the standard relaxation model of the transmon. This means the qubit would be populated starting from state $|i\rangle$, and all states $|i+1\rangle, |i+2\rangle ...$ would be filled with probabilities determined by Eq. 1. The rates of settling to this distribution would be entirely set by the uncontrolled temperature of the bath. However, a fully engineered bath would allow us to create population distributions at chosen rates, without hoping for the right ambient conditions to achieve the desired state. We can achieve all of the scenarios shown in Fig. 2 by altering the effective temperature and deciding exactly which levels get filled.

We can change how our qubits couple to this bath and exchange energy with it. In the following chapters, we will explore how to engineer these couplings in a controllable way, making our qubit gain and lose energy from its bath coupling at a rate and final steady state of our choosing. The methods presented in this thesis do not work to decrease total exchange rates (and thus increase mode lifetimes) but rather to increase the exchange rates to build a final configuration faster than it would have settled to if left alone, or

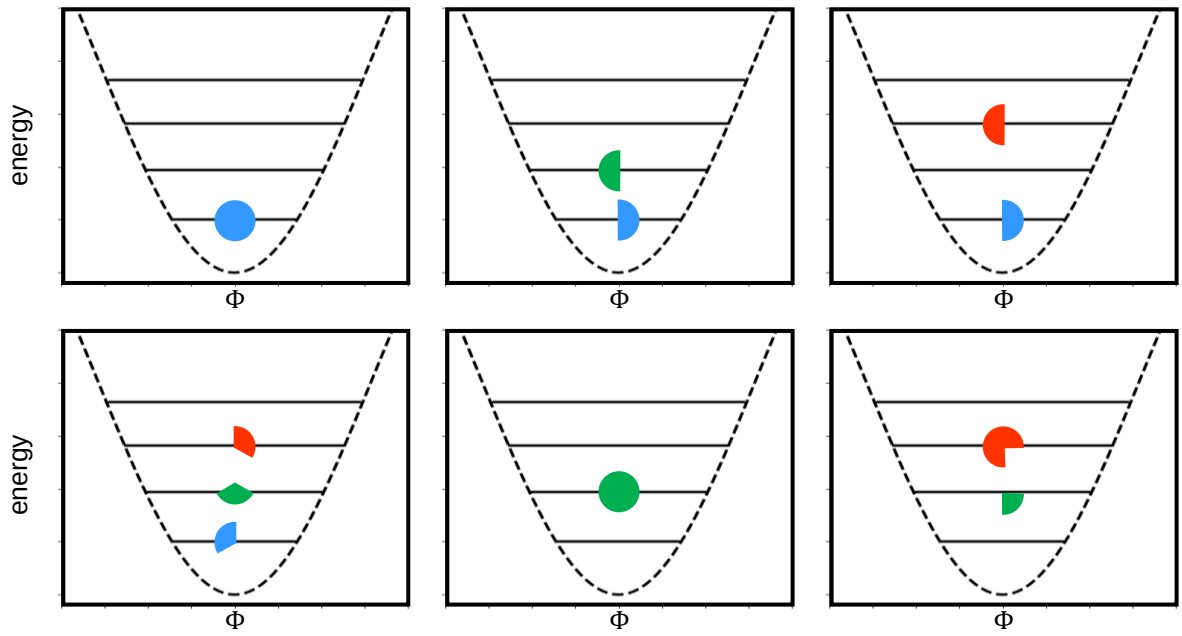


Figure 2: **Exotic transmon relaxations** The transmon anharmonic level structure allows us to uniquely specify the eigen energies of the multi-level qubit. The relaxations of the transmon do not need to follow the standard Boltzmann model. We may design any of the configurations shown with varying parametric drives and engineered loss.

sometimes to a configuration that is completely outside the transmon's standard relaxation model. Crucially, we invert our transmon's population, maintaining its population in $|e\rangle$ with parametric drives.

### 1.4 Masers and the Standard Quantum Limit

Masers and lasers are ubiquitous in physics as bright and highly coherent light sources. They are typically made of many, naturally occurring atoms or molecules pumped into

a population inverted $\lambda$ level structure and feed excitations to a cavity with stimulated emission. In our cQED platform, however, we can build a single atom maser that does not use stimulated emission at all.

Our maser will be built with a transmon qubit that is population inverted by a parametric three-wave mixing process. With the same techniques learned in creating exotic transmon states, we apply a broad parametric pump plus engineered loss to thermalize the transmon to $|e\rangle$. This excited transmon, or our artificial atom, directly exchanges energy with a high Q cavity and continuously feeds it a resonant photon. Light will come out of the cavity through this indirect driving scheme at $\Gamma_c^{masing}$, a significantly narrower linewidth than the cavity's natural response. The Standard Quantum Limit for maser linewidth is set by quantum mechanics. Uncertainty in the energy or phase in the maser causes a large divergence in its random walk through phase space. We can only be so certain about the state of the atoms or the cavity at any given time, leading to a lower limit on linewidth:

$$\Gamma_c^{\text{masing}}(STL) = \frac{\Gamma_c}{4\langle n \rangle}. \tag{4}$$

for bare cavity linewidth $\Gamma_c$ and mean photon number $\langle n \rangle$.

Cryogenic light sources are a valuable tool to have in quantum circuits because they allow us to drive cold systems with cold light. Superconducting cQED experiments are mounted at the base stage of a $^3$He/$^4$He dilution refrigerator near the $1-10$ GHz range. Experimentalists send in signals and drives from room temperature through heavily attenuated and filtered lines, which interact with the sample and come back out of the fridge for interpretation. Despite the filtering measures taken, the light coming down the fridge is full of hot, noisy photons.

The maser we create takes these noisy 300 K drives and cleans them up to produce highly coherent light in the cavity. The cavity itself is not directly driven, but instead the only drive is through the parametrically pumped SNAIL, which inverts the qubit population, which then exchanges energy with the cavity. The SNAIL accepts a broad band of drive frequencies and amplitudes. The light that comes out of the cavity through the masing process (Sec. 3.2.3.1) can be narrowed to

$$\frac{\Gamma_c^{\text{masing}}}{2\pi}(\text{minimum}) = 57.67 \text{ Hz} \tag{5}$$

down from $\frac{\Gamma_c}{2\pi} = 10 - 25$ kHz measured on the VNA when the masing process is turned off. Not only can we measure the maser's steady state response, but we can also measure it on time scales much shorter than its parametrically increased coherence time. This allows us to understand the maser's evolutionary dynamics and track its output to be used as a cryogenic light source.

## 1.5 Organization of Thesis

This dissertation will provide an in-depth look at two major projects with bath engineered superconducting qubits. I will begin in Chap. 2 with an overview explanation of circuit QED, and within that framework how superconducting quantum circuits can arise, leading to the transmon [13] and SNAIL [14]. The transmon and SNAIL will be coupled via parametric three-wave mixing, Sec. 2.2. With this foundation, Chap. 3 will describe the theory driving our method of bath engineering for transmons in Sec. 3.1 and the mathematical formalism that allows us to be able to write a chemical potential for photons. Next in Sec. 3.2 I walk through our motivation for single atom masing and the theory used to construct one. Both theories rely on parametric drives and non-unitary dissipations. In Chap. 4 the results from our bath engineering project will be explained in full, where transmon relaxations like those shown in Fig. 2 are created with variations to drive conditions. This is followed by experimental results from the maser in Chap. 5, where I will show how drive and bias conditions greatly alter the maser's output. Both chapters on experiment data provide information on the numerical and microwave simulations performed in preparation for laboratory measurements, as well as the steady state frequency response diagnostic measurements taken to characterize our circuits. Finally in Chap. 6 I will conclude with a discussion on both of my major projects, bath engineering, and parametric three-wave mixing, as well as provide suggestions for follow up studies using the flexible circuits we have built.

## 2.0 circuitQED, Superconducting Circuits, and Parametric Mixing

### 2.1 circuit QED and Superconducting Qubits

Cavity quantum electrodynamics (CQED) is the study of atoms/particles interacting with reflective cavities. The Nobel Prize in Physics was awarded in 2012 for the study of open quantum systems using cavities to manipulate the states of light generated, entangled, and swapped amongst modes, despite spontaneous emission [15]. This inspired the field of circuit QED (cQED) [8]. In cQED, artificial atoms are coupled to superconducting quantum circuits. This departure from naturally occurring atoms or molecules means that circuit modes are created by the cumulative properties of its components and are far more readily engineered in the laboratory. The mode structure, inter-element interactions, and loss properties of the circuit are all designed, rather than innate properties of particular atomic species. Figure 3 shows how atom-cavity CQED is logically transformed to artificial atom-cavity in cQED.

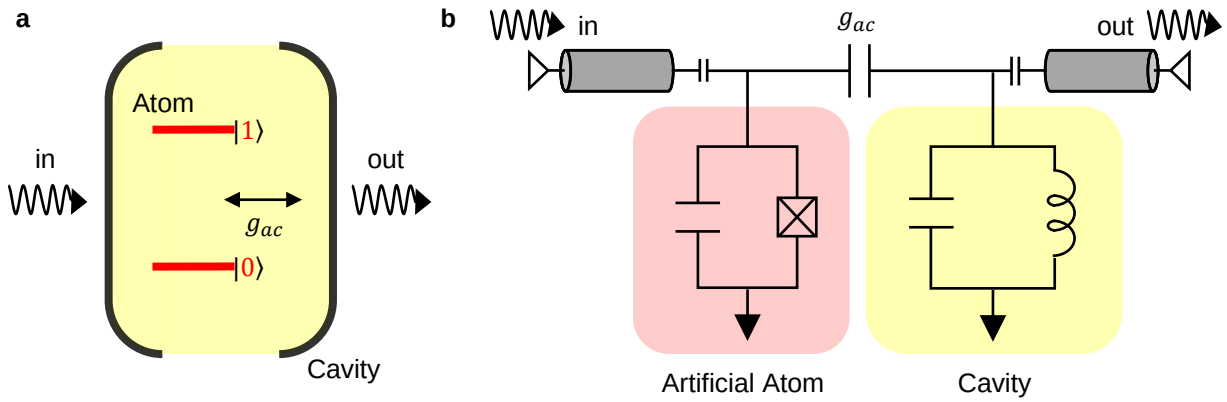


Figure 3: **CQED to cQED** (a) An atom couples to a reflective cavity so its emission is captured by the cavity rather than lost to the outside world. (b) In circuit QED, the same principle applies to artificial atoms. The circuit diagram shown reflects the components that make up such a system.

With the advent of cQED came a rich landscape of theory and experimental work that has established superconducting circuits as a strong platform for quantum computing, with many companies devoting their efforts and resources towards SC qubits [16, 17, 18] and as a large portion of the United States' $968 million dollar budget for quantum research in 2024 [19] going towards academic and national laboratories as well as industry ventures.

These circuits are typically made from capacitors, inductors, transmission lines, and Josephson junctions (Sec.2.1.1) and arranged in countless ways to build unique experiments. We avoid resistive elements because they dissipate heat. Superconducting qubit experiments are operated at the base stage of $^3$He/$^4$He dilution refrigerators, which typically reach $\approx$ 20 mK, well below the superconducting critical temperatures of the materials circuits are comprised of. In this thesis, all circuits described are made of aluminum with $T_c = 1.2$ K and/or tantalum with $T_c = 4.4$ K.

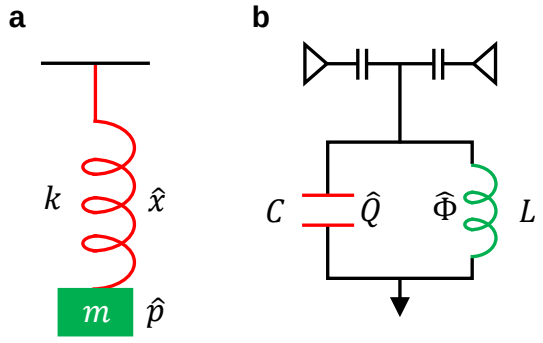


Figure 4: **Harmonic Oscillators** (a) A mass suspended on a spring has a harmonic oscillatory response with both a kinetic and potential energy term. Its Hamiltonian is quadratic in both momentum $\hat{p}$ and position $\hat{x}$. (b) A quantized circuit made of a capacitor and inductor has the same harmonic eigenmode structure and Hamiltonian quadratic in charge operator $\hat{Q}$ and phase operator $\hat{\Phi}$.

Cavities or resonators that form harmonic oscillators for storage and readout are one of the simplest models in cQED with analogs in CQED and classical physics, see Fig. 4. Capacitors (C) and inductors (L) together form a quantum harmonic oscillator with linearly spaced energy levels. In a chosen frame, the oscillator degrees of freedom are the charge

on the capacitor ($\hat{Q}$) and current in the inductor ($\hat{I}$) which vary sinusoidally with time. Its behavior is the same as that of a simple harmonic oscillator mass-spring system, where the potential energy takes a parabolic form and eigen energies are linearly spaced at frequency $\omega_{QHO}$. In this thesis these QHOs, or resonators or cavities, will be realized in both three and quasi-two dimensions. In the basis where flux is the canonical coordinate variable and charge the conjugate momentum [20], with flux across the inductor $\hat{\Phi}$ and charge difference on the capacitor $\hat{Q}$:

$$H_{LC} = \frac{1}{2C}\hat{Q}^2 + \frac{\hat{\Phi}^2}{2L} \tag{6}$$

with the commutation relation $[\hat{\Phi}, \hat{Q}] = i\hbar$. In the frame of quantized single excitations, it is often more intuitive to understand the circuit using raising $\hat{a}^\dagger$ and lowering $\hat{a}$ operators. For a mode $a$ this can be written as:

$$H_{LC} = \hbar\omega_a(\hat{a}^\dagger\hat{a} + \frac{1}{2}) \tag{7}$$

where we can write $\hat{\Phi}$ and $\hat{Q}$ in terms of quantized raising and lowering operators:

$$\hat{\Phi} = \Phi_{ZPF}(\hat{a}^\dagger + \hat{a}) \tag{8}$$

$$\hat{Q} = iQ_{ZPF}(\hat{a}^\dagger - \hat{a}) \tag{9}$$

with zero-point fluctuation phase $\Phi_{ZPF} = \sqrt{\frac{\hbar}{2\omega_a C}}$, charge $Q_{ZPF} = \sqrt{\frac{\hbar\omega_a C}{2}}$, and frequency $\omega_a = \frac{1}{\sqrt{LC}}$. The raising and lowering operators follow the commutation relation $[\hat{a}, \hat{a}^\dagger] = 1$. We define the number operator $\hat{N} = \hat{a}^\dagger\hat{a}$ with eigenvalues for Eq. 7 as $\hbar\omega_a n$ for state $|n\rangle$. This shows how the energy difference between any two adjacent levels is universally $\hbar\omega_a$, shown in black in Fig. 6.

Evenly spaced energy levels are not very useful for information science. If energy is pumped into or emitted by the circuit at frequency $\omega_a = \omega_{01} = \omega_{12}, ...$, we do not know what this excited or was produced by. We need unique microwave frequency signatures for each quantum of energy. In superconducting circuits, we achieve this with the Josephson junction.

### 2.1.1 The Josephson Junction

Josephson tunnel junctions are weak links formed by Cooper pairs of electrons that quantum mechanically tunnel through the barrier created by separating two superconducting islands with a thin insulating barrier [21]. This type of junction, called an SIS (superconductor-insulator-superconductor), is commonly made from (Al-AlOx-Al), see Fig. 5(b). Josephson's model predicted a DC current at zero voltage, proportional to a critical current value and sinusoidally dependent on the phase across the interface. It also predicted an AC current under DC driving at a frequency proportional to this voltage. The DC Josephson effect establishes the current-phase relation, or first Josephson relation:

$$I_J(t) = I_c \sin\varphi(t) \quad \text{(Josephson relation 1)} \tag{10}$$

for critical current $I_c$ and time dependent phase across the junction $\varphi(t) = \frac{2\pi}{\Phi_0}\Phi(t)$. The critical current is the maximum current of Cooper pairs that can tunnel through the junction based on geometry and composition of the superconductor. It is defined as $I_c = \frac{2e\hbar n_0^2}{m_{CP}L}A$ for cross-sectional area A, Cooper pair density $n_0$, tunnel length $L$, $2e$ for the Cooper pair charge, and Cooper pair mass $m_{CP}$ [22]. The superconducting flux quantum is $\Phi_0 = \frac{h}{2e}$. The AC Josephson effect is found by taking the time derivative of the phase across the junction, in the voltage-phase or second Josephson relation:

$$\frac{\partial\varphi}{\partial t} = \frac{2\pi}{\Phi_0}V \quad \text{(Josephson relation 2)} \tag{11}$$

which shows that an applied voltage across the junction leads to an increase in phase difference. This highlights why JJs are often used as sensitive voltage readers. Inductance is related to voltage and current through the instantaneous relation $v = L\frac{di}{dt}$:

$$L(\varphi) = \frac{\Phi_0}{2\pi I_c}\frac{1}{\cos\varphi} = \frac{L_J}{\cos\varphi} \tag{12}$$

where we define the Josephson inductance $L_J = \frac{\Phi_0}{2\pi I_c}$. The introduction of a $\cos\varphi$ in the inductance makes this circuit element nonlinear. Additionally the energy can be written as:

$$E_J = \frac{\Phi_0 I_c}{2\pi} \tag{13}$$

which is the energy to store one flux quantum in the inductor.

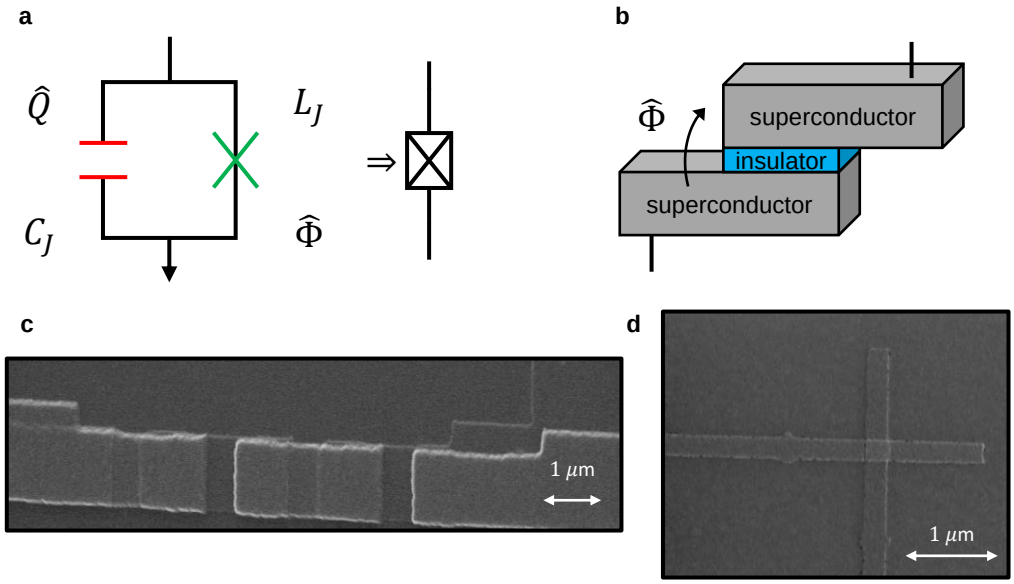


Figure 5: **The Josephson junction** (a) Josephson junctions are represented by Xs in circuit diagrams and the surrounding box means the diagram includes both the nonlinear inductance and Josephson capacitance. (b) They can be formed by sandwiching a thin insulating layer between two superconductors to make a weak tunnel barrier. Two possible ways to fabricate Josephson junctions in the laboratory are in a 'Dolan bridge' (c) or 'bridge free' (d) geometry. Multiple junctions may be fabricated in both series and parallel. (c) SEM of 3 successive Dolan junctions, formed by suspended bridges of aluminum, shown in the middle three squares. Under this top layer of aluminum, there is a thin barrier of aluminum oxide, and below that a second layer of aluminum. (d) SEM of a single bridge-free junction formed at the crossing of the streets (left to right) and avenues (top to bottom). Imaged by Param Patel.

### 2.1.2 The Transmon

These junctions can be inserted into LC circuits to introduce nonlinearity. Historically, the charge qubit (in the form of a Cooper Pair Box) was the first system to demonstrate qubit coherence with Rabi oscillations [23, 24], but it suffered from uncontrollable charge

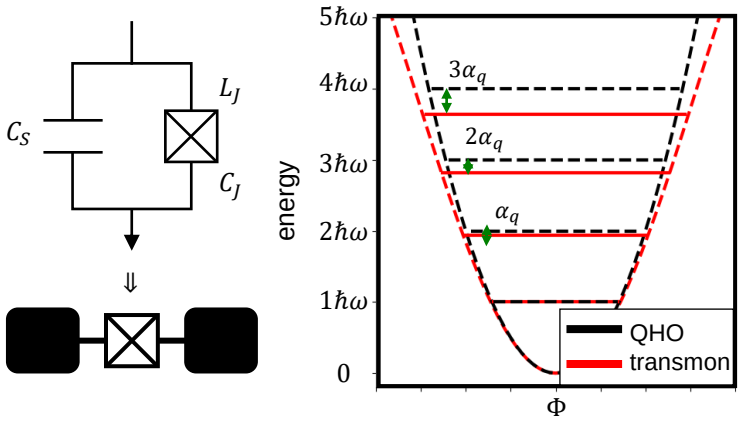


Figure 6: **The transmon** The transmon is formed by shunting a Josephson junction with a large capacitor $C_S$. This qubit has a weakly anharmonic mode structure and is insensitive to fluctuations in charge. The transmon's eigen energies are plotted in red as a stretched parabola, while the energies of a linear quantum harmonic oscillator are plotted in black. The harmonic oscillator has evenly spaced energy levels so we cannot distinguish one excitation from another. The transmon, however, has energy levels that differ by anharmonicity $\alpha_q$ which removes energy degeneracy.

noise. The transmon [13] was developed as a charge qubit with exponentially suppressed charge dispersion (making it insensitive to charge noise) due to a large shunting capacitance and ratio of inductive to capacitive energies $\frac{E_J}{E_C} = 50$ for capacitive energy $E_C = \frac{e^2}{2C_{total}}$, see Fig. 6. Transmons are typically fabricated to operate at a few GHz, set by the geometry of the shunt and Josephson junction. With this $\frac{E_J}{E_C}$ ratio, the transmon maintains anharmonicities $\approx -200$ MHz which is sufficient to lift the degeneracy of the QHO model to make an effective two level qubit.

The transmon Hamiltonian can be approximated for charge number operator $\hat{N}$ and small $\hat{\varphi}$, where the anharmonicity of the transmon is apparent:

$$\hat{H}_{\text{transmon}} = 4E_c\hat{N}^2 + \frac{1}{2}E_J\hat{\varphi}^2 - E_J(\cos\hat{\varphi} + \frac{1}{2}\hat{\varphi}^2) \tag{14}$$

and further approximating by taking a Taylor expansion on the $\cos\hat{\varphi}$ term:

$$\hat{H}_{\text{transmon}} = 4E_c\hat{N}^2 + \frac{1}{2!}E_J\hat{\varphi}^2 - \frac{1}{4!}E_J\hat{\varphi}^4 + ... \tag{15}$$

with typical truncation out to fourth order in $\hat{\varphi}$. Now we define the raising $\hat{q}^\dagger$ and lowering $\hat{q}$ operators for the transmon, similarly to Eq. 8:

$$\hat{\varphi} = (\frac{2E_C}{E_J})^{\frac{1}{4}}(\hat{q}^\dagger + \hat{q}) \tag{16}$$

$$\hat{n} = \frac{i}{2}(\frac{E_J}{2E_C})^{\frac{1}{4}}(\hat{q}^\dagger - \hat{q}) \tag{17}$$

leading to the more familiar form of the transmon Hamiltonian:

$$\hat{H}_{\text{transmon}} = \sqrt{8E_CE_J}\hat{q}^\dagger\hat{q} - \frac{E_C}{12}(\hat{q} + \hat{q}^\dagger)^4 \rightarrow \hbar\omega_q\hat{q}^\dagger\hat{q} - \frac{E_C}{2}\hat{q}^\dagger\hat{q}^\dagger\hat{q}\hat{q} \tag{18}$$

where we define the Josephson plasma frequency $\hbar\omega_p = \sqrt{8E_CE_J}$ and the 'Lamb shift' $E_C$ [25] so the transmon frequency is effectively $\omega_q = \omega_p - E_C$. The self-Kerr term $\frac{E_C}{2}\hat{q}^\dagger\hat{q}^\dagger\hat{q}\hat{q}$ is the anharmonicity of the transmon. For increased photon number $\hat{q}^\dagger\hat{q}$, the frequency of the qubit is further shifted by $-E_C$, removing the degeneracy of the energy levels in Eq. 7. We now have an anharmonic oscillator, allowing us to use this as a two level quantum bit where we generally use the transmon's two lowest quantum number eigen states as $|g\rangle$ and $|e\rangle$ with transition frequency $\omega_{ge}$ that differs from the next transition $\omega_{ef} = \omega_{ge} - \alpha_q$.

With one Josephson junction, the frequency of the transmon is fixed once fabricated. To make a frequency tunable transmon, we replace the single junction with a superconducting loop of two nominally identical junctions in parallel. This creates a DC SQUID (Superconducting Quantum Interference Device) [26], shown in Fig. 7(a). The pair of junctions creates an effective single junction that has a tunable phase $\varphi_{ext}$. This changes the critical current $I_c$ and the eigen spectrum of the qubit, allowing us to shift the entire energy potential well in frequency while maintaining transmon anharmonicities. This is achieved in the laboratory by threading magnetic flux through the loop of Josephson junctions.

The expression for Josephson energy in Eq. 13 is modified slightly to become:

$$E_J(\Phi) = \frac{\Phi_0 I_c}{2\pi}\left|\cos(\frac{2\pi\Phi}{\Phi_0})\right| \tag{19}$$

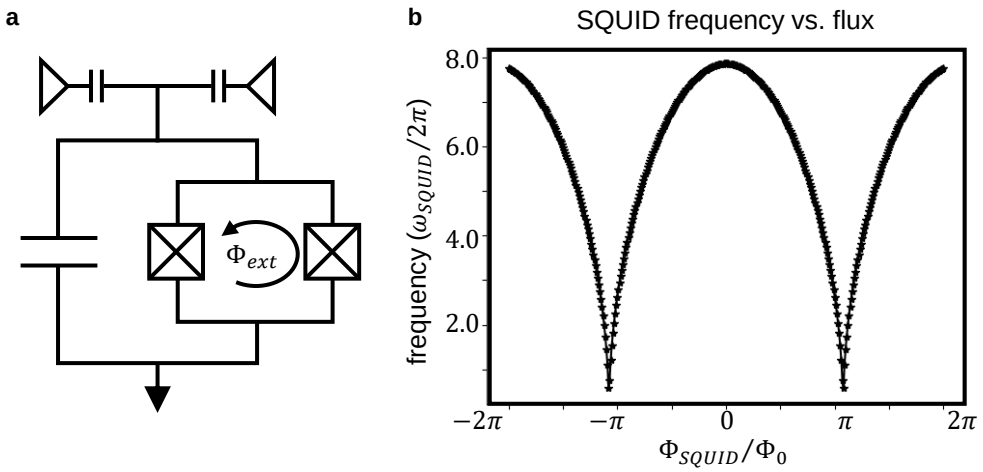


Figure 7: **The DC SQUID** (a) A frequency tunable transmon can be made by putting two identical Josephson junctions in parallel in place of just one. (b) When magnetic flux is threaded through the loop of junctions, the frequency response of the SQUID changes due to changes in the total effective Josephson inductance $L_J(\varphi)$. The frequency of the SQUID follows the form in Eq. 21.

for maximum effective critical current $I_c$ and phase through the Josephson junction loop $\Phi$. This contributes to the SQUID's Josephson inductance as:

$$L_J(\Phi) = \frac{\Phi_0}{2\pi I_c \left|\cos\left(\frac{2\pi\Phi}{\Phi_0}\right)\right|} \tag{20}$$

leading to a frequency dependence of the form:

$$\omega_{SQUID}(\Phi) = \sqrt{\frac{2\pi I_c \left|\cos\left(\frac{2\pi\Phi}{\Phi_0}\right)\right|}{\Phi_0 C}} \tag{21}$$

with capacitance $C$. The frequency vs. flux modulation of the SQUID is shown in Fig. 7(b).

Often our experiments have preferred frequencies and operating points, making it tempting to always use a split junction transmon. There are some issues that can arise. First, it is quite difficult to make Josephson junctions the exact dimensions intended. This is due to

inconsistencies that arise in the fabrication process. If the two junctions are not identical, we replace the single $\cos\hat{\varphi}$ term in Eq. 14 with:

$$\hat{H}_{splitJJ} \propto -E_{J1}\cos\hat{\varphi}_1 - E_{J2}\cos\hat{\varphi}_2 \tag{22}$$

for the Josephson energies of each $E_{J1,2}$ and phase difference across each junction $\hat{\varphi}_{1,2}$. The effective superconducting phase difference and Josephson energy of an asymmetric SQUID introduces interesting effects that will be described later in this chapter, Sec. 2.1.4. For the purpose of making an easily frequency tunable transmon, the scene is a bit more complicated. The biggest issue that arises is the loss of qubit information to magnetic flux noise. This causes a decrease in qubit phase coherence time $T_2$. Fabrication results are often 'close enough' and a DC SQUID transmon is only used for absolute necessity.

### 2.1.3 Coupling Qubits to Cavities

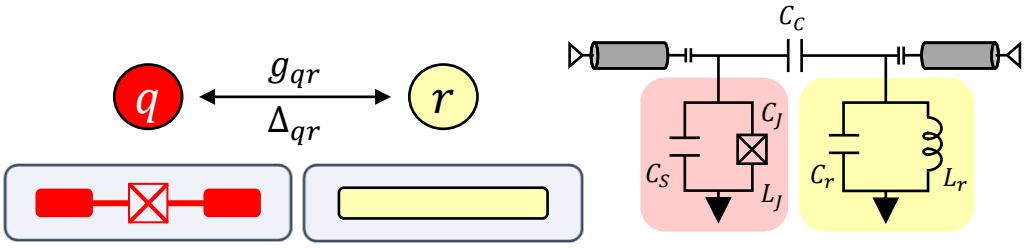


Figure 8: **Coupling qubits and cavities** The generic mode coupling of a qubit and cavity. The modes $q$ and $r$ exchange energy at rate $g_{qr}$ and frequency detuning $\Delta_{qr}$. If $\Delta_{qr} \to 0$, their interaction is governed by a strong coupling Hamiltonian like Eq. 23. If $\Delta_{qr} \gg g_{qr}$, the system is in the dispersive regime with Eq. 26.

In circuit QED, qubits can be strongly coupled to neighboring resonator modes for storage and readout of their state(s), in contrast to cavity QED, where atoms are weakly coupled to their surrounding cavity. Storage and readout are almost mutually exclusive cavity operations. If the lifetime of the cavity mode is longer than the qubit's it is used for storage of qubit

information, often implemented with 3D cavities like in Ref. [27]. However readout needs to occur much faster than qubit decay so these cavities should have short lifetimes [28]. Superconducting quantum circuits provide protection to qubits allowing us to use the cavity's(-ies') light to retain and understand their behavior.

This strong coupling allows us to project qubit information in the cavity's excitations and protect qubits from decoherence. For a qubit mode $q$ and resonant cavity mode $r$, we can write their joint Hamiltonian in the Jaynes-Cummings basis [29] as

$$\frac{H_{JC,qr}}{\hbar} = \omega_r r^\dagger r + \omega_q q^\dagger q - \frac{E_C}{12}(q+q^\dagger)^4 + g_{qr}(q^\dagger r + qr^\dagger + qr + q^\dagger r^\dagger). \tag{23}$$

All hats (ex. $\hat{q}$) indicating operators have been removed for visual decluttering. The first two terms are the cavity and transmon's respective oscillator energies, followed by the transmon's fourth order anharmonic term. In this expression we do not make the simplifying assumption that $(q+q^\dagger)^4 \rightarrow q^\dagger q^\dagger qq$ because, as will be described below, the diagonalization of Eq. 23 will produce self- and cross-Kerr terms involving cavity operators. The final term in Eq. 23 is the direct exchange interaction.

The qubit and cavity exchange excitations at vacuum Rabi coupling rate:

$$g_{qr} = \frac{1}{2}\sqrt{\omega_q \omega_r}\frac{C_C}{\sqrt{(C_r+C_C)(C_S+C_C)}} \tag{24}$$

which features the resonator's capacitance $C_r$, transmon shunt capacitance $C_S$, and coupling between the two $C_C$, depicted in Fig. 8. Terms $\propto qr + q^\dagger r^\dagger$ can be ignored in the rotating wave approximation for coupling much less than either bare mode frequency $g_{qr} \ll \omega_q, \omega_r$. In the rotating frame, we see a rediagonalization of the Hamiltonian that transforms it to the new coupled basis, where under the strong Jaynes-Cummings interaction the excitations of the circuit for operators $\tilde{q}$ and $\tilde{r}$ are now a dressed function of both bare modes.

When the modes' detuning is much greater than their coupling ($\Delta_{qr} = |\tilde{\omega}_q - \tilde{\omega}_r| \gg g_{qr}$), we operate in what is called the 'dispersive regime.' In this limit, the resonator inherits some nonlinearity, like weak self-Kerr terms $\propto \tilde{r}^\dagger \tilde{r}^\dagger \tilde{r}\tilde{r}$ and cross-Kerr terms $\propto \tilde{q}^\dagger \tilde{q} \tilde{r}^\dagger \tilde{r}$. The Hamiltonian takes the form:

$$\frac{H_{\text{dispersive},qr}}{\hbar} = \tilde{\omega}_r \tilde{r}^\dagger \tilde{r} + \tilde{\omega}_q \tilde{q}^\dagger \tilde{q} - \frac{\alpha_q}{2}(\tilde{q}^\dagger \tilde{q}^\dagger \tilde{q}\tilde{q}) - \chi_{qr}(\tilde{q}^\dagger \tilde{q} \tilde{r}^\dagger \tilde{r})) \tag{25}$$

which can be suggestively rearranged as:

$$\frac{H_{\text{dispersive},qr}}{\hbar} = \tilde{\omega}_q \tilde{q}^\dagger \tilde{q} - \frac{\alpha_q}{2}(\tilde{q}^\dagger \tilde{q}^\dagger \tilde{q}\tilde{q}) + (\tilde{\omega}_r - \chi_{qr}\tilde{q}^\dagger \tilde{q})\tilde{r}^\dagger \tilde{r}. \tag{26}$$

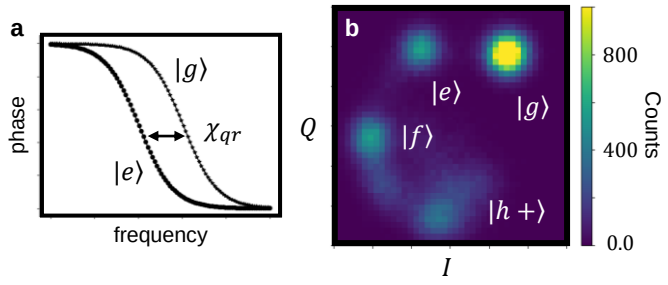


Figure 9: **Dispersive measurement of transmons** In a coupled system like in Fig. 8, when $\Delta_{qr} \gg g_{qr}$, the qubit-cavity interaction term causes a shift in response frequency of the cavity when the qubit is excited. (a) We can infer the state of the qubit indirectly by measuring two distinct cavity states separated by $\chi$. (b) For systems with high readout fidelity, like those backed with parametric amplifiers, we can distinguish multiple states of the transmon by further $\chi$ shifting. In this histogram of cavity measurements, we see distinct blobs for $|g\rangle$, $|e\rangle$, and mostly $|f\rangle$, while those for $|h\rangle$ and beyond are harder to separate due to decreased coupling to higher order modes and decreased qubit lifetimes.

In this form, the effect of such a coupling regime can be seen by photon number counting. If the qubit mode has a photon (meaning the Fock basis eigen value of $N = \tilde{q}^\dagger \tilde{q} \to 1$), the cavity mode will shift down in frequency by $\chi_{qr}$. For typical experiments, this value is only up to a few MHz, sufficient to infer the qubit's state by measuring the cavity. If the cavity responds at $\tilde{\omega}_r$, the qubit is likely in $|g\rangle$, or if it responds at $\tilde{\omega}_r - \chi_{qr}$, it is likely in $|e\rangle$. This is shown visually in Fig. 9. Likewise, if the cavity has $n$ photons, it will shift at $-n\chi_{qr}$ [30]. This quantum non-demolition (QND) measurement allows us to repeatedly measure the qubit without perturbing its state [31]. An excellent work up of the formulas produced in this chapter can be found in Ref. [32].

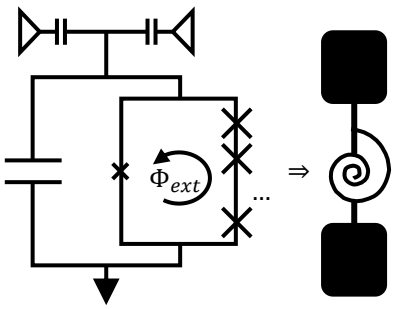


Figure 10: **The SNAIL** The SNAIL [14] joins the family of superconducting quantum creatures with $n > 1$ large junctions in parallel with one smaller at Josephson energy ratio $\alpha_s$. External magnetic flux is threaded through this loop to change the distribution of energy throughout the circuit and its frequency and self-nonlinearity.

### 2.1.4 The SNAIL

Multiple Josephson junctions can be assembled in more complicated geometries to produce circuit elements with different functionalities. One such way is as a SNAIL [14] (a backronym [33]). The SNAIL is realized with $n > 1$ large identical Josephson junctions in parallel with one smaller one, see Fig. 10. In 2- and 3D circuits, the SNAIL takes on the form factor of a dipole with large capacitor pads on either side of the superconducting loop. Magnetic flux $\Phi_{ext}$ is threaded through the loop. Not only does adjusting $\Phi_{ext}$ change the frequency (much like a SQUID), but it also changes the nonlinear coefficients that arise due to this asymmetric junction layout.

The SNAIL potential energy takes the form:

$$U_s(\varphi) = \alpha_s E_J \cos\varphi - nE_J \cos\left(\frac{\varphi_{ext} - \varphi}{n}\right) \tag{27}$$

where the large Josephson junctions each have Josephson energy $E_J$, the smaller has $\alpha_s E_J$ with unit-less ratio $\alpha_s$. The junctions are fabricated such that $E_J \gg E_C$. The reduced superconducting phase parameter $\varphi = \frac{\Phi}{\Phi_0}$ is the phase across the small junction per flux

quantum, while $\varphi_{ext} = \frac{\Phi_{ext}}{\Phi_0}$ is the reduced external flux through the loop. Expanding near a minimum $\varphi_{min}$, we minimize the energy and find expansion coefficients:

$$c_m = \frac{1}{E_J} \frac{d^m U_s}{d\varphi^m}\bigg|_{\varphi=\varphi_{min}} \tag{28}$$

for coefficients of order $m$. Defining $\tilde{\varphi} = \varphi - \varphi_{min}$, we find an effective potential:

$$U_{s,eff}(\tilde{\varphi})/E_J = \frac{c_2}{2!}\tilde{\varphi}^2 + \frac{c_3}{3!}\tilde{\varphi}^3 + \frac{c_4}{4!}\tilde{\varphi}^4 + ... + \frac{c_m}{m!}\tilde{\varphi}^m \tag{29}$$

where all order coefficients are present without loss of generality. We can write the SNAIL's Hamiltonian as $H_s = 4E_C N^2 + U_{s,eff}(\tilde{\varphi})$ and in a similar circuit quantization as taken in Sec. 2.1, we can write the SNAIL Hamiltonian in the raising and lowering operator basis:

$$\frac{H_s}{\hbar} = \omega_s s^\dagger s + \sum_{m=3}^{\infty} g_m (s + s^\dagger)^m \tag{30}$$

with frequency $\omega_s = \frac{1}{\hbar}\sqrt{8c_2 E_J E_C}$ and nonlinear parameters:

$$g_m = \frac{c_m}{\hbar\, m!} E_J (\varphi_{ZPF})^m \tag{31}$$

where the zero-point fluctuation phase can be rewritten as $\varphi_{ZPF} = \sqrt{\frac{\hbar\omega_s}{2c_s E_J}}$. This result highlights how the SNAIL has a native, leading third order nonlinearity and each successively higher order term is decreased due to the $1/m!$ factorial coefficient.

The SNAIL can be tuned to operate at bias conditions where the even order terms $g_{4,6,...}$ go to zero, corresponding to a point where $\Phi_{ext} = \Phi_{ext}^{null}$. This is desirable to mitigate issues of the Kerr and AC Stark effects. These effects can potentially become problematic when we use the SNAIL (or any nonlinear circuit element) as a multi-wave parametric mixer, discussed in greater detail in Sec. 2.2.1.

## 2.2 Parametric Mixing

The Jaynes-Cummings direct exchange Hamiltonian of Eq. 23 requires $\Delta_{ij} \to 0$ for couplings modes $i$ and $j$. Energy is only swapped back and forth between them and the interaction is always on. This is not always desirable, or even feasible, for particular applications in quantum computing. For example, we may want to couple modes that are very far apart in frequency [34], turn the interaction on only when desired [35], or create an interaction like $i^\dagger j^\dagger$ rather than $i^\dagger j$ [36]. This necessitates an alternative coupling scheme like parametric mixing.

Parametric mixing can be realized with linear and nonlinear circuit elements, but this thesis will focus on the use of nonlinear couplers to achieve the desired outcome. In superconducting quantum circuits, this is made possible with Josephson junction elements, especially those like SNAILs and JRMs (Josephson Ring Modulators) which feature both even and odd order nonlinearities, as opposed to purely-even order nonlinear elements like transmons and SQUIDs. I will begin explaining parametric interactions with coupling a SNAIL to a generic mode $a$. In this thesis, $a$ will be a transmon qubit (whose Kerr nonlinearity adds further complication to this procedure), but these parametric couplers can also be coupled to linear modes like cavities. Often the coupler circuit element itself will be one of the modes affected by the mixing process.

Consider a SNAIL mode with generic nonlinearity as in Eq. 30 coupled to harmonic oscillator mode $a$. Their undriven Hamiltonian takes the form:

$$\begin{aligned} \frac{H_0}{\hbar} &= \frac{H_L}{\hbar} + \frac{H_{NL}}{\hbar} \\ &= \omega_s s^\dagger s + \omega_a a^\dagger a + g_{sa}(s^\dagger a + s a^\dagger) + g_{sa}(s^\dagger a^\dagger + s a) + \sum_{m=3}^{\infty} g_m (s + s^\dagger)^m \end{aligned} \tag{32}$$

for a SNAIL mode with all order nonlinearity. The expression for $H_0$ is broken into the linear components $H_L$ (those with two operators) and the nonlinear components $H_{NL}$ (those with more than two operators). This Hamiltonian can be transformed to the proper frame to highlight the desired interactions by first treating the nonlinear components of Eq. 32

as perturbations. Diagonalizing $H_L$ to get $H'_L$, using a standard Bogoliubov transformation detailed in Refs. [37, 32], produces dressed mode frequencies:

$$\tilde{\omega_s} = \frac{1}{2}(\omega_s + \omega_a - \sqrt{\Delta_{sa}^2 + 4g_{sa}^2}) \tag{33}$$

$$\tilde{\omega_a} = \frac{1}{2}(\omega_s + \omega_a + \sqrt{\Delta_{sa}^2 + 4g_{sa}^2}) \tag{34}$$

for mode detuning $\Delta_{sa} = \omega_s - \omega_a$. This transformation also creates new effective raising and lowering operators:

$$\tilde{s} = \cos(\Lambda)s - \sin(\Lambda)a \tag{35}$$

$$\tilde{a} = \cos(\Lambda)a + \sin(\Lambda)s \tag{36}$$

for a displacement choice $\Lambda = \frac{1}{2}\arctan(\frac{2g_{sa}}{\Delta_{sa}})$. The tilde (ex. $\tilde{s}$) will be omitted for simplicity (moving forward all operators and coefficients are transformed to the new diagonal basis). This procedure is standard for any mode coupling (not just nonlinear ones). Circuit QED modes in the laboratory are dressed modes and altered by their couplings to other modes and channels. The nonlinear perturbation term also gets transformed with the same unitary operation to $H'_{NL}$.

We will now focus on the leading third order terms ($m = 3$). A microwave drive on mode $s$ at frequency $\omega_d$ and time dependent strength $\epsilon_d(t)$ has the drive Hamiltonian:

$$\frac{H_{drive}}{\hbar} = (\epsilon_d(t)e^{-i\omega_d t} - \epsilon_d^*(t)e^{i\omega_d t})(s^\dagger - s). \tag{37}$$

We add all three $H'_L + H'_{NL} + H_{drive}$ and apply a displacement transformation to reach an interaction Hamiltonian of the form:

$$\frac{H'_{int}}{\hbar} = \omega_s s^\dagger s + \omega_a a^\dagger a + g_3(s + \frac{g_{sa}}{\Delta_{sa}}a + \eta_d e^{-i\omega_d t} + h.c.)^3 \tag{38}$$

for driving term $\eta_d = \frac{2\omega_d \epsilon_d(t)}{\omega_d^2 - \omega_s^2}$. This derivation is described in greater detail in Ref. [38]. Expanding this leads to all combinations of terms as some combination of three operators in $s^{(\dagger)}$ and $q^{(\dagger)}$. Not all terms will survive the rotating wave approximation and some will be used towards potential parametric interactions.

The rotating wave approximation (RWA) is used to eliminate terms in the expansion of Eq. 38 that do not conserve energy (like terms $\propto ss, a^\dagger a^\dagger$) and those that oscillate at frequencies very fast compared to the pumped system's dynamics. using the rotation operator:

$$R = e^{-iH_L' t} \tag{39}$$

with the linear Hamiltonian $H_L'$ components from Eq. 32. The total Hamiltonian in Eq. 38 is transformed under the operation:

$$H_{RWA}'' = RH_{int}'R^\dagger + i\hbar \dot{R} R^\dagger \tag{40}$$

which eliminates the linear terms (like $\omega_s s^\dagger s$, etc.) and moves the nonlinear components to:

$$\frac{H_{RWA}''}{\hbar} = g_3(se^{-i\omega_s t} + \frac{g_{sa}}{\Delta_{sa}} ae^{-i\omega_a t} + \eta_d e^{-i\omega_d t} + h.c.)^3 \tag{41}$$

where now the choice of $\omega_d$ will lead to term cancellation and highlight the parametrically induced processes.

If $\omega_d = \omega_s + \omega_a$, the terms $(s^\dagger e^{i\omega_s t})(a^\dagger e^{i\omega_a t})(\eta_d e^{-i\omega_d t})$ and $(se^{-i\omega_s t})(ae^{-i\omega_a t})(\eta_d^* e^{i\omega_d t})$ are the only ones with phase cancellation to 0 and that conserve energy, rotating at the appropriate frame frequency. This leads to a Hamiltonian:

$$H_\Sigma = g_{\Sigma_{s,a}}(s^\dagger a^\dagger e^{-i\phi_d t} + sae^{i\phi_d t}) \tag{42}$$

for $\phi_d = \arg(\eta^*)$ pump phase and $g_{\Sigma_{s,a}} = 6g_3 \frac{g}{\Delta_{sa}} |\eta_{d,\Sigma}|$ the effective parametric interaction strength. This Hamiltonian will be called the '$\Sigma$' process, as photons are added in pairs, but is often referred to as a gain or two mode squeezing Hamiltonian.

Likewise if $\omega_d = \omega_s - \omega_a$, the terms $(s^\dagger e^{i\omega_s t})(ae^{-i\omega_a t})(\eta_d e^{-i\omega_d t})$ and $(se^{-i\omega_s t})(a^\dagger e^{i\omega_a t})(\eta_d^* e^{i\omega_d t})$ are the only ones with phase cancellation to 0 and that conserve energy, rotating at the appropriate frame frequency. This leads to a Hamiltonian:

$$H_\delta = g_{\delta_{s,a}}(s^\dagger a e^{-i\phi_d t} + sa^\dagger e^{i\phi_d t}) \tag{43}$$

with $g_{\delta_{s,a}} = 6g_3 \frac{g}{\Delta_{sa}} |\eta_{d,\delta}|$. This Hamiltonian will be called the '$\delta$' process, as photons removed from one mode are exchanged into the other. This is referred to as a conversion or beam splitting Hamiltonian. Equation 43 differs from the always-on interaction of Eq. 23 because this parametric process does not require strong direct coupling and is only turned on when the pump is supplied.

### 2.2.1 Nonlinear and Even-Order Terms

Odd-order, nonlinear parametric driving schemes, like those described in Eqs. 42 and 43, do not have the potential to cause frequency shifting. We will compare third to fourth order nonlinear terms as the canonical example in this section, but the same argument also applies to higher order odd vs. even nonlinearities.

Three wave parametric mixing creates effective two-body interactions under the appropriate driving conditions to satisfy the RWA. Terms that are purely comprised of one mode's operators, like $s^\dagger ss$, do not have the appropriate number of operators to conserve energy. These types of interactions do not remain in the eigen basis. For example, $s^\dagger ss\,|n\rangle = (n-1)\sqrt{n}\,|n-1\rangle$ removes a photon from the system entirely rather than staying in $|n\rangle$. This means we do not need to worry about 'all of one mode' terms in a three-operator interaction. Some three operator terms that mix modes using a number operator, like $s^\dagger sa$ can act for an undriven Hamiltonian at special frequencies. For example, if $2\omega_s = \omega_a$, this will produce some interesting 'crossings.' The mode $a$ will appear to have an avoided level crossing in spectroscopy due to this frequency collision, but mode $s$ will not for low drives because we can only swap pairs of photons. We try to avoid this scenario with carefully mapped frequency choices.

However in four wave mixing, the same is not necessarily true. Consider Eq. 38 if instead of assuming only $m = 3$, we had also included an $m = 4$ SNAIL term:

$$\frac{H_4}{\hbar} = g_4(se^{-i\omega_s t} + \frac{g_{sa}}{\Delta_{sa}}ae^{-i\omega_a t} + \eta_d e^{-i\omega_d t} + h.c.)^4 \tag{44}$$

This leads to combinations of three and four operators when the entire Hamiltonian gets transformed. Unlike in the above argument, terms with four of the same operator could conserve energy. For example $s^\dagger s^\dagger ss\,|n\rangle = (n-1)n\,|n\rangle$ for eigenvalue $n$. This form is seen in the transmon's anharmonicity in Eq. 18. With increased photon number, the mode shifts in frequency by the coupling coefficient. When there are instead terms with a raising and lowering operator for each mode involved, like the term $q^\dagger qr^\dagger r$ in Eq. 25, the frequency of the modes shift due to occupation in the other modes, highlighted by the dispersive shift rearrangement to Eq. 26.

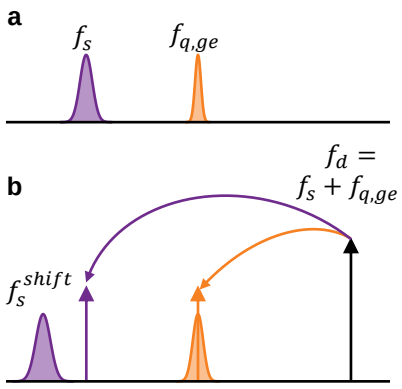


Figure 11: **Frequency shifting** (a) Without any drives on the system, a SNAIL and qubit each have static frequencies and finite mode widths. These are the frequencies used to drive a parametric process like in Eq. 42. (b) The parametric drive at $f_s + f_{q,ge}$ is now detuned from $f_s^{shift}$, which is the new frequency of the SNAIL mode as a function of drive strength. The parametric drive would 'miss' because the photon created by the parametric pump is outside of the bandwidth of the shifted mode.

This issue is summarized as the Kerr effect. Kerr terms are those involving four operators in an interaction that is always on, or rather not involving the driven terms including an exponential driven phase $e^{\pm i\omega_d t}$. Self-Kerr terms are those with four of the same operator type, and cross-Kerr are those that mix the coupled modes' operators. This can cause trouble if frequency shifts are not properly accounted for, meaning the shift causes an unwanted interaction with another process or the frequency of a drive or pump is detuned. Cross-Kerr is useful when properly calibrated and intentional, like in a dispersive qubit readout protocol (Fig. 9). However issues like frequency overlapping can occur, causing spurious interactions or making a parametric drive detuned outside the modes' finite bandwidth (Fig. 11). For these reasons, we try to avoid undriven Kerr terms by biasing our SNAIL to conditions where Eq. 44 $= 0$ (and generally Eq. 31 goes to zero for all even $m$) with adjusting the Josephson energy by externally applied flux $\Phi_{ext}^{null}$ [39].

Kerr terms also refer to those that move when the system is pumped, for example pro-

ducing $f_{shift}$ in Fig. 11. The AC Stark effect causes trouble with strong drives. In terms of Eq. 44 involving the driven operation $\eta_d^{(*)} e^{\mp i\omega_d t}$, there will be those that cancel phase and produce number conserving operations (ex: $\propto |\eta_d|^2 s^\dagger s$). These terms cause frequency shifting with increased photon number and drive strength, as well as cause measurement induced dephasing and artificial mode broadening [40]. In the processes described in Chap. 3, we require increasingly powerful drives to increase the rates of our parametric interactions. Therefore we would prefer to avoid any drive-induced AC Stark shifting because we do not necessarily track these shifts with increased power.

## 2.3 Outlook and Next Steps

In this chapter, I have provided an overview of the building blocks for my PhD research. The cQED platform allows us to configure circuits in countless ways. We can make combinations of qubits, cavities, and parametric couplers to create the interactions needed to engineer just about any Hamiltonian we desire. Superconducting systems built with one or more Josephson junctions have nonlinear responses that allow for the creation of two level systems to be used as qubits and parametrically driven interactions that allow us to dynamically create couplings. We drive and measure these systems with microwave pulses sent in and out from room temperature, which interact with cryogenic, superconducting systems.

While superconducting qubits are an established platform within the burgeoning field of quantum computing, some issues must still be addressed [41]. In the NISQ (Noisy Intermediate Scale Quantum) device era [42], we must improve (a) qubit 'quality', (b) mode connectivity, (c) gate fidelity, and (d) scalability. Qubits lifetimes must be improved to allow for higher computational circuit depth, and their information must be encoded with other qubits to create long-lived logical qubits out of many physical qubits. The gates or operations we perform with these physical and/or logical qubits need to be performed without loss of information to noise, or at least with errors corrected using efficient quantum error correction schemes [43]. Additionally, quantum computers using SC qubits should be able to do all of these tasks, but with more qubits to increase $2^N$ information for $N$ qubits. An

added challenge is the scaling of physical hardware, both to drive/connect/measure circuits but to also protect them from the hot, noisy room temperature world we perform these tasks from.

In this thesis, I will show how I use these circuit elements and engineered Hamiltonians to create two main projects: a fully engineered qubit-bath coupling and a single 'atom' maser. Both experiments benefit greatly from the ability to create microwave-frequency modes that have the desired level of nonlinearity to achieve parametric three-wave mixing to alter the state of my transmon. Additionally, both require external flux to tune my systems to their operation sweet spots. In the first project, whose data is shown in Chap. 4, the SNAIL is biased to a point of high $g_3$ and $g_4 \approx 0$ for driving purely third order Eqs. 42 and 43. In the second, with data in Chap. 5, we tune the bias conditions for two separate circuit modes: first the SNAIL is biased to high $g_3$ and surprisingly sometimes moderate $g_4$, and second a SQUID to force my qubit and cavity on resonance with one another.

## 3.0 Bath Engineering and Single Atom Masing: Theory

### 3.1 Bath Engineering with Parametric Mixing: Theory

Losses in any physical system are inevitable. They are especially deleterious in quantum systems, where any coupling to another observer causes a loss of precious quantum information. Quantum mechanical circuit elements, like qubits, are all coupled to their environment, but cannot go completely unprotected as their wave function would collapse with 100% certainty. The wave function, and thus life cycle, of a qubit is dependent on the properties of its couplings to its environment, and even enhanced by cavity couplings in cQED [44]. We measure this in parameters like $T_1$ for energy decay, $T_{2,\ Ramsey}$ for equatorial dephasing sensitive to low-frequency noise, and $T_{2,\ Echo}$ which measures dephasing by removing frequency-dependent noise [45, 46, 47].

There is much work being done to increase qubit coherence times (Refs. [48, 49, 50, 51, 52] to name a small few) to increase computing performance and our ability to actually do computational tasks with the qubits at hand [53]. Loss mechanisms due to different channels add inversely, rates add linearly:

$$\frac{1}{T_{i,i+1}} = \Gamma_{i,i+1} + \Gamma_{i+1,i} \tag{45}$$

where the mode $q$ has energy decay times between adjacent levels $i$ and $i+1$, visually depicted in Fig. 1. Both the up-going $\Gamma_{i,i+1}$ and down-going $\Gamma_{i+1,i}$ rates in Eq. 45 can be modified to change $T_1$. Quantum fluctuations and finite bath temperatures can cause the qubit to gain energy, without any driving pulse. For a 'cold' system, this rate should be much smaller than the down-going rate (ex: $\Gamma_{eg} \gg \Gamma_{ge}$). Increasing Q-factors, or decreasing these rates like what's shown above, is one such way to increase $T_1$.

However, the presence of this loss need not be fatal. While we cannot necessarily eliminate bath loss, the interaction between a qubit and its bath is a controllable parameter. This thesis focuses on how we use parametric mixing to engineer this loss and increase interaction rates, experimentally setting how the qubit exchanges energy with its finite temperature

bath. The caveat: my work does not improve Q-factors or increase transition times, but rather increases the rate of qubit thermalization to some intended steady state. I decrease the time for transitions and control what state the qubit ends up in. Additionally, I will only discuss energy losses, not phase decoherence.

In cQED specifically, there are many examples of bath engineering experiments, a non-exhaustive list includes Refs. [54, 55, 56, 57, 58, 59, 60, 61]. These works add specific excitations to their systems, alter mode couplings, or create a new basis. The work described below seeks to engineer a bath and make whatever qubit steady state(s) desired, at whatever rate is desired, quasi-independently of natural decay properties.

The project was initiated by a theory paper by Hafezi et al. [1]. A photonic chemical potential can arise in a system where the qubit-bath interactions are controlled with parametric couplings. In this paper, they propose employing a three-wave parametric mixer [36] to modulate couplings between a qubit and a low temperature, low frequency bath. Figure 12 shows a generic mode schematic adapted from the paper. The chemical potential is set by the frequency of the parametric coupler, which determines which parametric process is activated and how it behaves.

The use of three-wave mixing is often preferred over four-wave, see Sec. 2.2.1. Kerr and AC Stark effects cause frequency shifting in modes with fourth order nonlinearity. Even-order mixing schemes are difficult to efficiently pump and manage because modes will shift in frequency with higher mode occupation and under strong drives. For our system, we wish to strongly pump our mixer mode in order to vary the chemical potential $\mu$ in any way we please. The mixer mode is low Q and designed to be cold (having low or nearly-zero photon occupation on average), making $n$ also low. However, Kerr shifting will be non-negligible, making it more difficult to track down a pumping frequency that causes the parametric process we desire and potentially inducing other unwanted cross-interactions.

Third order nonlinearity is much easier to parametrically pump because the parametric coupler is not susceptible to Kerr- or AC Stark shifting. The third order nonlinear Hamiltonian coefficient is also typically larger than the fourth, so we can supply weaker pumps to still see an effect. Josephson junction based parametric converters like the JRM and SNAIL have nonlinearity terms of all orders from third and above. Therefore to avoid self-Kerr

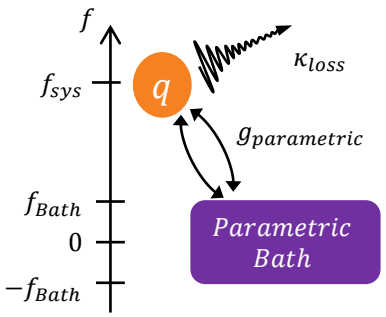


Figure 12: **Bath engineering, adapted from Hafezi et al.** [1] A low frequency, low temperature parametric bath is coupled to the higher frequency system. They exchange information through a parametric coupling, and the system loss is $\kappa_{loss}$. Modulating the parametric coupling $g_{parametric}$ alters how the system interacts with the bath, and thus how it gains and loses information.

terms we operate them at external flux bias conditions where the third order Hamiltonian coefficients are maximized and fourth order minimized [62]. At these biases, fifth and higher odd order nonlinearities will also be present, but much smaller in magnitude.

After my colleagues Xi Cao and Gangqiang Liu's initial work on this project using a low frequency JPC, we decided to pursue this experiment with a SNAIL using three-wave mixing. Details on the SNAIL can be found in Chap. 2.1.4, so an abbreviated explanation will be given in this chapter. A SNAIL that is weakly hybridized with a transmon will produce Hamiltonian terms that look like:

$$H_{sq} \propto (s + \frac{g_{sq}}{\Delta_{sq}} q + h.c.)^3. \tag{46}$$

All hats on operators have been removed for neatness. We want to utilize terms that feature one $s$ operator and one $q$ to conserve energy. The SNAIL mode will be pumped, and its dynamic operator $s$ and $q$ are what we are ultimately seeking to modify. With the addition of a drive and displacement operation, this Hamiltonian is transformed to:

$$H^d_{sq} \propto g_3(se^{-i\omega_s t} + \frac{g_{sq}}{\Delta_{sq}} qe^{-i\omega_q t} + \eta_d e^{-i\omega_d t} + h.c.)^3. \tag{47}$$

Expanding this, only the terms that are energy conserving and pumped at the correct frequency will be activated under the rotating wave approximation. When $s$ on the SNAIL mode is pumped at $f_d = f_s + f_q$, we see an effective gain Hamiltonian meaning that one photon each is added to the SNAIL and qubit modes. When instead $s$ is pumped at $f_d = f_s - f_q$, we get a conversion process where energy from the qubit mode is exchanged with the SNAIL. Another important feature of note is that multiple parametric pumps may be applied simultaneously [62]. Each process that is driven is activated and ultimately the final state of the system will be affected by the combination of all pumps. In our experiment, we will measure this as the competition of rates $\Gamma_\uparrow$ vs. $\Gamma_\downarrow$ modulated by $g_{\text{gain, total}}$ vs. $g_{\text{conversion, total}}$.

With these concepts in mind, we can start to put the pieces together to build a fully configurable transmon bath. We can realize such a system with a transmon coupled to a low Q-factor SNAIL. I will use the pump operation on the SNAIL to make the qubit state what I want, and the dynamic $s$ operator to control the rate at which the qubit reaches that state.

### 3.1.1 Transmon Heating

I find it easiest to visualize the SNAIL-qubit coupling with a ladder diagram to understand the effect of drives and engineered dissipations, see Fig. 13. Let us first examine the system using the gain operation. We assume the joint ground state, although I will do nothing to necessarily force it there. Pumping on $s$ at $f_d = f_s + f_{q,ge}$ drives the gain-type Hamiltonian in a process we call '$\Sigma$' (for the addition of qubit photons):

$$H_\Sigma = g_{\Sigma_{s,ge}}(s^\dagger q^\dagger e^{-i\phi_d t} + sqe^{i\phi_d t}). \tag{48}$$

This moves the joint $|s, q\rangle$ state from $|0, g\rangle$ to $|1, e\rangle$, the first ladder rung above the ground state where a photon each occupies the SNAIL and qubit. The parametric process is driven at coupling rate $g_{\Sigma_{s,ge}} \propto g_3 \frac{g_{sq}}{\Delta_{sq}} \epsilon_d$ for room temperature driving strength $\epsilon_d$.

From $|1, e\rangle$, the SNAIL decays at rate $\kappa_s$ leading to $|0, e\rangle$. The leading loss $\kappa_s$ is designed to be the fastest process in the entire experiment. This ensures the qubit 'sees' a cold SNAIL bath (Fig. 14) and that the entire process repeats. In turn, this makes a population inverted qubit that sits in $|e\rangle$. This is completely unlike a qubit driven by a $\pi$-pulse (Fig. 32(a)),

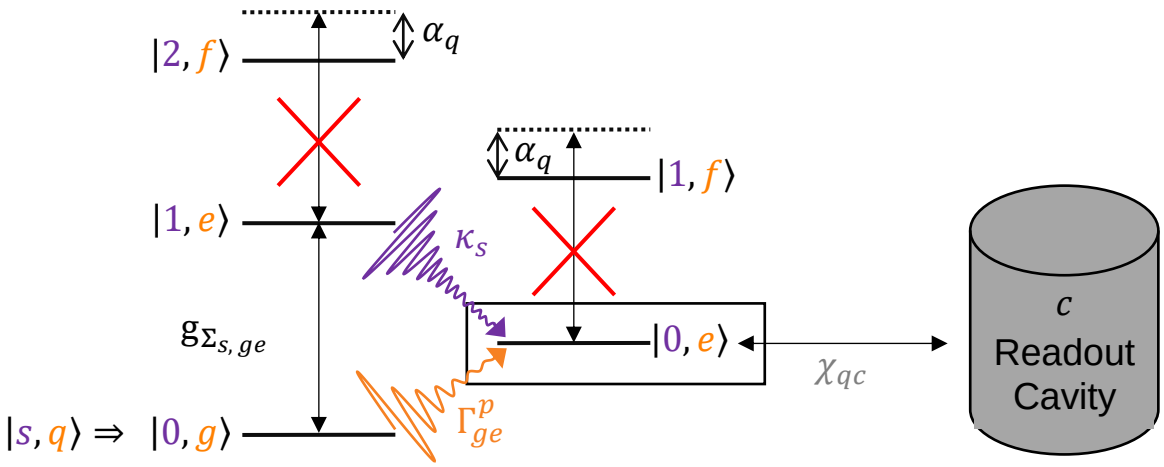


Figure 13: **Transmon heating ladder diagram** A step-wise visual depiction of the energy gains and losses in our experiment. The parametric pump $\Sigma_{s,ge}$ is modulated at $g_{\Sigma_{s,ge}}$, exciting $s$ and $q$. The fastest rate $\kappa_s$ causes fast decay to $|0, e\rangle$, the target state for this experiment. The qubit is effectively brought to the excited state at $\Gamma_{ge}^{p}$. Transmon anharmonicity prevents higher order qubit transitions as they are selectively detuned from the parametric gain process.

which is the standard way to excite a qubit! Single, typically Gaussian, $\pi$ pulses bring the qubit from one Bloch sphere pole to another, so from $|i\rangle$ to $|i+1\rangle$, and $|i+1\rangle$ to $|i\rangle$. The pulse applied here, however, is a finite width flat-top that should only excite from $|i\rangle$ to $|i+1\rangle$. Finally, the qubit is dispersively coupled to a cavity $c$ mode so its state is inferred through a shift in cavity response.

Crucially, the transmon is anharmonic. This prevents drives between intended adjacent qubit levels from also inducing other qubit excitations. Under the $\Sigma_{s,ge}$ drive, the pump $f_d = f_s + f_{q,ge}$ is only tuned for the $|g\rangle \rightarrow |e\rangle$ transition, and is detuned by $\alpha_q$ from the $|e\rangle \rightarrow |f\rangle$ transition and so on, depicted with red X's in Fig. 13. This, along with the SNAIL's engineered short lifetime, mean that energy in the system remains in the lowest manifold of states, and not coupled to or lost in decay channels we are not seeking.

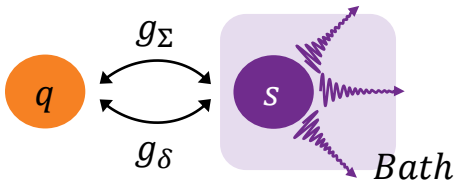


Figure 14: **Transmon bath energy exchange** The system-bath coupling is slightly modified in our experiment compared to Figs. 1 and 12. The qubit $q$ is coupled to the SNAIL $s$, which exchanges energy with its bath. Therefore the qubit-bath interaction is controlled by the qubit-SNAIL interaction, which we parametrically pump at rates $g_\Sigma$ and $g_\delta$. This experimental knob means we can set the qubit's effective mode temperature and chemical potential.

The generic parametric heating process $\Sigma_{s,\,i,\,i+1}$ occurs at an effective rate $\Gamma^p_{i,\,i+1}$. This rate goes quadratically with pump strength, inverse to SNAIL decay rate $\kappa_s$ because $\kappa_s \gg g_\Sigma$ [63]:

$$\Gamma^p_{i,i+1} = \frac{4g^2_{\Sigma_{s,i,i+1}}}{\kappa_s}. \tag{49}$$

In this process, $g_\Sigma$ is the 'regeneration' rate, or the rate at which photons are added back into the system. This is controlled by changing how strong and at what frequency we parametrically pump at, and the strength of hybridization between the SNAIL and qubit. In designing the system in simulation, we can vary the direct dipole-dipole coupling to change $g_{sq}$. Once fabricated and cooled down, however, we lose that degree of freedom. We can change where we bias the SNAIL in frequency and nonlinearity, to change $g_3$ and potentially introduce higher $g_4$, and tune the parametric driving frequency and strength.

### 3.1.2 Transmon Cooling

The opposite parametric process that can be driven is photon swapping or mode conversion. In a process we call $\delta$, the qubit can be brought to the ground state faster than it

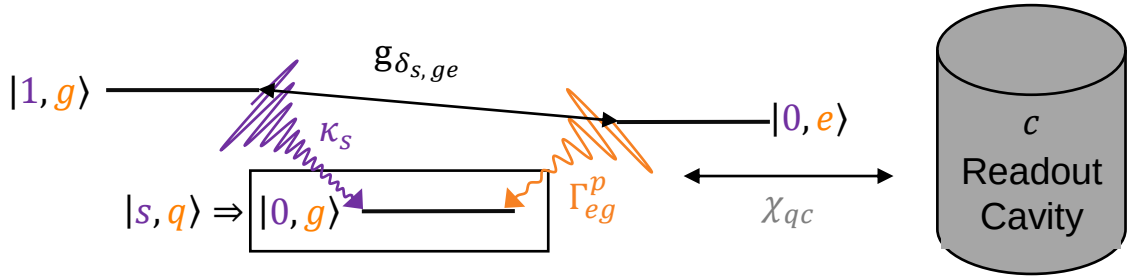


Figure 15: **Transmon cooling ladder diagram** A step-wise visual depiction of the energy gains and losses in our experiment. The qubit is prepared in $|e\rangle$ and the parametric pump $\delta_{s,ge}$ is modulated at $g_{\delta_{s,ge}}$, exchanging the excitation from the qubit to the SNAIL. $\kappa_s$ causes fast decay to $|0,g\rangle$, the target state for this experiment. The qubit is effectively brought to the ground state at $\Gamma^p_{eg}$.

would if simply left to energy decay. This is useful in a scenario where the qubit population needs to be reset, and different than a typical $T_1$ decay because the rate of $\Gamma^p_{eg}$ will be experimentally controlled, rather than allowed to naturally interact with an untouched bath. So in cases where the down-going rate needs increasing, we must increase the coupling to the qubit's dissipative bath to carry that energy away (Fig. 14). The SNAIL works for just that purpose.

Shown in Fig. 15, this time starting with the transmon with some excited, finite temperature population we pump $s$ at $f_d = f_s - f_{q,ge}$ and induce the photon exchange Hamiltonian that causes the photon in $q$ to exchange with $s$:

$$H_\delta = g_{\delta_{s,ge}}(s^\dagger q e^{-i\phi_d t} + s q^\dagger e^{i\phi_d t}) \tag{50}$$

The SNAIL then quickly decays at $\kappa_s$ to carry the energy away from the joint SNAIL-qubit system. Similarly to $\Sigma$, the $\delta$ drive is controlled by the frequency and strength of the parametric pump $g_{\delta_{s,ge}}$. To pull the qubit from $|e\rangle \rightarrow |g\rangle$, we pump at $f_d = f_s - f_{q,ge}$ to bring the qubit to $|g\rangle$ at rate $\Gamma^p_{eg}$. This rate follows the same form as Eq. 49 with instead $g_{\delta_{s,\ i,\ i+1}}$.

Note that this process is different than other reset protocols because it does not require an extra resonator [64], multiple state-conditional pulses [65], or very specific parametric pump frequencies [66]. The SNAIL mode is broad and reconfigurable in situ with external flux biasing and parametric drives, and therefore accepts any pump frequency supplied.

### 3.1.3 Full Parametric Control and the Chemical Potential

Both $\Sigma$ and $\delta$ described above are completely general and can be tuned for any qubit transition between adjacent levels. The first cycle of the 'parametric ratchet' goes as [prepare qubit, apply pump, SNAIL decays, qubit in target state], and each subsequent cycle as [qubit decay out of target state, apply pump, SNAIL decays, qubit in target state, repeat as needed]. Every repetition is heralded by a SNAIL photon, which is emitted at a frequency within the broad band of the mode. With these single parametric pumps, we gain control over a single decay process. For example if $\Sigma_{s,ge}$ is applied, we only control the rate $\Gamma^p_{ge}$, while the other rates (like $\Gamma_{eg},\ \Gamma_{ef},\ \Gamma_{fe}$ etc.) are not directly in our control.

In order to control multiple rates and the steady state solution we must apply multiple parametric pumps. If we, the experimentalist, can set the rates of transmon thermalization, ad hoc, then we can alter the bath dynamics. A general system Hamiltonian takes the form:

$$H^p_{\text{total}} = \sum_i g_{\Sigma_{s,i,i+1}}(s^\dagger \left|i+1\right\rangle \left\langle i\right| + s \left|i\right\rangle \left\langle i+1\right|) + \sum_i g_{\delta_{s,i,i+1}}(s^\dagger \left|i\right\rangle \left\langle i+1\right| + s \left|i+1\right\rangle \left\langle i\right|). \tag{51}$$

Written in this suggestive form, the utility of such a coupling scheme becomes apparent. Any two adjacent levels of the transmon, $i$ and $i+1$ can be parametrically coupled by driving its respective process, $\Sigma_{s,i,i+1}$ or $\delta_{s,i,i+1}$, and any combination of those parametric processes may be simultaneously driven. Each parametric process is activated independent of any others, but the effective total rates for each transition (like $\Gamma^p_{ge},\ \Gamma^p_{eg}$ etc.) are affected by any imparted drives, so different drives may be individually tuned to produce the desired total transition rates and steady state populations.

In the case of occupying up to a certain level, we can think of this as realizing a chemical potential for photons. In thermodynamics, the chemical potential $\mu$ is an additional term

to the mode energy that signals the addition or removal of particle number. In an electron system, energy is filled up to the Fermi level set by $\mu$ [67]. This model works well for finite-number particles. But photons are not that easy! In Planck's work on blackbody radiation [68], there is not a $\mu$-type term because photons are absorbed and emitted by the walls of their container. We cannot count unique photons in a box. Other works outside of superconducting qubits [69, 70, 71] have realized a chemical potential for photons with electrons and holes in semiconductor junctions and optical cavities that form Bose-Einstein condensates. In our experiment with superconducting quantum elements, however, we take advantage of the $\Sigma$ and $\delta$ processes demonstrated to selectively occupy qubit states, seen in Fig. 16.

### 3.1.4 Chemical Potential Theory

We will now take a short aside to study the Lindbladian Master Equation formalism for understanding a photonic chemical potential. This work is adapted from our paper Ref. [72] and the following analytical derivations spearheaded by my colleague Xi Cao.

We simplify the qubit and SNAIL both as two level systems. For the transmon this is not too far of a stretch given its anharmonicity, and for the SNAIL it holds because it thermalizes much faster than the parametric processes ($\kappa_s \gg g_\Sigma,\ g_\delta$), keeping the mode cold. The Hamiltonian features both $\Sigma$ and $\delta$ parametric processes described, driven at $\omega_\Sigma = \omega_s + \omega_q$ and $\omega_\delta = \omega_s - \omega_q$. In the rotating frame it is approximated as:

$$H^R_{sq}/\hbar = g_\Sigma \sigma_s^+ \sigma_q^+ + g_\delta \sigma_s^+ \sigma_q^- + \text{h.c.} \tag{52}$$

The dynamics of the master equation are illustrated by the Lindbladian:

$$\dot{\rho} = \frac{1}{i\hbar}[H^R_{sq}, \rho] + \kappa_s D(\sigma_s^-)\rho + \kappa_q D(\sigma_q^-)\rho \tag{53}$$

where dissipator $D(a)\rho = a\rho a^\dagger - \frac{1}{2}\{a^\dagger a, \rho\}$, and $\kappa_i$ is the decay rate of the $i^{\text{th}}$ channel. We model only SNAIL decay because $\kappa_s \gg \kappa_q$, leading us to write:

$$\begin{aligned}\dot{\rho} =& \frac{1}{i\hbar}[H^R_{sq}, \rho] + \frac{\kappa_s}{2}(\bar{N}(\omega_s)+1)(2\sigma^-\rho\sigma^+ - \rho\sigma^+\sigma^- + \sigma^+\sigma^-\rho) \\ &+ \frac{\kappa_s}{2}\bar{N}(\omega_s)(2\sigma^+\rho\sigma^- - \rho\sigma^-\sigma^+ + \sigma^-\sigma^+\rho).\end{aligned} \tag{54}$$

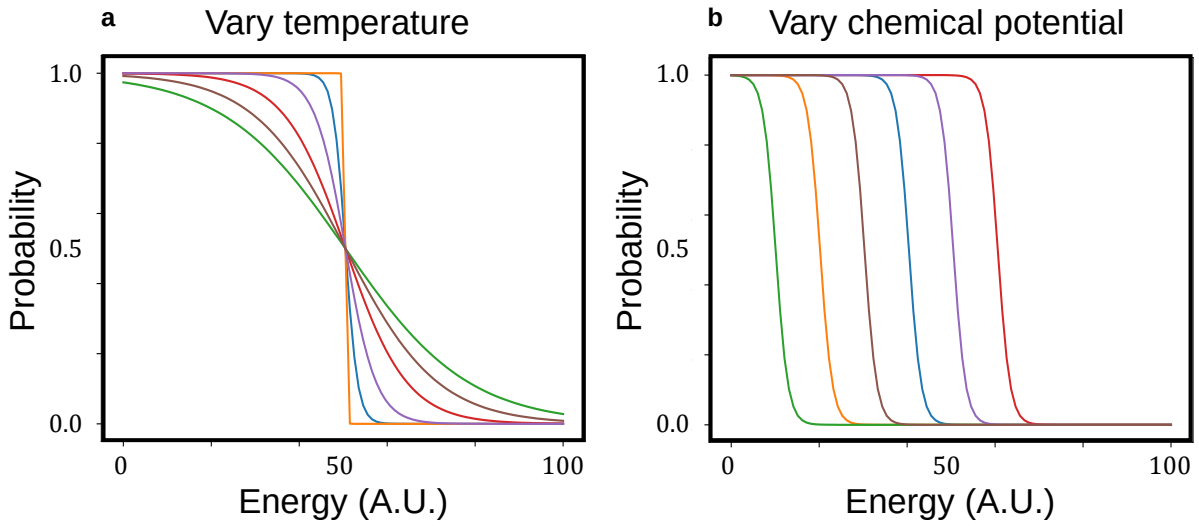


Figure 16: **Fermi energy with varying $T$ and $\mu$** The equation $P(E) = 1/e^{(E-\mu)/k_BT} + 1$ describes the population per energy state for particles following Fermi-Dirac statistics. This expression features the chemical potential $\mu$ which determines the energy up until which will be occupied by particles. The probability per energy unit is plotted. (a) When the temperature $T$ is varied, the sharpness of occupation is changed. The nearly-step function curve occurs for small temperatures, while the large sweeping curve is for large temperatures. (b) Instead if the temperature is constant and $\mu$ varied, the highest energy of occupation shifts. For increased $\mu$, the energy increases. Our experiment seeks to modify both variables. We wish to change the states that get photon occupation ($\mu$) and how occupied each state is ($T$).

For $\bar{N}(\omega_s) = 1/(e^{\hbar\omega_s/kT_{\text{Bath}}} - 1)$, the average photon number for the thermal state at temperature $T_{\text{Bath}}$. In this model, only the SNAIL is coupled to the bath. To solve the master equation, break $\dot{\rho}$ into each matrix element and find the equilibrium solutions to each mode by tracing out the other mode with $\rho^s = \text{Tr}_q(\rho)$, leading to a simplified density matrix for the SNAIL mode:

$$\rho^s = \begin{pmatrix} \frac{1+\bar{N}(\omega_s)}{1+2\bar{N}(\omega_s)} & 0 \\ 0 & \frac{\bar{N}(\omega_s)}{1+2\bar{N}(\omega_s)} \end{pmatrix}. \tag{55}$$

The SNAIL is in a thermal state at the bath's temperature provided:

$$\frac{g_\delta^2 g_\Sigma^2}{(g_\delta^2 + g_\Sigma^2)\kappa_s^2} \ll 1, \tag{56}$$

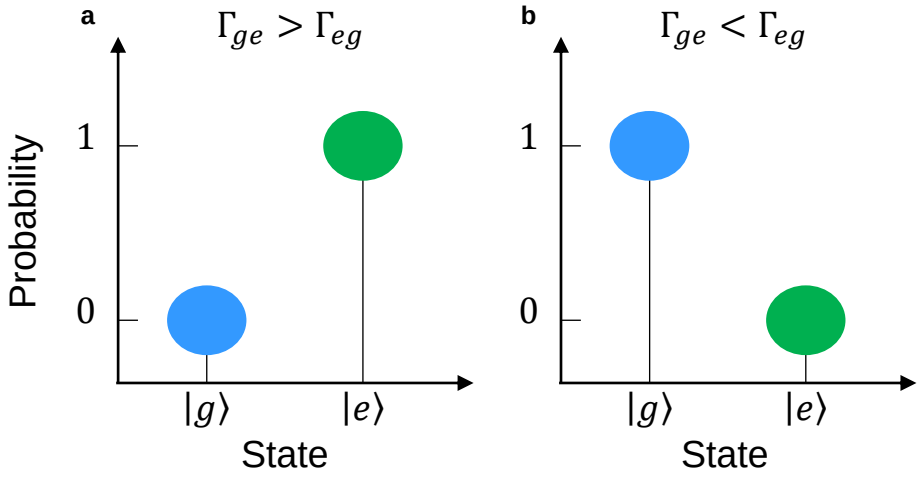


Figure 17: **Transmon heating and cooling rate representation** This cartoon model shows the effects of rate engineering on qubit populations. (a) When the rate from $|g\rangle$ to $|e\rangle$, $\Gamma_{ge}$ exceeds that from $|e\rangle$ to $|g\rangle$, $\Gamma_{eg}$, we see a steady state population inverted qubit that is much more likely to be in the excited than ground states. (b) The opposite case, where $\Gamma_{ge}$ is now less than $\Gamma_{eg}$, and the qubit is more likely to be in the ground state.

The only bath this qubit is coupled to is that of the SNAIL. We similarly trace out the SNAIL mode: $\rho^q = \mathrm{Tr}_s(\rho)$. For qubit heating only, when $g_\delta = 0$:

$$\rho^q = \begin{pmatrix} \frac{\bar{N}(\omega_s)}{1+2\bar{N}(\omega_s)} & 0 \\ 0 & \frac{1+\bar{N}(\omega_s)}{1+2\bar{N}(\omega_s)} \end{pmatrix}, \tag{57}$$

we see a population inverted qubit, visually shown by Fig. 17(a). Likewise for qubit cooling only, when $g_\Sigma = 0$:

$$\rho^q = \begin{pmatrix} \frac{1+\bar{N}(\omega_s)}{1+2\bar{N}(\omega_s)} & 0 \\ 0 & \frac{\bar{N}(\omega_s)}{1+2\bar{N}(\omega_s)} \end{pmatrix}. \tag{58}$$

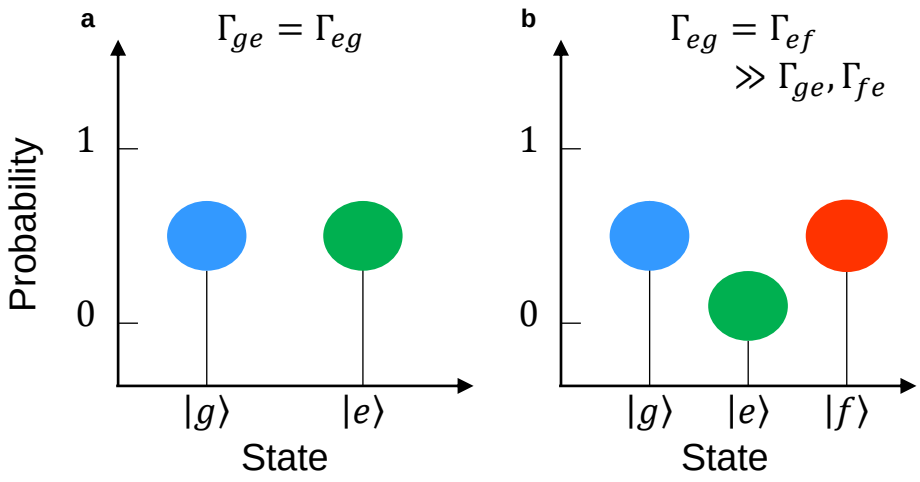


Figure 18: **Simultaneous transmon heating and cooling** With multiple parametric processes activated, we can selectively tune qubit thermalization rates and steady state population probabilities. (a) Controlling between $|g\rangle$ and $|e\rangle$. An example of one configuration possible with tuning two parametric drives: balancing $\Gamma_{ge}$ and $\Gamma_{eg}$ to create a qubit equally in $|g\rangle$ as in $|e\rangle$. (b) Still with two parametric drives, we can balance $\Gamma_{eg}$ and $\Gamma_{ef}$ to create a qubit equally in $|g\rangle$ as in $|f\rangle$. This is outside the chemical potential model described in Sec. 3.1.4.

Here we see the qubit thermalize to the same state as the SNAIL, Eq. 55, seen in Fig. 17(b). This is different than simply adjusting the environment temperature because the qubit's state depends on the parametrically controlled SNAIL statistics $\bar{N}(\omega_s)$.

Turning on both parametric interactions ($g_\Sigma,\ g_\delta \neq 0$), we achieve our desired scenario of obtaining a chemical potential term assuming Eq. 56, depicted in Fig. 18(a). The populations for $|g\rangle = P_g$ and $|e\rangle = P_e$ are found as:

$$P_g = \frac{1}{1 + e^{-\beta(\hbar\omega_s - \mu)}} \tag{59}$$

$$P_e = \frac{e^{-\beta(\hbar\omega_s - \mu)}}{1 + e^{-\beta(\hbar\omega_s - \mu)}}, \tag{60}$$

where

$$\mu = \frac{1}{\beta} \ln\left( \frac{g_\Sigma^2 e^{\beta\hbar\omega_s} + g_\delta^2}{g_\Sigma^2 e^{-\beta\hbar\omega_s} + g_\delta^2} \right). \tag{61}$$

This is our expression for the chemical potential! Note how the qubit's population in $|g\rangle$ and $|e\rangle$ are modulated with $\mu$, which is directly changed with parametric rates $g_\Sigma$ AND $g_\delta$. The grand canonical density matrix can be found with Eqs. 59 and 60:

$$\rho^q(\infty) = Z(\beta,\mu)^{-1} e^{-\beta(\frac{\omega_s}{2}\sigma_q^z - \frac{\mu}{2}\sigma_q^z)} \tag{62}$$

with $Z(\beta,\mu) = \mathrm{Tr}[e^{-\beta(\frac{\omega_s}{2}\sigma_q^z - \frac{\mu}{2}\sigma_q^z)}]$, and $\mu$ given in Eq. 61. The chemical potential and equilibrium state of the qubit is tuned by the ratio of $g_\Sigma$ vs. $g_\delta$.

### 3.1.5 Bath Engineering Population and Rate Calculations

The above prescription shows the steady state solutions for SNAIL-qubit coupling. Next we will examine the dynamics of the system. A semi-classical phenomenological model will be used. The rate for changing from $|g\rangle \to |e\rangle = \Gamma_{ge}$, $|e\rangle \to |g\rangle = \Gamma_{eg}$. This means we may write the probability time dependencies as:

$$\dot{P}_g = -\Gamma_{ge} P_g + \Gamma_{eg} P_e \tag{63}$$

with the condition the probabilities sum to 1: $P_g + P_e = 1$. This can be solved as:

$$P_g = c_0 e^{-(\Gamma_{ge}+\Gamma_{eg})t} + \frac{\Gamma_{eg}}{\Gamma_{ge}+\Gamma_{eg}} \tag{64}$$

with initial condition $c_0$. Transmon heating and cooling will follow this exponential model. The physical temperature should be low enough to allow the dynamics of the driven system to dominate over natural heating.

As will be shown later in Chap. 4, when the transmon has a non-trivial $|f\rangle$ population, we must use a semi-classical model that involves the qubit's third energy level:

$$\dot{P}_g = -\Gamma_{ge} P_g + \Gamma_{eg} P_e \tag{65}$$

$$\dot{P}_e = \Gamma_{ge} P_g - (\Gamma_{ef} + \Gamma_{eg}) P_e + \Gamma_{fe} P_f \tag{66}$$

with $P_g + P_e + P_f = 1$.

### 3.1.6 Bath Engineering Theory: Conclusions and Outlook

The temperature and chemical potential (in the traditional, thermodynamical sense) means that states up to some energy will be occupied (Fig. 16(a)) and nothing above (Fig. 16(b)), so it sets the level of maximum state occupation allowed. The above equations in Secs. 3.1.4 and 3.1.5 allow us to analytically express the populations of our qubit if we know how energy is moving amongst the qubit states. Therefore if we can drive any parametric process, we can make arbitrary combinations of transmon states if the separation between states in phase space is sufficiently large and can tune parametric drives within a window of uncertainty around that qubit transition frequency. However, we do not need to stick within this traditional $\mu$ model, with one such example shown in Fig. 18(b). We will later show in Chap. 4 that we can fill the qubit in an uneven split of occupations, and even show how we can skip occupying levels with occupation on either side.

I have shown above theoretically how any combination of transmon states can be generated in situ at chosen rates. The bath is fully controlled because the gain and loss of energy to/from the bath is experimentally tuned. We determine how the transmon dissipates energy to its environmental bath by tuning how the parametric coupler transfers energy throughout the circuit.

## 3.2 Single-Atom Masing: Theory

The bath engineering experiment of Sec. 3.1 taught us valuable lessons in controlling the rate and steady state of qubit transitions under parametric driving and engineered loss. I now will employ these ideas in building a single-atom maser. The transmon qubit is, after all, an artificial atom and the beauty of cQED is that we can rearrange and configure circuits in countless ways, making for a flexible platform to build a cryogenic light source.

### 3.2.1 What is a Maser?

In the beginning of the 20$^{th}$ century, physicists began to try explaining peculiar observed phenomena that did not match any physical models. These included blackbody radiation [68], the photoelectric effect [73], and the Bohr model of atoms [74]. Einstein's thoughts on discrete quanta of energy led to the idea of a photon [75], as well as the different types of excitations and emissions of photons from atoms. This includes spontaneous emission if the energy is emitted without being probed and stimulated emission if a specific frequency photon probe causes the atoms to release a photon themselves. This can be cascaded if the atoms are continually hit with the correct energy light, causing the emission process to continually repeat. In this case, there is strong coherence amongst the homogeneous population of photons emitted by the same source/atoms.

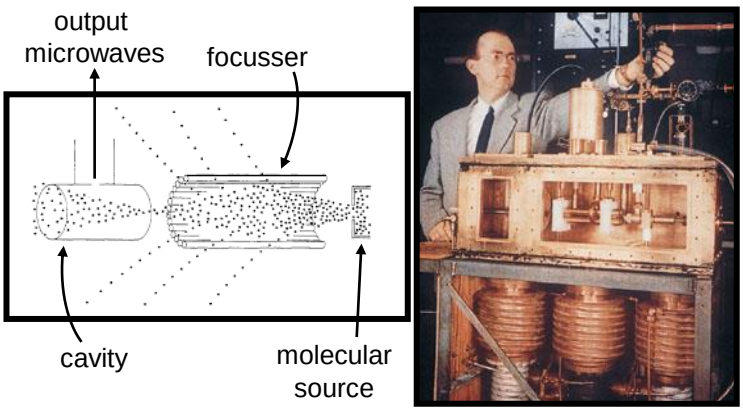


Figure 19: **The ammonia maser** The first demonstration of a maser in the laboratory was by Charles Townes et. al, earning him a joint Nobel Prize in 1964. The molecular source emits molecules into the focusser, where excited molecules enter the cavity and those in the ground state diffuse out. The masing threshold is met when a sufficient number of excited molecules enter the cavity to excite its electromagnetic modes. The diagram is adapted from Townes' Nobel lecture, 1964. On the right, Townes stands with his maser prototype.

The maser was demonstrated in 1954 with ammonia molecules as a coherent source of

electromagnetic radiation in the RF range by Schawlow and Townes [76], see Fig. 19. The maser (Microwave Amplification by Stimulated Emission of Radiation), and its successor the laser (Light —) are made of (generally very many) atoms that have a population of emitted photons that are amplified and emitted into an enclosing cavity. Typically, the atoms are excited by a resonant drive and emit photons. Those photons bounce off the mirrored walls of the cavity, and scatters with the source. This causes the atoms to emit more photons. Now those photons can scatter with the atoms and cause the emission of even more photons. This process repeats and light is collected out of a small opening in the cavity. The light is very coherent because it all was emitted by the same source. This is stimulated emission.

The atoms or masing medium needs to be excited for the process to occur. There is a threshold which must be overcome: masing occurs when the masing medium is in its lowest energy level where stimulated emission dominates over spontaneous emission. This means that the pumped processes are stronger and/or faster than the unpumped ones. Generally, a maser needs [77]:

1. A collection (usually a large number, but can be just one) of atoms, often elements or molecules that have fixed transition energies/frequencies.
2. A high Q-factor cavity to store light, often made of mirrors like a Fabry-Perot cavity [78]. The cavity has radiative loss.
3. Linear couplings between the atoms and cavity, and cavity and output.
4. The atoms are pumped in a $\lambda$-structure, where the excitation is driven from $|0\rangle \leftrightarrow |2\rangle$, and spontaneously decays from $|2\rangle \rightarrow |1\rangle$, where then the $|1\rangle \rightarrow |0\rangle$ light is collected by the cavity.
5. Stimulated emission: the atoms are excited and emit photons. Those photon interacts with other atoms which causes the emission of more photons. This cycle cascades as more photons resonantly interact with the masing medium.
6. The output light is both amplified and narrowed compared to the bare cavity power output $P_c$ and linewidth $\Gamma_c$.

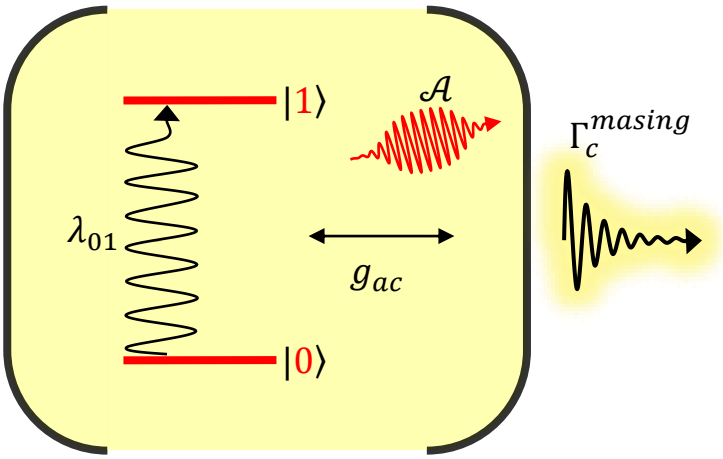


Figure 20: **A single-, two-level atom maser** A toy model for a maser fed by a single atom with only two levels. The atom is incoherently pumped from $|0\rangle$ to $|1\rangle$ at pumping rate $\lambda_{01}$ and couples to the cavity at rate $g_{ac}$. The atom emits light with linear gain coefficient $\mathcal{A}$, and the cavity emits light at $\Gamma_c^{masing}$. Masing is achieved when $\mathcal{A} \geq \Gamma_c$, which is when the atom's emission exceeds the cavity's loss.

### 3.2.2 Master Equation Theory for Single Atom Masing

We can derive maser dynamics using the master equation. The following section is adapted from Chenxu Liu's thesis [79] and Scully and Zubiary's Quantum Optics [77], who provide a thorough work up of laser physics. The simplified version written here is to motivate the problem for experimentally building a micromaser using Josephson junctions.

For simplicity, we will assume our single atom only makes transitions between $|0\rangle$ and $|1\rangle$, not in a $\lambda$-level structure. This will not have an effect on the final answer. We begin with an atom pumped from $|0\rangle \rightarrow |1\rangle$ at incoherent rate $\lambda_{01}$, starting at time $t_0$. The atom couples to the cavity at rate $g_{ac}$ and the cavity decays or loses photons at rate $\Gamma_c$. The cavity has finite coherence because it is made of partially transmitting mirrors that have a non-zero overlap wave function with the outside world.

The atom-cavity coupling Hamiltonian is a simple Jaynes-Cummings model:

$$H_{ac} = g_{ac}(\sigma_a^+ c + \sigma_a^- c^\dagger) \tag{67}$$

where $\sigma_a^\pm$ are the atom's operators and $c^{(\dagger)}$ the cavity's. The equations of motion are described by the master equation for cavity field density operator $\rho$. Assume for simplicity that the atom's degrees of freedom have been traced out, and we are only looking for the cavity field's interactions with the mean atom state:

$$\dot{\rho} = \frac{1}{i\hbar}[H_{ac}, \rho] + \lambda_{01}\mathcal{D}[\sigma_a^+]\rho + \Gamma_c\mathcal{D}[c]\rho. \tag{68}$$

If the cavity decay rate is small compared to the atom-cavity coupling ($\Gamma_c \ll g_{ac}$), then we may adiabatically eliminate neighboring transitions and let $\dot{\rho} = 0$. For cavity occupation transitions between photon number $n$ and $n'$ we may write:

$$\begin{aligned}\dot{\rho}_{n,n'} = &\frac{\mathcal{N'}_{n,n'}\mathcal{A}}{1+\mathcal{N}_{n,n'}\mathcal{B}/\mathcal{A}}\rho_{n,n'} + \frac{\sqrt{nn'}\mathcal{A}}{1+\mathcal{N}_{n-1,n'-1}\mathcal{B}/\mathcal{A}}\rho_{n-1,n'-1} \\ &+\frac{\Gamma_c}{2}(n+n')\rho_{n,n'} + \Gamma_c\sqrt{(n+1)(n'+1)}\rho_{n+1,n'+1}\end{aligned} \tag{69}$$

for linear cavity gain coefficient $\mathcal{A} = \frac{4g_{ac}^2}{\lambda_{01}}$, self-saturation coefficient $\mathcal{B} = \frac{32g_{ac}^4}{\lambda_{01}^3}$, and numerical factors $\mathcal{N}_{n,n'} = \frac{1}{2}(n+n'+2) + \frac{(n-n')^2\mathcal{B}}{16\mathcal{A}}$ and $\mathcal{N'}_{n,n'} = \frac{1}{2}(n+n'+2) + \frac{(n-n')^2\mathcal{B}}{8\mathcal{A}}$. We can think of $\mathcal{A}$ as the density of photons propagating from the atom and $\mathcal{B}$ the point when the atom is saturated due to its bath coupling.

References [79] and [77] go into greater detail, and some of the conclusions drawn are as follows. First, the model assumes no loss of laser levels. Second, there is no pump to re-populate the atom. More complicated models treat this qubit re-population pump as a process where the atom is prepared and injected into the interacting cavity. Atom loss is viewed as the process in which atoms leave the cavity after having interacted with it for some time. This is referred to as a micromaser and is closest to what our system will behave like in the laboratory with photon excitations and emissions.

In the Fock basis, matrix diagonals are not mixed. This means the diagonals (when $n = n'$) give the photon distribution of the laser field. The off diagonals ($|n - n'| = 1$) yield the laser linewidth. In the detailed balance limit, what is lost must be re-pumped back in.

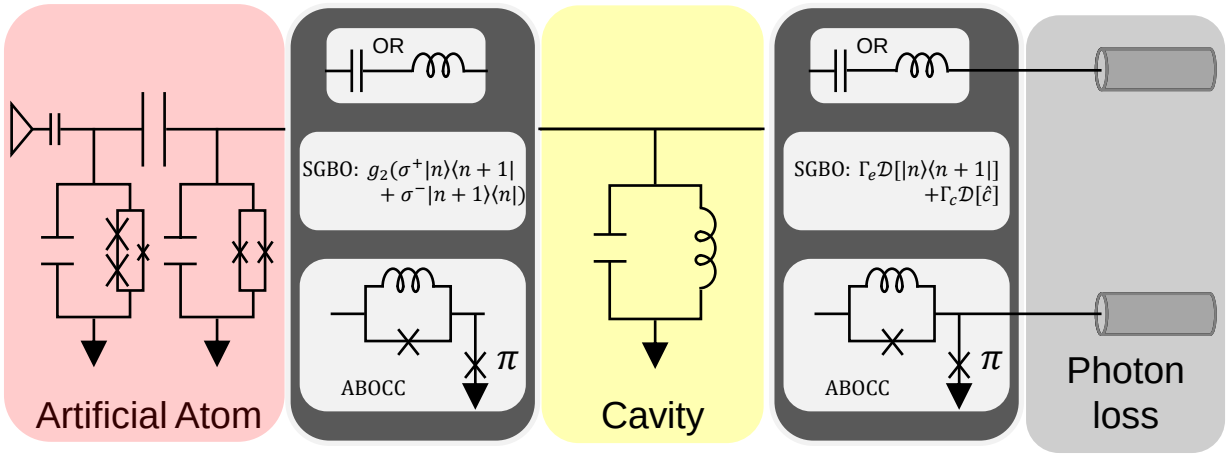


Figure 21: **A theoretical maser circuit diagram adapted from Chenxu Liu et al. [2]** The circuit that inspired this experimental project. The (artificial) atom is made of a transmon qubit coupled to a three-wave mixer. The cavity is an LC oscillator. The coupling between the atom and cavity is modelled in three ways: (top) conventional linear capacitive or inductive couplings, (middle) purely theoretical Susskind-Glogower operators [80], or (bottom) Approximately Bare Operator Coupling Circuits. For masers with either conventional loss or ABOCCs, the output is coupled through a transmission line.

For the diagonal elements and letting $P_n = \rho_{n,n}$, we find the recurrence relation between the number of photons in the cavity:

$$P_n = \prod_{n'=1}^{n} \frac{\mathcal{A}/\Gamma_c}{1 + n'\mathcal{B}/\mathcal{A}} P_0 \tag{70}$$

for all $P_n$ summing to 1. For a linearly coupled Josephson junction based maser, as proposed in Ref. [2], this two-level atom model works well. This is fine for changing the nonlinear ABOCCs (coupler choice on the bottom row of Fig. 21) to more standard linear capacitive couplings (coupler choice on the top row of Fig. 21). We find the linewidth:

$$\Gamma_c^{masing} \sim \frac{\mathcal{A} + \Gamma_c}{8\langle n \rangle} \tag{71}$$

which shows that the phase noise comes from both the gain $\mathcal{A}$ and loss $\Gamma_c$ processes. To meet or exceed the masing threshold, we require $\mathcal{A} \geq \Gamma_c$, leading us to what is referred to as the Schawlow-Townes limit on laser linewidth [81]:

$$\Gamma_c^{masing}(\text{STL}) = \frac{\Gamma_c}{4\langle n \rangle}. \tag{72}$$

This arises from having standard linear couplings between the atom and cavity, and cavity and output channel. With uncertainty in phase noise, and thus photon number, comes a limit on how well we can define the output of the maser. The second half of my PhD has focused on creating such a coherent light source at cryogenic temperatures using superconducting circuit elements.

### 3.2.3 Building a Micromaser in cQED

There have been many papers on building masers out of Josephson junction based circuits. Reference [82] built a single-atom laser using a charge qubit. Reference [83] built a laser using the ac Josephson effect to great success. In their experiment, they have an 'enhancement of emission' where the atom reabsorbs and emits more photons. Additionally, they successfully injection lock their laser to get low linewidths (as opposed to the free running laser I will demonstrate). Reference [84] finds a detailed theory model to explain the ac laser. Additional papers on building a maser/laser with Josephson junctions can be found in Refs. [85, 86, 87], and a nice theory explanation of how to surpass the Standard Quantum Limit in Ref. [80].

The maser is not yet a completely solved problem, though. As shown in Eq. 72, the linewidth of a maser determines its monochromaticity and is limited by quantum mechanics. The standard quantum limit or Schawlow-Townes limit on laser linewidth is due to fluctuations in phase in the cavity and lasing medium or atom states. Noise is what ruins maser linewidth- the only way to move past this limit is to remove sources of noise.

In recent proposals, Refs. [88, 2], the noise can be removed from the system with the addition of nonlinear couplers. Instead of linear couplings between elements, the couplings are nonlinear and thus can sort of mitigate the noise, see Fig. 21. Reference [88] uses one

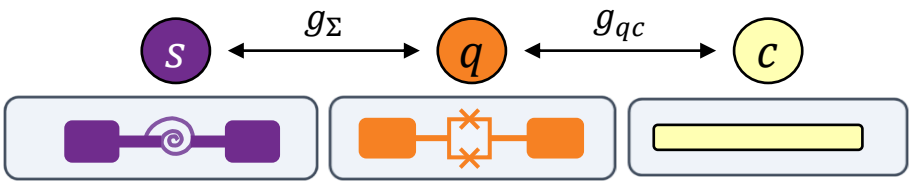


Figure 22: **Maser mode couplings** Our circuit interpretation of the conventional maser in Fig. 21. The single artificial atom transmon $q$ mode is coupled to both a SNAIL $s$ and cavity $c$. The SNAIL serves as the source of population inversion in the qubit through parametric heating and its dissipative bath. The qubit directly exchanges energy with the cavity $c$.

coupler to achieve a $\frac{1}{\langle n \rangle}$ decrease, and Ref. [2] uses two to get $\frac{1}{\langle n \rangle^2}$ reduction. This is done by controlling fluctuations in the atom and/or cavity state to a point where the matrix elements that connect adjacent excitations are independent of photon number, achieved by tuning the mode impedance with the nonlinear couplers. The photon number can grow without adding more uncertainty.

We have great flexibility in cQED, see Chap. 2, to configure the mode structure needed to perform a particular task or bring a desired Hamiltonian to life. We can realize a maser Hamiltonian in our laboratory using superconducting quantum circuit elements and parametric mixing, with or without the introduction of nonlinear couplers.

#### 3.2.3.1 Linear Single-Atom Masing Process

In the following section, I will describe how I will build a maser using the standard elements of cQED with linear inter-elemental couplings. While the long-term goal in Ref. [2] to surpass the Schawlow-Townes limit requires nonlinear couplings (realized in ABOCCs-Approximately Bare Operator Coupling Circuits: made of RF SQUIDS and $\pi$ junctions), we must first build a 'conventional' maser with linear couplings. This proved to be quite the challenge and showed off some interesting physics which highlights the properties of the SNAIL and transmons.

Starting with Fig. 22, we explain each circuit element's purpose in building a maser. First is the LC oscillator cavity, $c$. This cavity is linearly coupled to the other circuit elements via capacitive, dipole-dipole couplings. Inductive coupling is also linear and would have been an equally viable choice. The cavity is high-Q because it needs to build in photon occupation with the masing process, and will be fed these photons by the atom. The cavity's frequency response is given by $\omega_c = \sqrt{\frac{1}{LC}}$. The inductance $L$ and capacitance $C$ are effectively re-normalized due to the cavity coupling to other circuit elements. The cavity's decay rate $\Gamma_c$, when it is NOT masing, is caused by total losses in the system, again dependent on the coupling between modes and the outside world.

Our atom $q$ is artificial, the transmon qubit. It is coupled to a SNAIL mode $s$ that acts as a parametric mixing element. The qubit mode is also a re-normalized mode due to strong coupling to the SNAIL and lesser so by weak coupling to the cavity. In order to exchange energy with the cavity, we place them on resonance, $f_q = f_c$. This is an always-on interaction. The qubit is subjected to its interacting bath, namely the SNAIL's engineered loss. This process of controlling the qubit's bath coupling calls on the exact methods described in the previous bath engineering project of Sec. 3.1. The following ladder diagram in Fig. 23 and Tab. 1 processes are listed step-wise, but the entire process is happening continuously and without any pause between each individual step. All kets are $|s, q, c\rangle$.

Masing occurs when the light emitted by the cavity is both narrowed and brightened, all while not being directly driven. The transmon must be continually populated in order to keep feeding the cavity. This rate of cavity feeding from the transmon, $g_{qc}$, should be faster than the light decaying out of the cavity $\Gamma_c$. Because our atom is a qubit, it should only be able to support a single excitation photon ($|e\rangle$). When the transmon exchanges energy with the cavity, that energy must be replenished. This means the qubit must be population inverted, re-populated at a rate faster than it depletes. This means $\Gamma^p_{ge}$ must be greater than $g_{qc}$.

Chapter 2 details cQED formalism and parametric mixing. Our maser experiment utilizes the SNAIL as a three-wave parametric mixer which yields an effective two-body interaction with weak hybridization and room temperature drives. Its coupling Hamiltonian with the

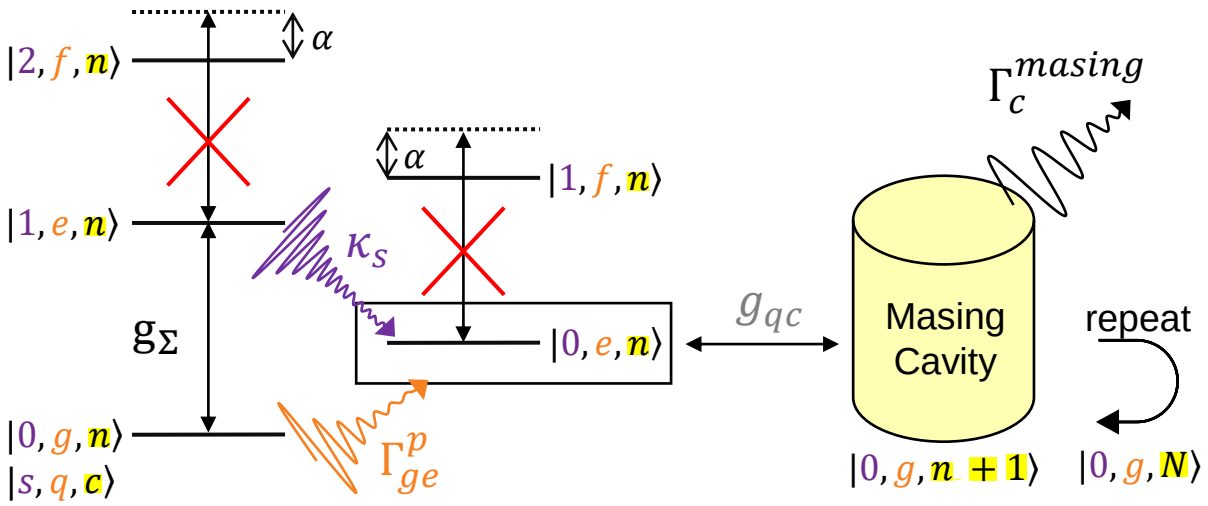


Figure 23: **Masing ladder diagram** A step-wise visual depiction of our masing process. The parametric pump $\Sigma$ is modulated at $g_\Sigma$, exciting $s$ and $q$. The fastest rate $\kappa_s$ causes fast decay to $|0, e, n\rangle$, the target state for this experiment. Transmon anharmonicity prevents higher order qubit transitions as they are selectively detuned from the parametric gain process. The qubit is effectively brought to the excited state at $\Gamma_{ge}^{p}$. This excited photon in the qubit is exchanged with the cavity, increasing its population. This process repeats bringing the cavity population to $|N\rangle$. Light is emitted by the cavity at rate $\Gamma_c^{masing}$.

qubit follows the form:

$$H_{sq} = g_\Sigma(s^\dagger q^\dagger e^{-i\phi_d} + sqe^{i\phi_d}) \tag{73}$$

for parametric pumping rate $g_\Sigma = 6g_3(\frac{g_{sq}}{\Delta_{sq}})|\eta_{d,\Sigma}|$ actuated by the drive $\eta_{d,\Sigma} = \frac{2\omega_d\epsilon_d(t)}{\omega_d^2-\omega_s^2}$ for variable drive strength $\epsilon_d(t)$. For cryogenic experiments, this is a function of the voltage driven from room temperature with microwave controls. The parametric up, or inversion, rate of the qubit is also controlled in situ by the SNAIL-qubit hybridization $\frac{g_{sq}}{\Delta_{sq}}$ and any detunings in pump frequency.

On average, the qubit needs to be population inverted. On top of the drive applied to the SNAIL, there must also be a loss of SNAIL energy in order to keep the parametric process

Table 1: **Step-wise masing with parametric process and engineered loss**

| **Initial state** | **Process** | **Target state** | **Rate** |
|---|---|---|---|
| $\|0, g, n\rangle$ | $\Sigma_{s,ge}$ | $\|1, e, n\rangle$ | $g_{\Sigma_{s,ge}}$ |
| $\|1, e, n\rangle$ | SNAIL loss | $\|0, e, n\rangle$ | $\kappa_s$ |
| $\|0, e, n\rangle$ | qubit-cavity exchange | $\|0, g, n+1\rangle$ | $g_{qc}$ |
| $\|0, g, n+1\rangle$ | Repeat above | $\|0, g, N\rangle$ | $\Gamma^p_{ge} + g_{qc}$ |

going forward within the two-level qubit manifold. The SNAIL loss must be engineered such that $\kappa_s$ is the highest rate of any process- the SNAIL loses its photon and decays to its ground state at rate $\kappa_s$, so that the SNAIL can again be pumped to regenerate the qubit photon, see Fig. 24. I want to emphasize this point: bath engineering is achieved with both parametric drives AND control of losses in our system. To engineer this bath, we must maintain the following rate structure:

$$\kappa_s \gg \Gamma^p_{ge} > g_{qc} \gg \Gamma_c \tag{74}$$

The qubit and cavity should be on resonance, where $\Delta_{qc} = 0$. However, this does not need to necessarily be the case. For small qubit-cavity detunings, the effective coupling rate may be decreased, meaning that the rest of the rate hierarchy in Eq. 74 can be shifted along with it. If $g_{qc,\text{effective}} = \frac{g_{qc}}{\Delta_{qc}}$ is decreased, then $\Gamma^p_{ge}$ and $\kappa_s$ may also be decreased, or rather those processes pertaining to the qubit's re-population have an even greater efficacy compared to the atom-cavity coupling process.

Overall the Hamiltonian of our system takes the form:

$$H_{\text{masing, total}} = g_\Sigma(s^\dagger q^\dagger e^{-i\phi_d} + sqe^{i\phi_d}) + g_{qc}(q^\dagger c + qc^\dagger) - \frac{\alpha_q}{2} q^\dagger q^\dagger qq \tag{75}$$

including the parametric three-wave mixing term at pumped rate $g_\Sigma$, qubit-cavity direct exchange at $g_{qc}$, and qubit anharmonicity $\alpha_q$.

The cavity's light is collected through its transmission line in reflection, which is capactively coupled to the cavity output. In our microwave cryogenic setup, this is through

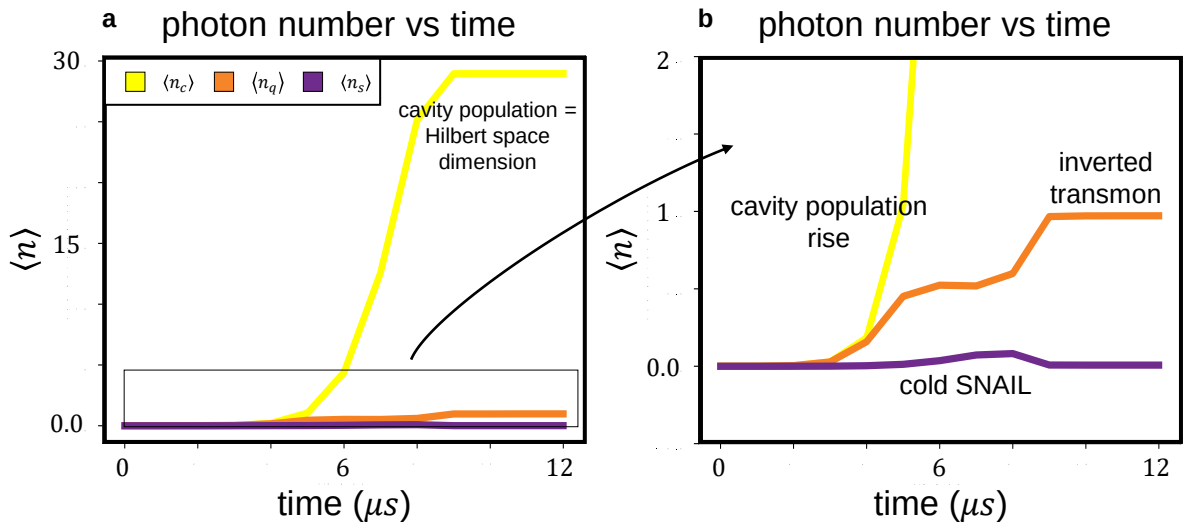


Figure 24: **Photon number simulation** QuTiP simulation for a two-level qubit, two-level Kerr-free SNAIL, and cavity. The steady state solutions for each mode are calculated using the master equation solver in QuTiP. Due to the parametric pump at $f_d = f_s + f_q$, the qubit is population inverted ($\langle n_q \rangle = 1$), the SNAIL is cold ($\langle n_s \rangle = 0$) due to fast decay ($\kappa_s$), and the cavity population grows ($\langle n_c \rangle \to 30$). It is cut off at 30 because that is the limit placed on the simulation matrix size. This simulation shows that a Hamiltonian of the form Eq. 75 achieves our desired masing process.

coaxial lines up to room temperature. The light emitted by the cavity should only be due to the masing process- not light due to any other (in)direct excitation to the cavity mode. This should be narrower than the 'bare' cavity mode, like how the cavity responds when directly weakly probed, and only due to the sustained exchange of photons into the cavity by our population inverted artificial atom transmon.

The process of building light in the cavity is not stimulated emission- we only coherently swap energy into the cavity on resonance. This is due to strong hybridization. The excitation of the atom does not cascade more excitations to keep the process building. The atom should only be able to tolerate a single photon, and it is the parametric pump that keeps populating it, not the other photons in the system that hit it and cause more excitations.

## 4.0 Bath Engineering with Parametric Mixing: Experiment

The data presented in this chapter is adapted and expanded from our preprint [72], and some figures are reproduced in this thesis. The goal of this experiment was to 'program' a superconducting qubit's equilibrium population via parametrically controlling its thermalization rates. This would allow us to change how the qubit shares information with its bath and what thermal population it settles to in the steady state, in contrast to only using the qubit's undriven rates and steady state based on its 'natural' environment and couplings. To perform this task with a superconducting transmon qubit, we have formulated a simple set of controls which in turn place a modest set of requirements on the experimental apparatus which are not too dissimilar from other experiments performed in our laboratory and throughout the community. Namely, we need a three-wave, very low-Q parametric coupler that we can drive and characterize, and a standard transmon dispersively coupled to a readout cavity and the parametric coupler.

### 4.1 Bath Engineering Simulations

Microwave simulations for this experiment were performed with Ansys HFSS, modelled in Fig. 25. As described in Sec. 3.1, this experiment called for maintaining the hierarchy of rates $\kappa_s \gg \Gamma^p_{i,i\pm1}$ and avoidance of frequency collisions. The initial goal, simulated, and measured numerical values of relevant circuit parameters are listed in Table 2.

In this table, there are some discrepancies between simulated and measured values that must be addressed. First, $\kappa_s$ was measured to be less than half of the simulated value. This can be due to imperfect chip placement or trimmed pin length. If the chip is slightly misaligned in its holder, it does not sit in the position in the copper tube that it was designed for, and this can lead to a great difference in mode coupling to its external drive/readout pin. Regardless, this measured value of $\kappa_s$ worked well for our application.

Next, the qubit was initially given a $T_1 = \infty$, or rather it was not assigned a decay. For

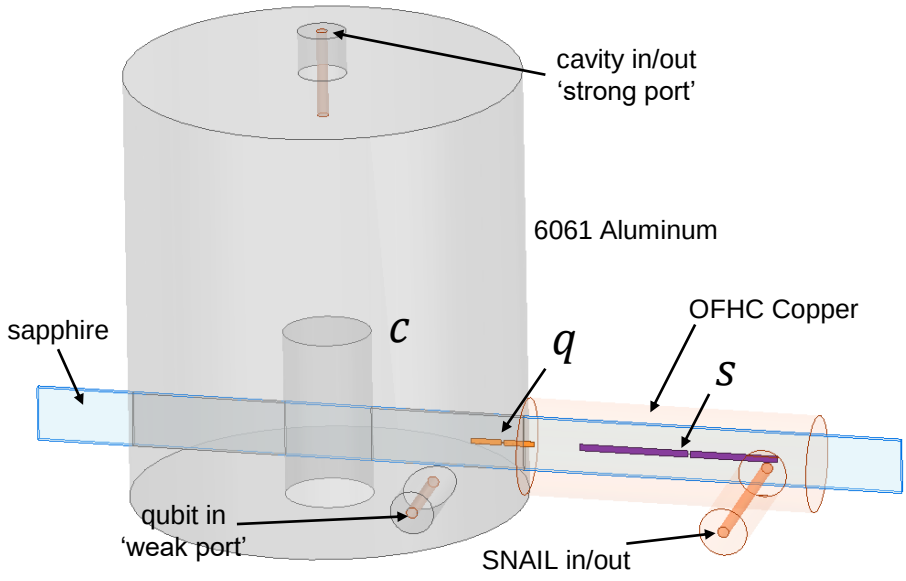


Figure 25: **Microwave simulation design** The experiment as designed in Ansys HFSS. The cavity mode is largely set by the central post. The copper tube adjoining the aluminum cavity holds the SNAIL and part of the qubit. Simulations show that this does not cause degradation of qubit Q-factor.

numerical simulations like in QuTiP, we often do not assign qubits any decay operator to simplify the problem. This is, unfortunately, never the reality but serves its purpose for early simulations. Next, we did not explicitly measure the SNAIL's nonlinearity or qubit-cavity cross-Kerr $\chi_{qc}$, but did perform a 'Duffing sweep' to qualitatively find the correct bias current to operate at. Lastly, this sample was initially designed for the high-Q masing project, so $\kappa_c$ values differ from initial planning to cold samples.

The SNAIL needs to be lossy to drive the ratcheting process, so it quickly decays to continually bring the qubit to its desired state. This engineered loss is the product of a fairly low internal Q-factor ($Q_{int,\ HFSS} \approx 20$ x $10^3$), but dominated by a low external Q-factor ($Q_{ext,\ HFSS} = 214$). The SNAIL's coupling pin, labelled 'SNAIL in/out' in Fig. 25, used for both drive and readout is strongly coupled to the SNAIL mode by extending far into the copper tube, which leads to this high loss rate.

Table 2: **Goal, simulated, and measured values for bath engineered qubits** The target values were determined by our intended Hamiltonian design and QuTiP evaluations of Hamiltonian dynamics. The simulated values were found either directly in HFSS using Eigenmode and Driven Modal solvers, or HFSS data was exported and calculated with the Black-Box Quantization method [89]. Measured values are typical across multiple measurements.

| **Parameter** | **Target value** | **Simulated value** | **Measured value** |
|---|---|---|---|
| $f_s$(operating) | 8.0 GHz | 8.0137 GHz | 8.01 GHz |
| $f_q$ | 4.5 GHz | 4.822 GHz | 4.520 GHz |
| $f_c$ | 7.0 GHz | 7.001 GHz | 6.966 GHz |
| $\frac{\kappa_s}{2\pi}$(operating) | 30 MHz | 37.796 MHz | 12.981 GHz |
| $T_{1,q}$ | $\infty$ | 8.065 s | 15.452 $\mu$s |
| $\frac{\kappa_c}{2\pi}$ | 1.0 MHz | 0.19 MHz | 0.761 MHz |
| $\frac{g_3}{2\pi}$(operating) | $-20$ MHz | $-12.8$ MHz | – |
| $\frac{g_4}{2\pi}$(operating) | 0.0 | 0.0 | $\approx 0$ |
| $\frac{\alpha_q}{2\pi}$ | $-180$ MHz | $-179.98$ MHz | $-197.39$ MHz |
| $\frac{\chi_{qc}}{2\pi}$ | $-1.0$ MHz | $-0.517$ MHz | – |

Additionally, the SNAIL is designed to have a Josephson inductive energy ratio of $\alpha_s = 0.25$ between the single, small Josephson junction and each of the three large junctions on the opposite arm. Note $\alpha_s$ is a dimensionless ratio of inductive energy, not to be confused with $\alpha_q$ the transmon's self-Kerr in units of angular frequency. The small junction was designed to have a critical current of 0.2866 $\mu$A.

The qubit lifetime was calculated in HFSS by assuming the qubit was made of 'Perfect Conductor' and finding the ideal weakly-coupled pin length near the qubit mode. At the time of this project's simulation and initial data-taking phase (mid 2019 to early 2020), assumed best lifetimes were achieved by having a dedicated weak qubit pin and strong cavity pin at the top of the coaxial cavity in the place where the cavity fields are exponentially damped.

In my simulations, I decreased the length of the qubit's pin ('qubit in/weak port' Fig. 25) to increase the mode's Q-factor. However, since this project, there has been much research on the lifetime of qubits in the presence of other modes. In the Hatlab this work has been carried out by my colleague Param Patel, who has shown that the placement of the cavity port is also very important. This idea, which we call WISPE (Waves in Space Purcell Effect) is described in greater detail in Ref. [52].

This sample was initially intended to be a maser (more details in Chap. 5), and so the cavity was supposed to be very high-Q in order to hold onto its photons. However, it became apparent that this sample, and generally the idea of parametrically driving a qubit/controlling its population with a third-order SNAIL, was exactly what we needed to build a fully controlled bath for a qubit. The cavity was initially designed to have a $Q_{ext,\ HFSS} > 1$ x $10^7$, but was easily decreased to 36 x $10^3$ in simulation by simply making the cavity's pin longer, thus increasing the coupling to the post cavity's lowest frequency mode. Photos of the machined device are seen in Fig. 26.

Increasing pin length was not difficult to implement in the lab, despite the metal housing having already been machined. At the time, all coupling pins were made by removing the outer metal jacket and dielectric of a coaxial copper cable, leaving only the center copper pin. This method affords great flexibility in pin length because it can be trimmed to the desired length. Also because the cavity mode was a coaxial, 3D cavity, the frequency and linewidth can be measured at room temperature with a constant (room temperature $\leftrightarrow$ cryogenic temperature) conversion factor! This made trimming the cavity pin to the desired length an easy snip. However, the downside of using trimmed copper cable is that the pin is very flexible and often skews from perfectly-straight. This adds uncertainty in pin-mode coupling because the simulation was made with a straight pin and even small bends in the pin can greatly change the impedance of the mode. Despite our best efforts, there can be even greater issues under cryogenic conditions. Due to thermal contraction, the pin may flex or bend away from the room temperature conditions we had set making results difficult to reproduce. See Fig. 55(a) for a standard RF pin used in this experiment.

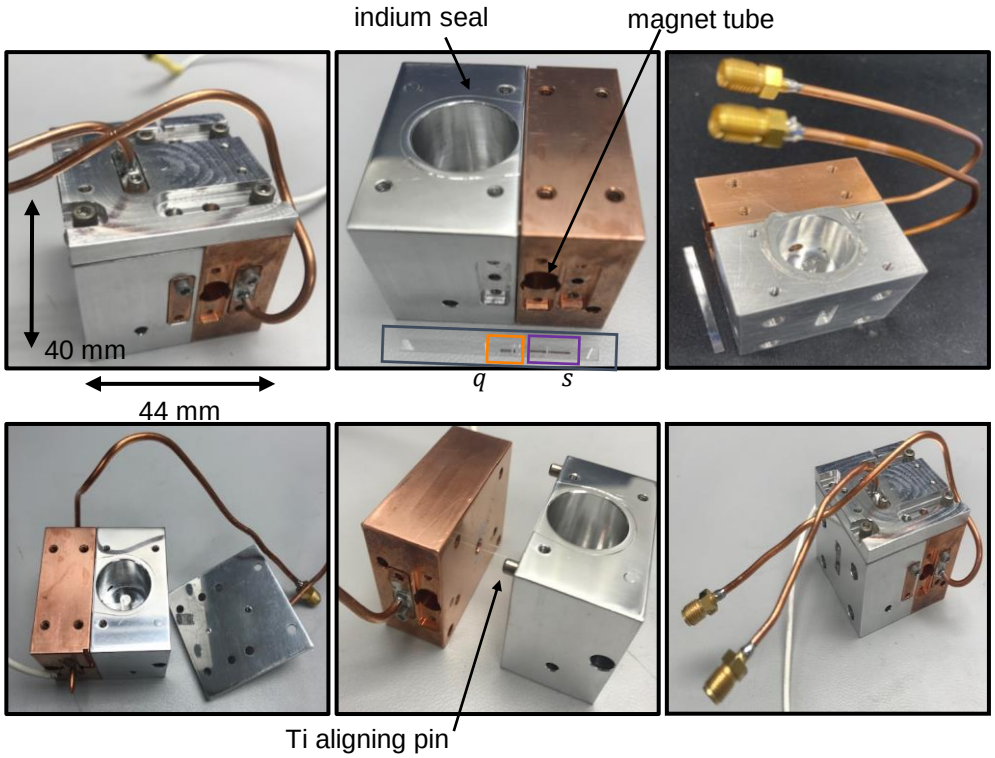


Figure 26: **Photos of device** The cavity housing was machined out of 6061 superconducting aluminum. The adjoining copper block is made of OFHC with a tube opening perpendicular to the cavity. The microwave ports are designed to be 50 Ω with stripped copper cable, so the pin length is variable. An indium seal gasket surrounds the top of the cavity to fill any gaps at the cavity-lid interface. The sapphire chip is held in place with a molybdenum screw. Titanium dowel pins are used to align the Al-Cu joint. The slit for the chip (which spans the Al and Cu, and must go through the central $\lambda/4$ cavity post) is laser cut to be precise and made in a singular cut to be perfectly aligned.

## 4.2 Frequency Domain Measurements

The sample chip (Fig. 26) was fabricated with all aluminum, single step nanofabrication and cooled on the base stage of a dilution refrigerator (Fig. 27). We first measure the SNAIL's parameters in reflection to choose the bias conditions needed to have high $g_3$ and low $g_4$. This is done with single-tone spectroscopy of the SNAIL mode with a varying external flux bias. Port 1 of the VNA is connected to the SNAIL's input line, and Port 2 to the output line after a low-noise room temperature amplifier (MITEQ). The VNA is used to send a range of frequencies into the sample and detect changes to the reflected signal it receives back. In the correct frequency range, this will excite the SNAIL mode. Throughout this thesis, as is the case in experimental work, when I refer to the properties of each mode, it is not the 'bare' mode. The couplings between modes leads to a re-diagonalization of the Hamiltonian and each mode is re-normalized with respect to other circuit modes. In this section, for example, I refer to the SNAIL's dressed parameters. This is quite different than the behavior of a bare SNAIL, alone in a circuit.

A flux sweep is performed by setting the VNA frequency span to a window that shows the SNAIL mode as it varies in frequency. This variation is caused by changing the external flux $\Phi_{ext}$ threaded through the loop of superconducting Josephson junctions, and thus changing the balance of inductive energy moving around the loop. We send a small current through the cylindrical magnet positioned over the SNAIL, which creates a perpendicular magnetic field to change the local flux. Figure 28 shows the SNAIL going through multiple flux quanta $\Phi_0$ variation.

A few useful parameters can be extracted from Fig. 28. We fit each individual VNA trace (in this colorplot a vertical line cut at one applied current) to find the frequency of the SNAIL mode, which should be $\propto |\cos \Phi_{ext}|$. Each trace also tells us how the decay rate of the SNAIL $\kappa_s$ varies with $\Phi_{ext}$. An individual trace extracted from Fig. 28 is defined in Fig. 29

Crucially, the nonlinearity coefficients of the SNAIL mode can be extracted by fitting to an ideal SNAIL model knowing the $f_s(\Phi_{ext})$ relationship and constant parameters like the capacitance, linear inductance, and Josephson junction properties. The $4^{\text{th}}$ order coefficient

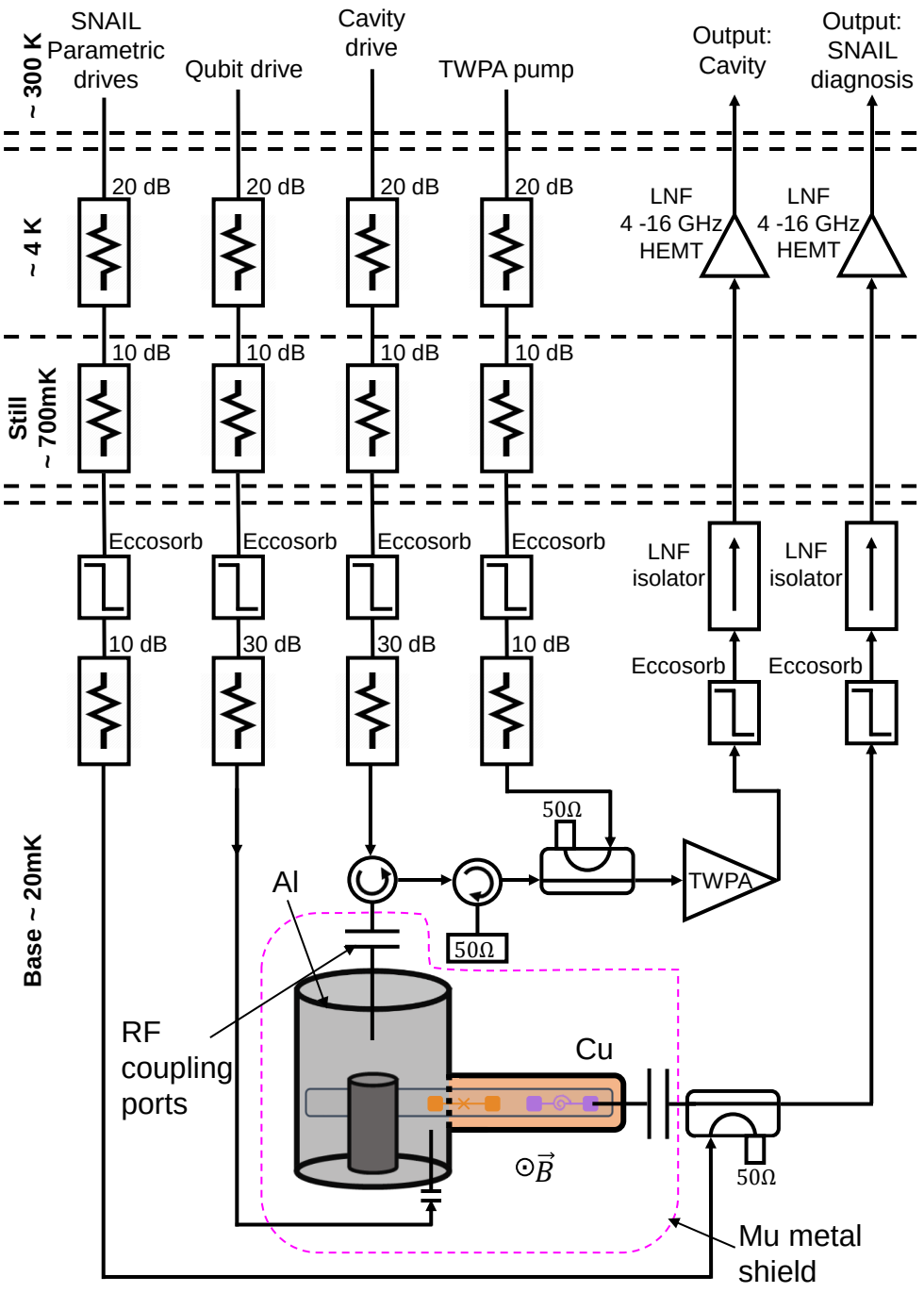


Figure 27: **Cryogenic diagram** A diagram of the full cryogenic input and output setup for our bath engineered qubit. The SNAIL is directly probed and the parametric drives are sent down the left-most input line. When the SNAIL is directly measured (for diagnostics), it is read in reflection. The qubit is driven through its 'weak port'. The cavity is driven and readout in reflection, with the signal out of the cavity passing through a TWPA before going through a cryogenic isolator at the base stage and a HEMT amplifier at the 4K stage.

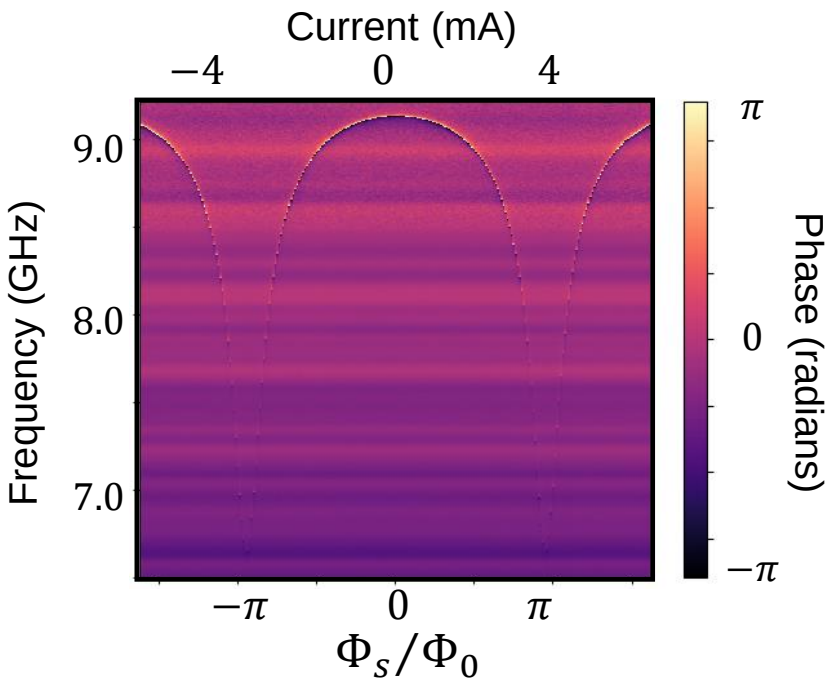


Figure 28: **SNAIL mode flux sweep** Single tone spectroscopy for the SNAIL mode. Weakly probing it in reflection on the VNA, we sweep the external flux driven through the loop of Josephson junctions. This is achieved by sweeping the current sent through a cylindrical magnet placed above the SNAIL's loop. Changing $\Phi_s$ changes the frequency and nonlinearity of the SNAIL. For this experiment, we operated near $\Phi_s/\Phi_0 = -\pi/3$ and $f_s = 8.009$ GHz.

can be experimentally verified with a power-dependence sweep. Josephson junction based amplifier(-esque) modes act like duffing oscillators [90] under high drives.

To perform a 'Duffing sweep,' we again measure the SNAIL's frequency response in reflection on the VNA, as well as send in a second continuous tone down the same input line. This tone should be detuned from $f_s(\Phi_{ext})$ (typically $5-10\times\frac{\kappa_s}{2\pi}(\Phi_{ext})$) so as not to resonantly excite it. We sweep the input power of the detuned drive to induce a frequency shift with respect to power. If the mode decreases in frequency with increased power, the $4^{\text{th}}$ order coefficient, or self-Kerr, of the mode is negative (from a Hamiltonian term $\propto n_d K_{ss} s^\dagger s$ for $n_d$

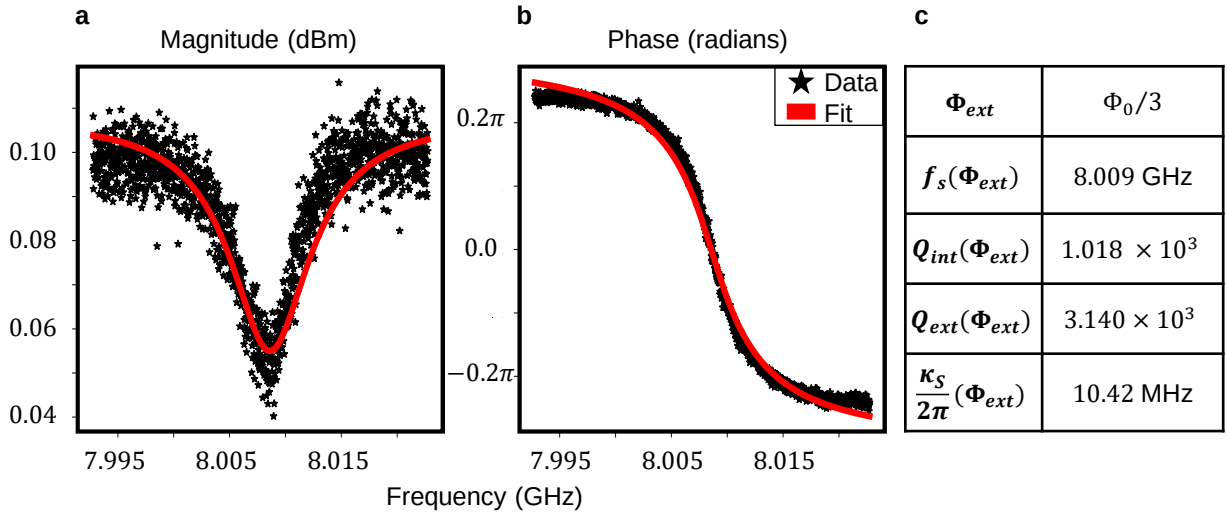


Figure 29: **SNAIL mode at** $g_4 \approx 0$ The reflected signal of the SNAIL mode as measured on a VNA. (a) Magnitude in dBm. (b) Phase in radians. (c) The fit parameters extracted from (a) and (b). The external bias condition was set to a point of nearly Kerr-free operation and the frequency, $Q_{int}$, and $Q_{ext}$ can be fit in reflection.

photons). Likewise if the mode increases in frequency with increased power, the self-Kerr is positive. For this experiment, we wish to operate at a point of $4^{\text{th}}$ order null so we operate at a current bias with minimal frequency bending under this drive. In Fig. 30 the SNAIL's nearly-Kerr-free bias condition was at 8.01 GHz.

At the appropriate SNAIL bias, the cavity mode can be measured with single-tone spectroscopy in a similar way. Typical cavity measurements for this experiment are: $f_c = 6.966$ GHz and $\frac{\kappa_c}{2\pi} = 0.768$ MHz.

Finally the qubit mode must be found in frequency space. A relatively simple first step is 'continuous wave spectroscopy:' measure the cavity's reflection response on the VNA and sweep a second continuous tone on the qubit drive line. If this drive frequency matches the $|i\rangle \leftrightarrow |i+1\rangle$ transition, it will excite that qubit mode, as shown in Fig. 31. Increasing the strength of this tone can also excite other transitions of the qubit, and so CW spectroscopy is a useful method to learn the qubit's frequencies and anharmonicity $\alpha_q$. Typical qubit

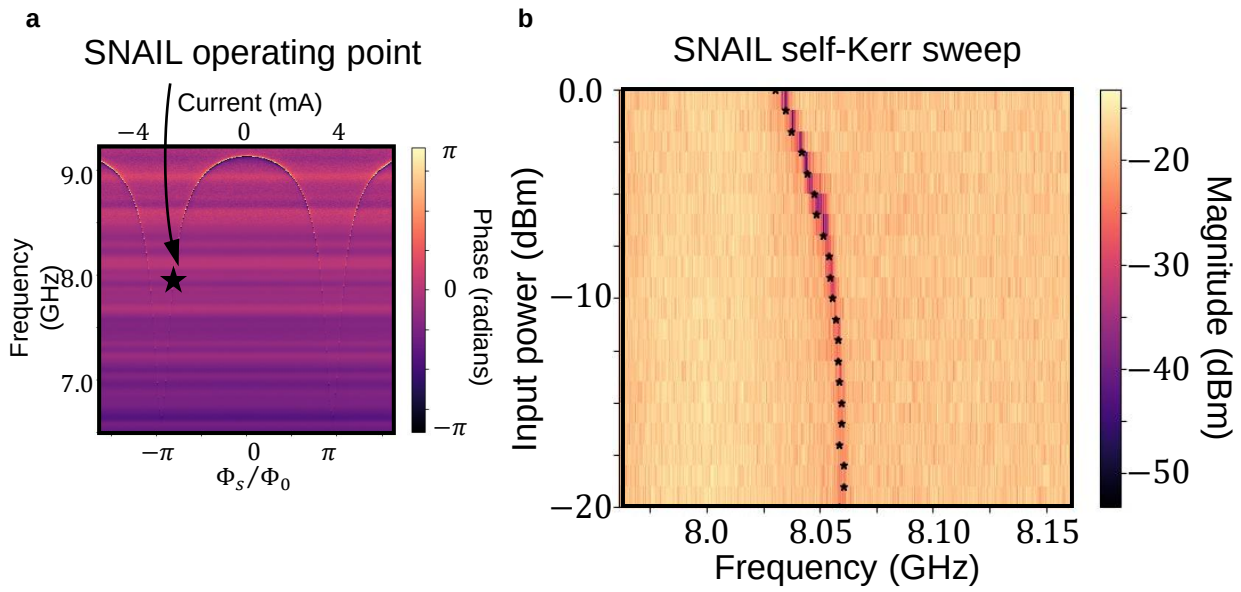


Figure 30: **SNAIL mode at operating bias** At the operating external flux bias (a), we sweep the power of a positively detuned second input tone while weakly probing the SNAIL. (b). Duffing oscillator-like behavior indicates the degree of $4^{\text{th}}$ order nonlinearity in the mode. This particular bias has a small negative self-Kerr.

measurements for this experiment are: $f_{q,ge} = 4.519$ GHz, $f_{q,\ gf/2} = 4.42$ GHz, $f_{q,ef} = 4.321$ GHz, and so $\frac{\alpha_q}{2\pi} = -198.6$ MHz.

CW spectroscopy can be avoided all together if you wish to move directly into time resolved, pulsed measurements. The above frequency-domain qubit measurements are useful if trying to get a rough idea of the system's frequency landscape, the qubit frequency is unknown, and your room temperature electronics are not limited to a small band of frequencies.

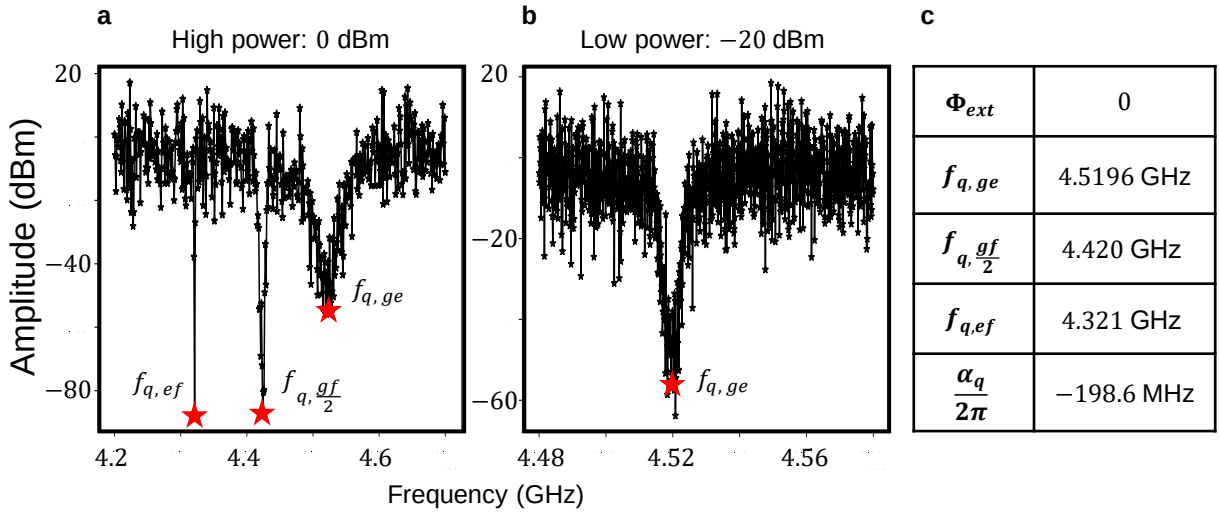


Figure 31: **Qubit spectroscopy** (a) High qubit drive power (b) Low qubit drive power (c) Frequency parameters of qubit. While weakly probing the cavity on the VNA at its resonant frequency, we sweep the frequency of a second tone down the qubit's transmission line. If that frequency matches one of a qubit transition, it will excite the qubit and appear as a dip in amplitude. When the qubit drive tone is strong (a), multiple modes are excited. When weak (b), only the lowest order $|g\rangle \leftrightarrow |e\rangle$ process will be excited.

### 4.3 Time Domain Measurements

With a full mapping of frequency space, we may now move on to time-resolved, pulsed measurements. For all drives in the bath engineering project, an arbitrary waveform generator (Tektronix 5014C) with sampling rate 1.0 GSa/s was used to generate the I and Q signals fed into an IQ-mixer (Marki IQ0618). The LO was fed by an RF signal generator (SignalCore SC5511A). The mixer's RF signal was sent to the appropriate input port at the room temperature stage of the dilution refrigerator. Signals coming out of the fridge, from either the readout cavity or SNAIL, were mixed down to 50 MHz using an IR-mixer (Marki IR4509) whose LO also comes from the same signal generator as the input mixer's. This signal is recorded using a fast ADC card (AlazarTech).

The cavity input was driven using a 50 MHz upper sideband. This was chosen because the digitizer records siganls at 50 MHz, so only a single SignalCore generator was needed to supply both input IQ- and output IR-mixers. This allows us to perform interferometric readout, where the signals coming out of the fridge/sample are compared to those that were routed directly from the generator to the readout mixer. For the cavity at 6.966 GHz, the generator is set to 6.946 GHz.

Using the pulse sequences in Fig. 32, average qubit values measured were: $f_{q,ge} = 4.52$ GHz and $\frac{\alpha_q}{2\pi} = -198.6$ MHz, with average coherence times $T_1 = 15.452$ $\mu$s, $T_{2,\,R} = 8.172$ $\mu$s, and $T_{2,\,E} = 8.693$ $\mu$s. The data shown in Fig. 33(a-e) are the typical measurements taken to characterize the qubit, with findings summarized in (f). We note frequency detuning errors in Fig. 33(e). This is not fatal, as even an imperfect $\pi$ pulse can sufficiently excite the qubit to accurately measure its dynamics. Additionally, not all experiments require a direct qubit drive. Heating between $|g\rangle$ and $|e\rangle$, for example, starts with preparing the qubit in the ground state, or doing nothing and waiting sufficiently long between pulses to ensure the qubit has decayed to the ground state, $\mathbb{I}$. But for experiments that call for qubit preparation, like $T_{1,\,2}$, cooling $|e\rangle \rightarrow |g\rangle$, etc., the qubit was driven using an 80 MHz upper sideband mixed to $f_{q,ge}$ with the IQ mixer.

To increase readout fidelity and perform single-shot readout with low averaging and low input power, we backed the readout cavity with a Travelling Wave Parametric Amplifier (TWPA) [92] provided to us by MIT Lincoln Laboratory. This broadband amplifier is continuously pumped with an RF tone chosen to give 20 dB gain at the cavity's frequency. The TWPA allowed us to perform multi-state readout because each state in the IQ-plane became better separated. Each qubit state's Gaussian blob was pushed out from the origin, so we could perform state discrimination to decide the qubit's state after the parametric pump. For example on the left of Fig. 34, when the TWPA is off (or rather the pump is not supplied), the qubit's amplitude and phase information of each state is unclear because of strong overlapping in the Gaussian histogram. However with the TWPA on /pumped on the right, we can much easier infer qubit states with well-defined blobs for each excitation, see Fig. 34(b). This is crucial for our experiment because we must be able to find the up- and down-going rates of the qubit between adjacent levels, and therefore must have a clear

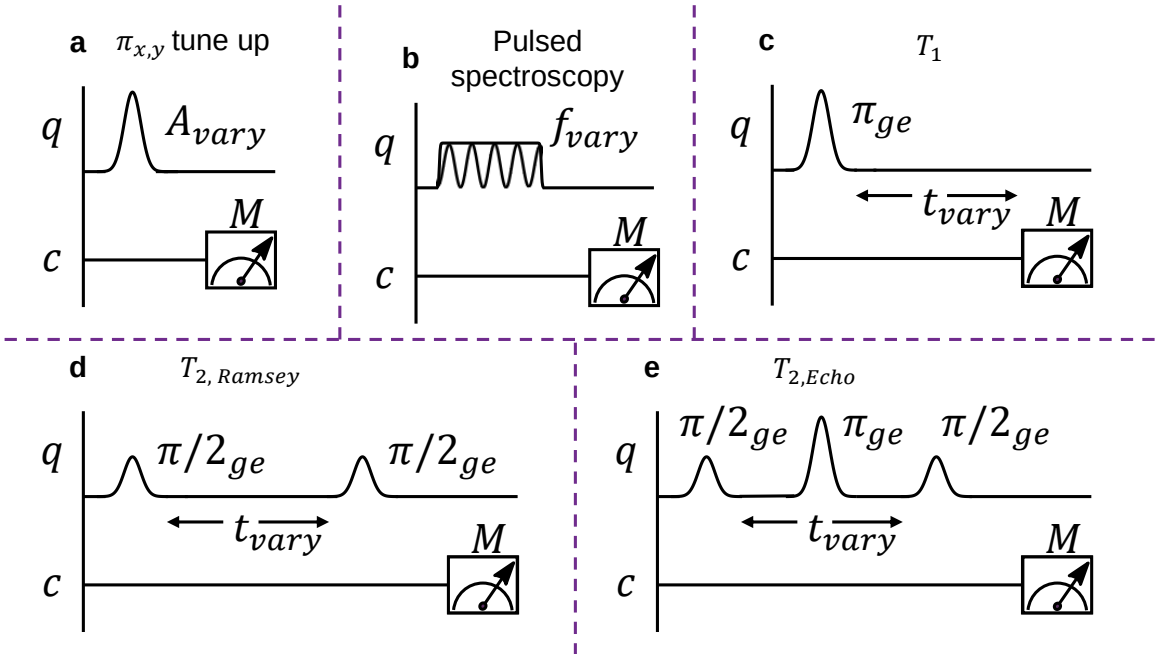


Figure 32: **Basic qubit pulse sequences** The microwave pulse sequences typical for characterizing qubit performance. (a) **$\pi$-pulse tune up.** Apply a Gaussian pulse on the qubit channel at the appropriate qubit frequency and measure the cavity. With each repetition, vary the amplitude of the Gaussian pulse, to find what amplitude appropriately excites the qubit to cause the cavity response to be most unique from its starting point. (b) **Pulsed spectroscopy.** Apply a variable frequency flat top pulse to the qubit channel. Whatever is the correct qubit frequency, will excite the qubit and shift the cavity's response by $\chi_{qc}$. (c) $T_1$**.** With the chosen $f_q$ and $A_\pi$, apply a Gaussian to the qubit channel and measure. With each repetition, increase the wait time between Gaussian and measurement. The qubit state measured per time should decrease to $|g\rangle$ with a characteristic time constant $T_1$. (d) $T_{2,\ Ramsey}$. Apply two $\pi/2$ pulses, spaced by variable time $t_{vary}$. This prepares the qubit on the equator, allows phase evolution, and then projects the qubit onto the measurement axis. If the drive frequency is detuned from true qubit frequency or there is low frequency noise, the signal will oscillate and produce 'Ramsey fringes'. (e) $T_{2,\ Echo}$. Same pulse sequence as $T_{2,\ R}$ except add an additional $\pi$ half way between the $t_{vary}$ period. This 'echoes' low frequency noise by flipping the qubit to the opposite equatorial axis. This removes sensitivity to detunings and indicates other sources of dephasing.

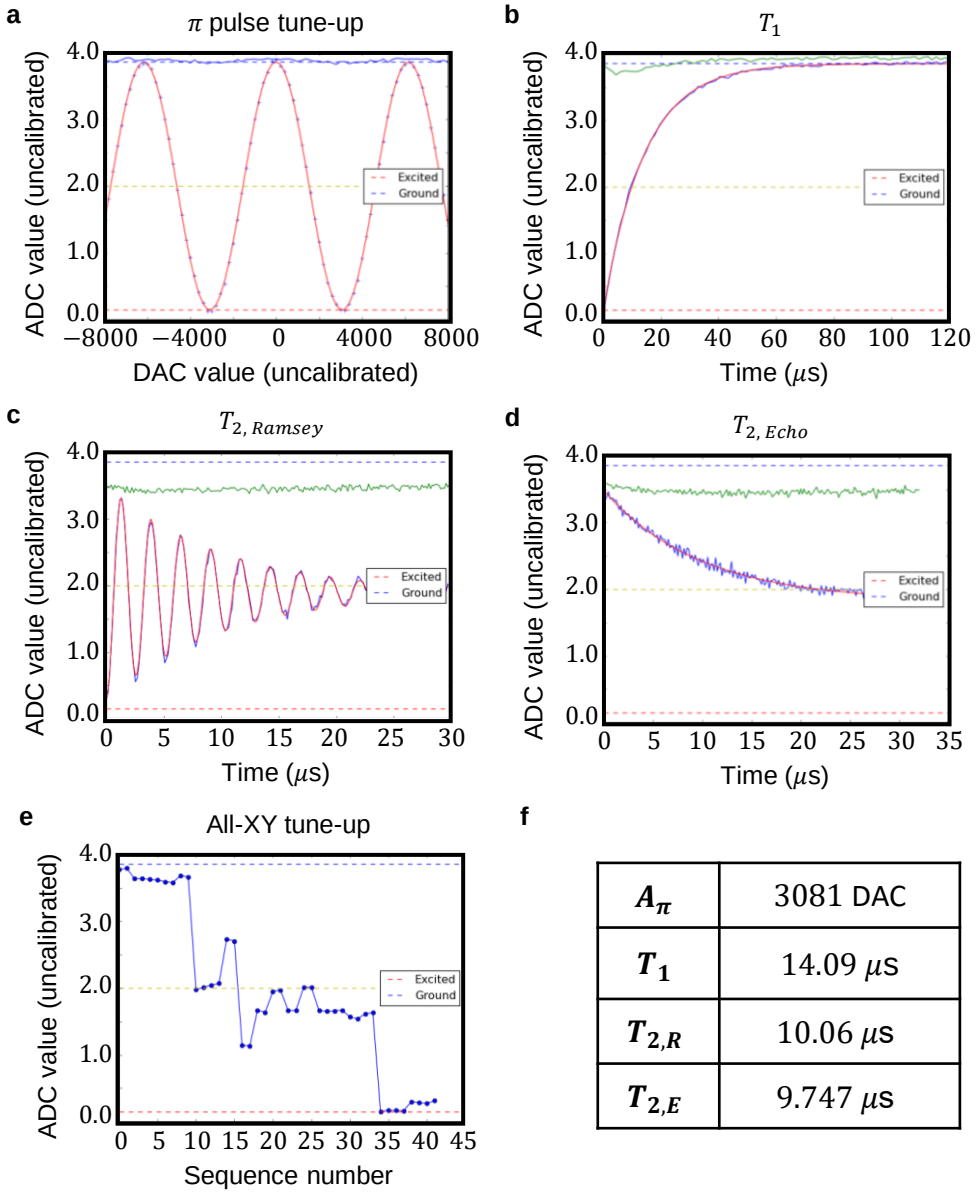


| | |
|---|---|
| $A_\pi$ | 3081 DAC |
| $T_1$ | 14.09 μs |
| $T_{2,R}$ | 10.06 μs |
| $T_{2,E}$ | 9.747 μs |

Figure 33: **Typical qubit measurements** (a) **$\pi$-pulse tune up.** This determines the voltage necessary to drive the qubit from pole to pole of the Bloch sphere. (b) $T_1$ **measurement.** The energy decay time constant. (c) $T_{2,\,R}$ measurement. Phase decoherence susceptible to low frequency noise. (d) $T_{2,\,E}$ measurement. Phase decoherence with low frequency noise echoed out. (e) **All-XY measurement.** A sequence of 21, 2-pulse measurements to determine the quality of qubit drive parameters. The error syndrome shown here indicates frequency detuning. See Ref. [91] for greater detail on this method. (f) Measured qubit parameters.

mapping of the qubit's behavior between each state vs. time, including $|f\rangle$ and beyond.

Before each parametric pulse and measurement we defined our qubit state discrimination to pick out, before the experiment ran, a known IQ-plane basis. This was done by applying a series of drives to the qubit that would result in a well-predicted population distribution so we could assign later results to those same sections of the IQ-plane. Our discrimination sequence was $\frac{\pi_{ge}}{2}, \frac{\pi_{ef}}{2}$, then $M$ measure the cavity state. After this, we waited 3 $\mu$s to empty the cavity, prepared the qubit in the necessary state, applied the parametric pump for variable time, and again measured the cavity. This time the resulting measurement had context- if the measurement after the parametric process landed in a particular section of the plane that had been assigned to a particular state, we were more confident that the qubit was truly in that state.

A final note before describing the engineered bath: frequency crowding. Finite frequency modes must be carefully separated so as to avoid collisions with other modes, and any drive imparted on the system should not excite some unwanted or unintended mode. There are many order terms in our Hamiltonian which can be parametrically driven. Terms with $n$ number of operators can act via $m$ pump photons and produce anywhere from $n-1$ to $n-m$ lower order parametrically driven tones. For example in Ref. [93], an $n = 4$ wave qubit term uses $m = 3$ to produce 1 photon. All of the modes involved must be either too weakly coupled or too far off resonance to not interfere with the modes we do wish to parametrically mix. This applies to multiples of mode frequencies as well. For example if the cavity mode were frequency $f_c$, the SNAIL pump $f_d$ should not be $Xf_c, f_c/X$, etc. for integer $X$. Unwanted processes can also arise from tone combination. If our SNAIL was truly only third order nonlinear, this would not be an issue. However, this is only an approximation and so we must take care in choosing our frequencies.

### 4.3.1 Natural Decay of Transmon Qubits

A qubit's bath is engineered, or controlled, if the populations of different states and the rate of movement between states is certainly controlled. This calls not only for good state separation (see above discussion), but also for the ability to quantify the rate of transition

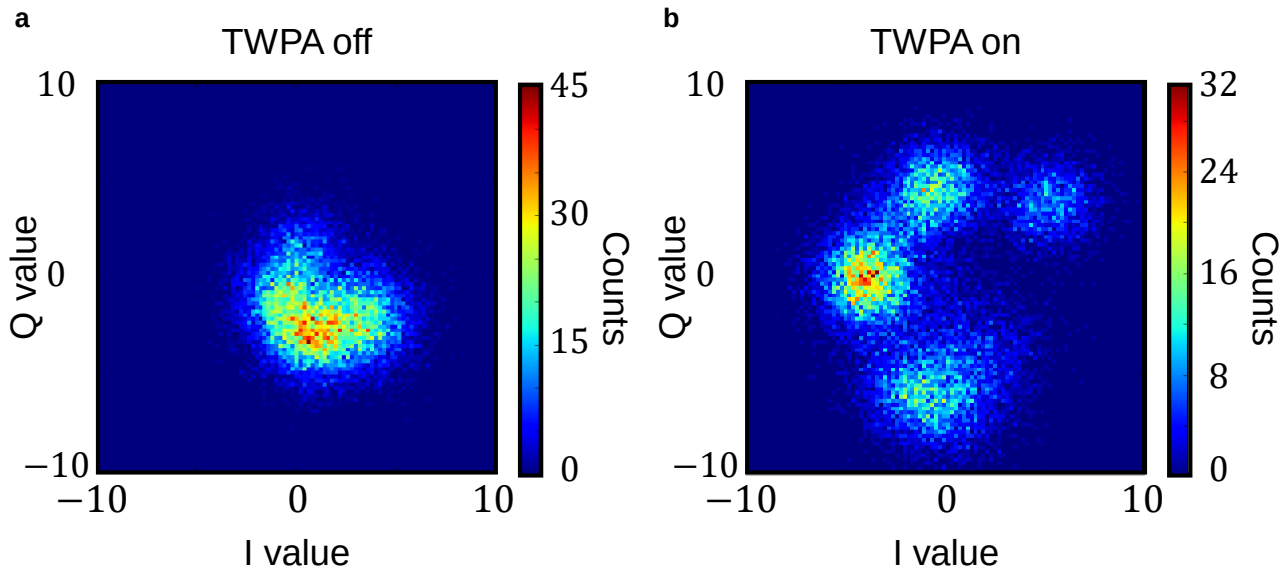


Figure 34: **Measuring the qubit with a backing amplifier** The qubit was prepared with two $\pi$-pulse: $\pi_{ge}$ and $\pi_{ef}$ and measured. (a) Histogram measurements of the cavity's state under the qubit drive sequence with the TWPA off. With this number of averages and measurement time, it is impossible to discriminate the qubit's states. (b) The same measurement repeated, but with the TWPA on. Now it is much easier to understand what IQ-plane values correspond to what qubit excitation. This measurement also highlights a feature of this experiment that will cause trouble later: the qubit appears to rotate in the IQ-plane after some time.

between states, going both up and down the transmon's anharmonic ladder. We can compare our parametrically-driven rates to the 'natural' rates of the transmon. If a transmon, or any oscillator with addressable levels, is prepared in a known state, we can measure the decoherent evolution as it transitions to an adjacent state. In this undriven case, the downward evolution is due to energy decay, and upward due to thermal heating.

The data shown in Fig. 35 was taken with the transmon and cavity from this project, but this method can be generalized to any qubit-cavity as there was nothing special about

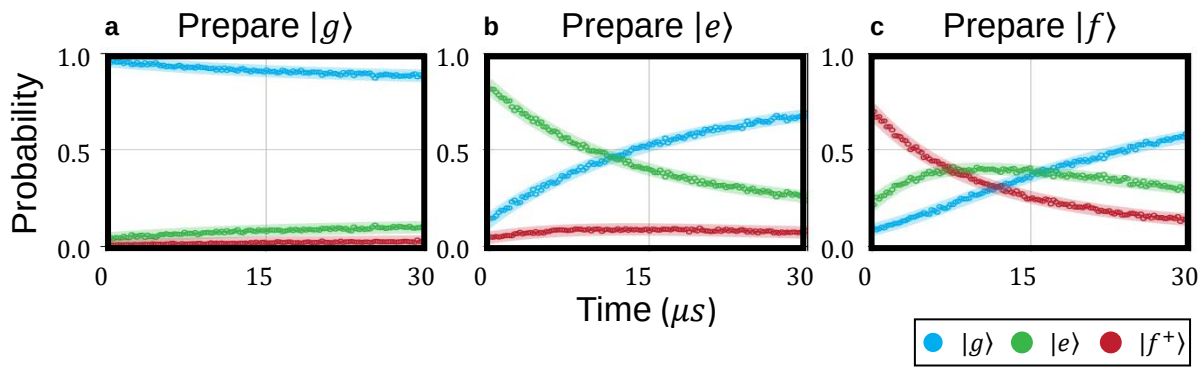


Figure 35: **Natural decay of the transmon** In each panel, the qubit is prepared to the state indicated, and then measured vs. time. Rates are fit with an exponential model following Eqs. 76. (a) Prepare $|g\rangle$ (b) Prepare $|e\rangle$ (c) Prepare $|f\rangle$

this set up. The qubit was prepared in $|g\rangle$, $|e\rangle$, or $|f^+\rangle$ and measured vs. time, there were no extra pulses applied. The state evolution can be mapped to a three-level exponential model:

$$\begin{aligned}
\dot{P}_g &= -\Gamma_{ge} P_g + \Gamma_{eg} P_e \\
\dot{P}_e &= \Gamma_{ge} P_g - (\Gamma_{ef} + \Gamma_{eg}) P_e + \Gamma_{fe} P_f \\
\dot{P}_f &= \Gamma_{ef} P_e - \Gamma_{fe} P_f
\end{aligned} \tag{76}$$

For the undriven cases shown in Fig. 35, we extract the following rates: $\frac{\Gamma_{ge}^{\text{natural}}}{2\pi} = 1.37$ kHz, $\frac{\Gamma_{eg}^{\text{natural}}}{2\pi} = 8.02$ kHz, $\frac{\Gamma_{ef}^{\text{natural}}}{2\pi} = 2.28$ kHz, and $\frac{\Gamma_{fe}^{\text{natural}}}{2\pi} = 11.26$ kHz. These rates are a consequence of the qubit-bath coupling and are not controlled in any way, other than the steps taken to increase qubit lifetimes and decrease physical temperature. A hot qubit will have increased natural up rates, as it thermalizes to its bath faster. While the qubit thermalization rates shown here are largely out of our control, this does not have to be the only case. In the following sections, I will show how we can enhance these rates using parametric drives, and later another experimental application of this concept.

### 4.3.2 Transmon Heating

When a transmon is physically heated, the populations in $|e+\rangle$ increase, in accordance with

$$P_n = \frac{e^{-E_n/k_BT}}{Z} \tag{77}$$

for a particular state $n$ where $Z$ is the partition function :

$$Z = \sum_{n=1}^{N} e^{-E_n/k_BT}. \tag{78}$$

However when changes to the physical temperature $\mathrm{T_{phys}}$ are the cause of population changes, this process is not easy to control. In the following section, I will demonstrate how to reliably create an increased excited state(s) population transmon with parametric drives.

Our transmon is heated by driving a parametric gain-type process through the coupled three-wave mixer SNAIL. I will start with describing the simplest case: heating from $|g\rangle$ to $|e\rangle$. We do not apply any drive directly to the qubit. Instead we prepare $|g\rangle$ by idling ($\mathbb{I}$) and apply the $\Sigma_{s,ge}$ pulse to the SNAIL. This parametric process generates a qubit photon, leading to an effective parametric up rate of $\Gamma^p_{ge}$. This is different than a $\pi$ -pulse-type excitation because a $\pi$ also brings the qubit back down to $|g\rangle$ from $|e\rangle$. Whereas our parametric drive only excites the qubit up with each 'reset' of the parametric $\Sigma_{s,ge}$ protocol. Therefore $\kappa_s$ is the ultimate limit on $\Gamma^p_{ge}$.

With a ground state qubit, we drive the $\Sigma_{s,ge}$ process by pumping on the SNAIL mode at $f_d = f_s + f_{q,ge}$ to bring the qubit from $|g\rangle$ to $|e\rangle$, with parametric driving rate $g_{\Sigma_{s,ge}}$. We apply this pump for a variable length, see Fig. 36(a), and then measure the cavity to dispersively readout the qubit. The efficacy of the inversion pump can be changed with a handful of in situ parameters: $f_d$ (which can be varied by $f_s + f_{q,ge} + \gamma_d$), and $g_{\Sigma_{s,ge}}$, which is a function of $\eta_d(t)$, $f_s$, and $g_3$.

For a fixed $f_d$, $f_s$, and $g_3$, we can change the drive strength (achieved by changing the voltage sent down the SNAIL's input line at room temperature) to alter the rate at which the qubit thermalizes its population to the first excited state, as well as the population

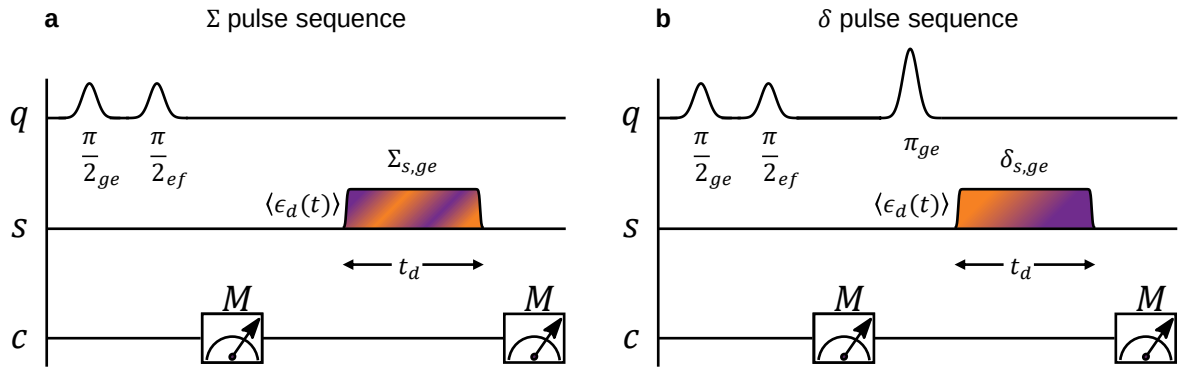


Figure 36: **Pulse sequence for single parametric processes** (a) For transmon heating, we perform the discriminatory qubit pulses and measure to define the IQ positions of each qubit state, briefly idle, and then apply $\Sigma_{s,ge}$ for varying time. We then measure the qubit state vs. time to measure the efficacy of the parametric pump. (b) For transmon cooling, we perform the same initial sequence, but instead this time prepare the qubit in $|e\rangle$ before applying $\delta_{s,ge}$ for varying times.

distribution caused by the drive. In Fig. 37, the drive strength is increased from left to right and we note a drastic increase in the rate of $|g\rangle$ to $|e\rangle$ in comparison to the natural rate $\frac{\Gamma_{ge}^{\text{natural}}}{2\pi} = 1.37$ kHz. This one-dimensional sweep is performed at a single pump frequency, but that is not the only $f_d$ that could have been chosen. In Fig. 38, we vary both the amplitude and frequency of the parametric drive. This shows an entire mapping of drive conditions to up-rates. Typically higher powers correspond to higher inversion rates, but can lead to drive saturation. This can be caused by driving the SNAIL too hard [94] and/or physically heating the components of the drive line [95] which limits output performance.

The classical component saturation in Fig. 39 shows a dramatic slowing of output amplitude per input amplitude, where increasing the AWG's DAC input reference voltage no longer buys an increase in peak output. This can be caused by supplying too great a power to the mixers or input amplifier. Additionally, the SNAIL itself does seem to saturate, too. Figure 40(a) shows the rates $\Gamma_{ge}^{p}$ (black) and $\Gamma_{eg}^{p}$ (red) for increased input voltage. In the

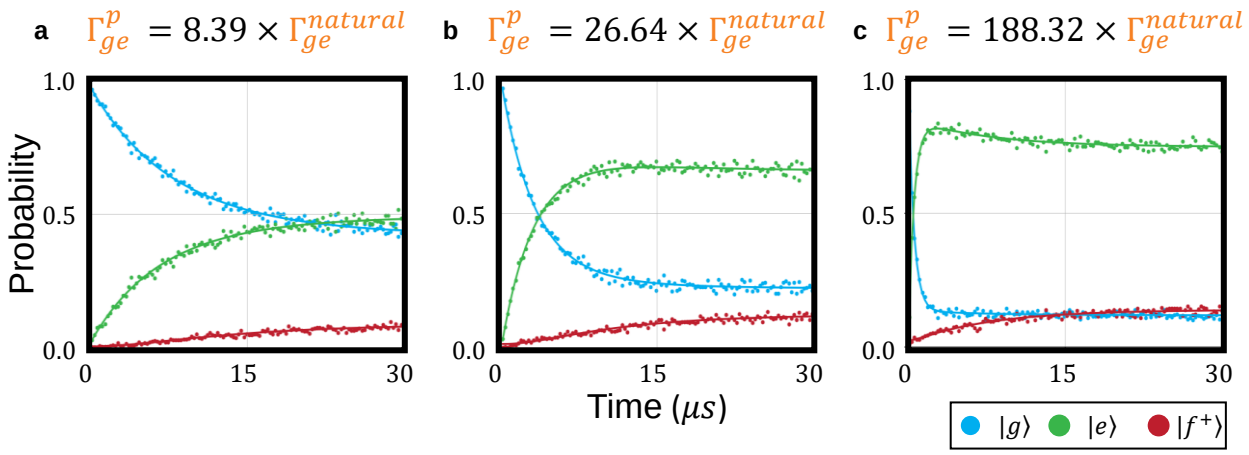


Figure 37: **Transmon heating** The transmon was initially prepared in $|g\rangle$ and the $\Sigma_{s,ge}$ strength is swept by varying DAC reference voltages (a) 0.5 V (b) 0.75 V and (c) 2.75 V. In each plot, the time of the pump is swept over the horizontal axis. The solid lines represent fits using Eq. 76 to fit the rates to and from each qubit state.

heating process where we wish to change $\Gamma_{ge}^{p}$, we do not see any major decrease in the rate with increased input voltage up to the input saturation point of 2.75 V. The solid black line is a quadratic fit $\propto V^2$ for the heating rate.

### 4.3.3 Transmon Cooling

A transmon in a cold bath will also follow Eq. 77 with $T \to 0$, causing the population to approach $|g\rangle$. Similarly to the case with physical heating, when a transmon is physically cooled, it is difficult to control the rates or final population distribution- the qubit evolves at a rate determined by the bath temperature and qubit-bath coupling strength, and ends at the final distributions based on Eq. 77.

For parametrically controlled transmon cooling between $|e\rangle$ and $|g\rangle$, the qubit is initially prepared in the first excited state with a $\pi_{x,y}$-pulse, and then $\delta_{s,ge}$ is applied to the SNAIL. This drives a conversion or beam-splitting process that converts a qubit mode photon to a

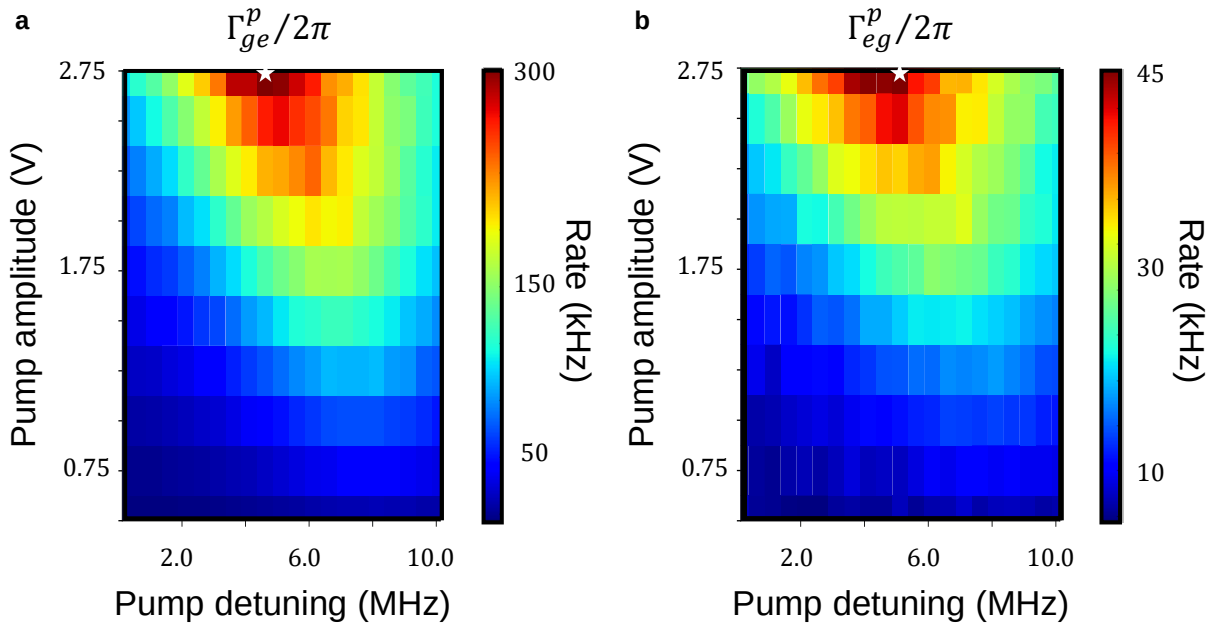


Figure 38: **Sweep $\Sigma_{s,ge}$ frequency and amplitude.** At a fixed $f_s$ and $g_3$, we sweep both the frequency detuning from 12.526 GHz (horizontal axis) and amplitude (vertical axis) and plot the rate in kHz for (a) $|g\rangle \rightarrow |e\rangle$ and (b) $|e\rangle \rightarrow |g\rangle$. The white star indicates the combination of pump conditions that cause the maximum inversion rate. This colorplot indicates there is not one singular set of driving conditions necessary to successfully operate the transmon heating protocol.

SNAIL mode photon, which then quickly decays leaving both the qubit and SNAIL empty. This process can be measured at an effective parametric down rate of $\Gamma^p_{eg}$. All other rates between adjacent levels are uncontrolled by this singular parametric process, but are still marginally affected in the presence of the strong drive. In Fig. 41, the strength of the drive is increased from left to right. All populations are tracked vs. time and fit to an exponential model, Eq. 76.

Like the heating experiment, here we change the parametric cooling rate by changing the drive strength, absorbed into $g_{\delta_{s,ge}}$ at a particular SNAIL bias and drive frequency $f_d$. The down-going rate induced by the parametric process can be compared to the natural

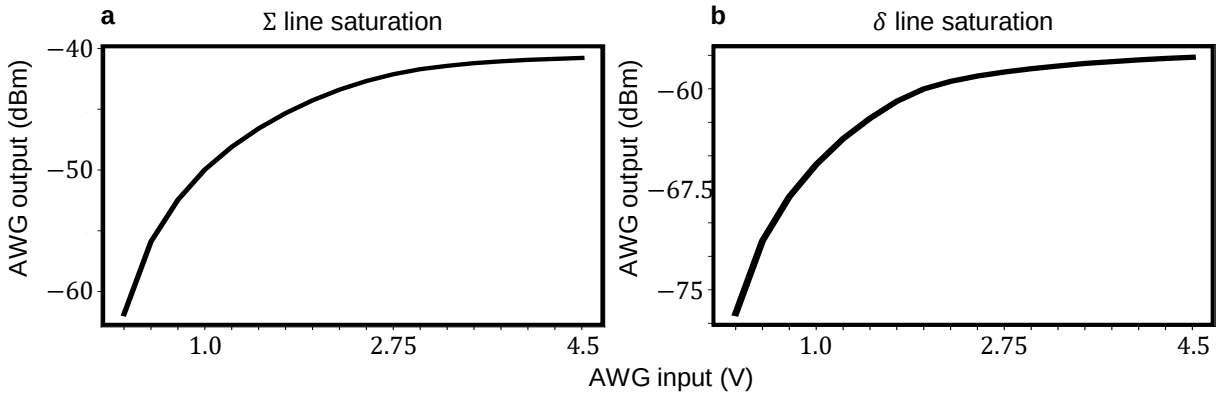


Figure 39: **Saturation of room temperature AWG input** For increased input voltage from our room temperature electronics, the output of the drive begins to saturate and does not necessarily deliver an increased voltage to our sample. (a) The $\Sigma$ line saturates near 2.75 V and (b) the $\delta$ line 1.75 V.

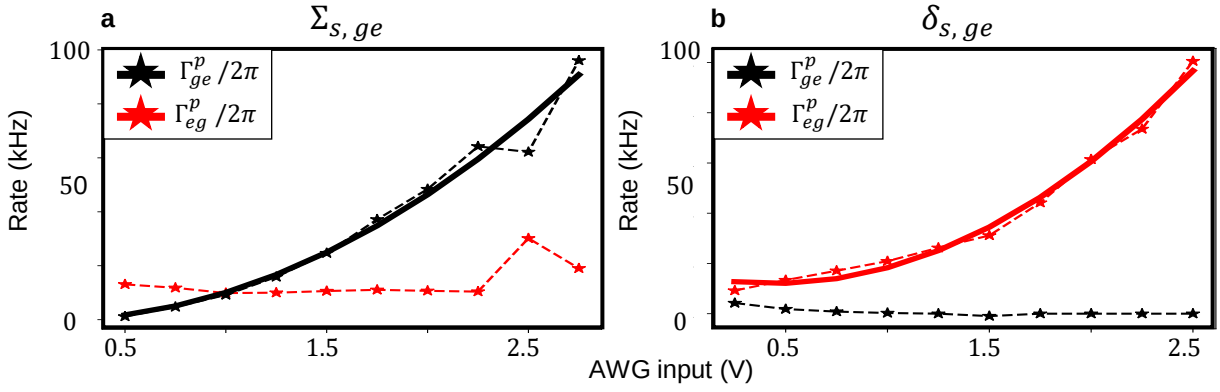


Figure 40: $\Gamma^p_{ge}$ **and** $\Gamma^p_{eg}$ **vs. input voltage**. Data is indicated with stars and dashed lines, and solid lines a fit to $V^2$. (a) For transmon heating $\Sigma_{s,ge}$, the rate of qubit inversion $\Gamma^p_{ge}$ increases quadratically with input voltage, while $\Gamma^p_{eg}$ remains largely unchanged.(b) For transmon cooling $\delta_{s,ge}$, instead $\Gamma^p_{eg}$ increases with $\Gamma^p_{ge}$ constant.

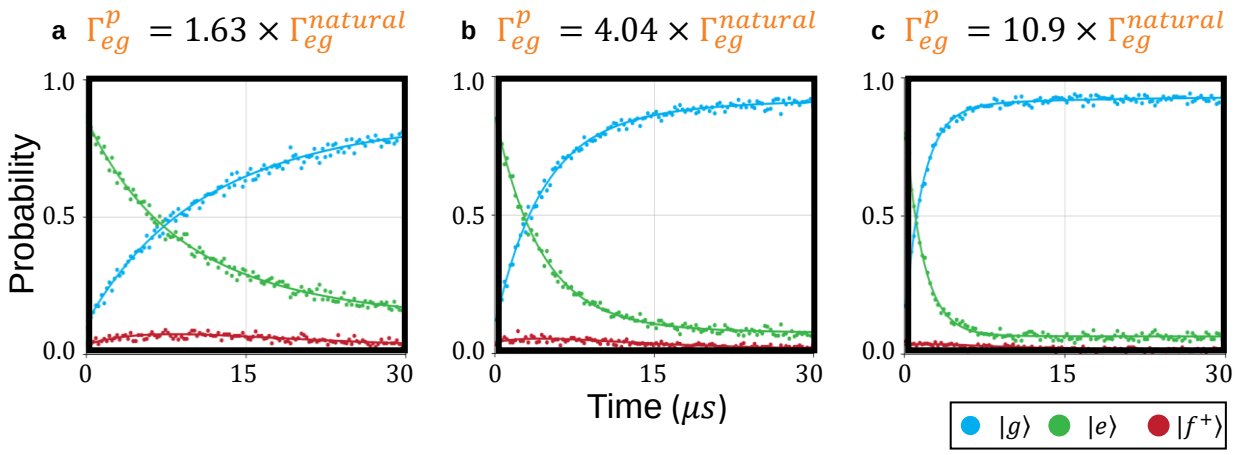


Figure 41: **Transmon cooling** The transmon was initially prepared in $|e\rangle$ and the $\delta_{s,ge}$ strength is swept by varying DAC reference voltages (a) 0.5 V (b) 1.5 V and (c) 2.5 V. In each plot, the time of the pump is swept over the horizontal axis. The solid lines represent fits using Eq. 76 to fit the rates to and from each qubit state

rate $\frac{\Gamma_{eg}^{\text{natural}}}{2\pi} = 8.02$ kHz. Here we see a more modest increase in rates compared to transmon heating. This could be improved by a finer sweep of the multi-dimensional parameter space. Due to the AC-Stark shift, Kerr shift, and physical heating caused by hot injection lines (caused by sending strong drives down them), the drive frequency that may optimally bring the qubit to $|g\rangle$ is not uniform for all drive strengths. To track this, we can perform a 2D sweep of drive parameters $f_d$ and $\eta_d$ and measure the qubit cooling rate. Figure 42 shows that typically with higher drive strength, the rate increases. The process also works over a range of pump frequencies. Within this sweep, we can find a combination of pump frequency and strength to achieve a desired $\Gamma_{eg}^{p}$ and population distribution by tuning $g_{\delta_{s,ge}}$. In this experiment with a single parametric conversion drive, the qubit population is pushed towards $|g\rangle$. This also pushes all other upwards excitations down as well, including the $|f\rangle$ state.

Applying a single parametric drive is straightforward enough- it only requires a single pump RF generator and one input signal (Fig. 36). The one target state can be obtained with a window of pump frequencies and strengths (Figs. 38, 42). However, with only one

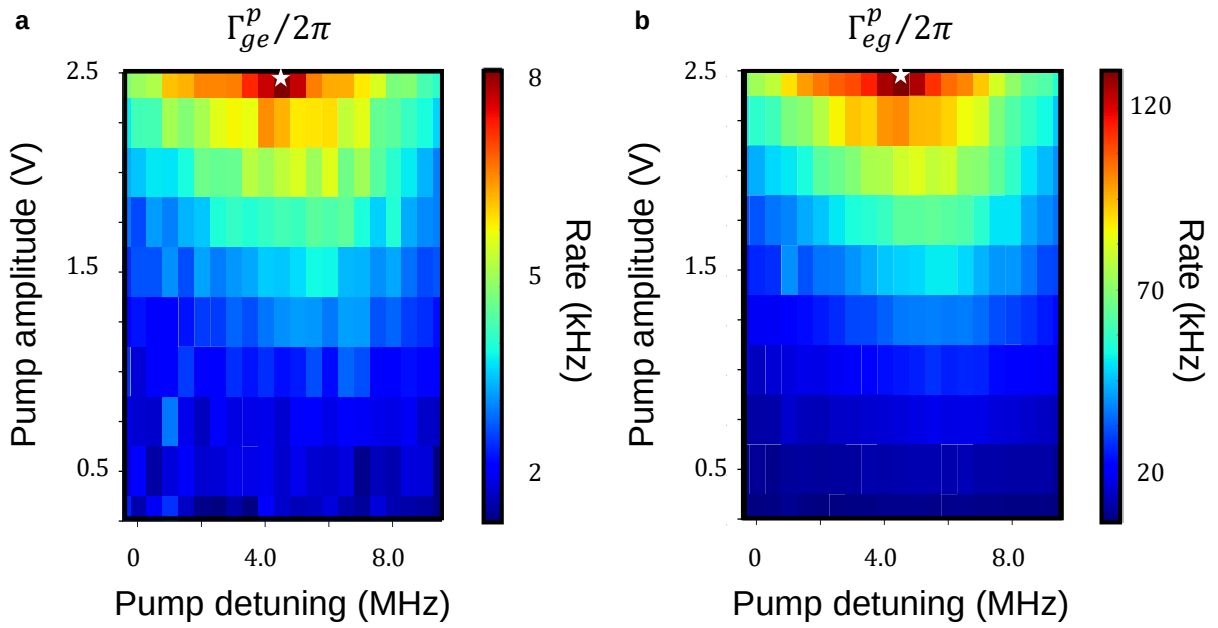


Figure 42: **Sweep $\delta_{s,ge}$ frequency and amplitude** At a fixed $f_s$ and $g_3$, we sweep both the frequency detuning from 3.484 GHz (horizontal axis) and amplitude (vertical axis) and plot the rate in kHz for (a) $|g\rangle \rightarrow |e\rangle$ and (b) $|e\rangle \rightarrow |g\rangle$. The white star indicates the combination of pump conditions that cause the maximum qubit reset rate. This colorplot indicates there is not one singular set of driving conditions necessary to successfully operate the transmon cooling protocol.

drive, we can only control one process, in one direction. We do not have a control knob for any other rate, or what the other non-targeted state populations are. For example if the only drive is $\delta_{s,ge}$, the only steady state population that can be targeted is $|g\rangle$ and the only qubit rate $\Gamma^p_{eg}$.

To fulfill the initial goal of the project, we need the ability to control both up and down rates of the transmon, so as to create a fully controlled bath for qubit photons. We wish to control how states are filled up to a certain level (or create an effective chemical potential), and thus should achieve rate control with parametric drives and not random thermalizations. In the following section, I will describe how this is achieved with multiple parametric pumps.

### 4.3.4 Multiple Parametric Drives

The SNAIL can tolerate multiple pumps that each activate a different parametric process, up to the limit that the drives imparted cause too great a shift to the SNAIL's Josephson junction's inductive energies. In this experiment, we drove 2 simultaneous drives that kept the SNAIL in a safe, operable regime. However in other experiments, more than 2 can be successfully driven for interesting parametric processes [96].

With multiple drives, we can make a system that has a finite chemical potential for photons if we control the filling up to a certain energy level, meaning we control the up- and down-going rates up to that chosen level. See Sec. 3.1.4 for greater detail. Within the $|g\rangle \leftrightarrow |e\rangle$ manifold, 2 pumps (one for up, another for down) let us control $\Gamma^p_{ge}$ and $\Gamma^p_{eg}$ and the population distribution of the qubit within that.

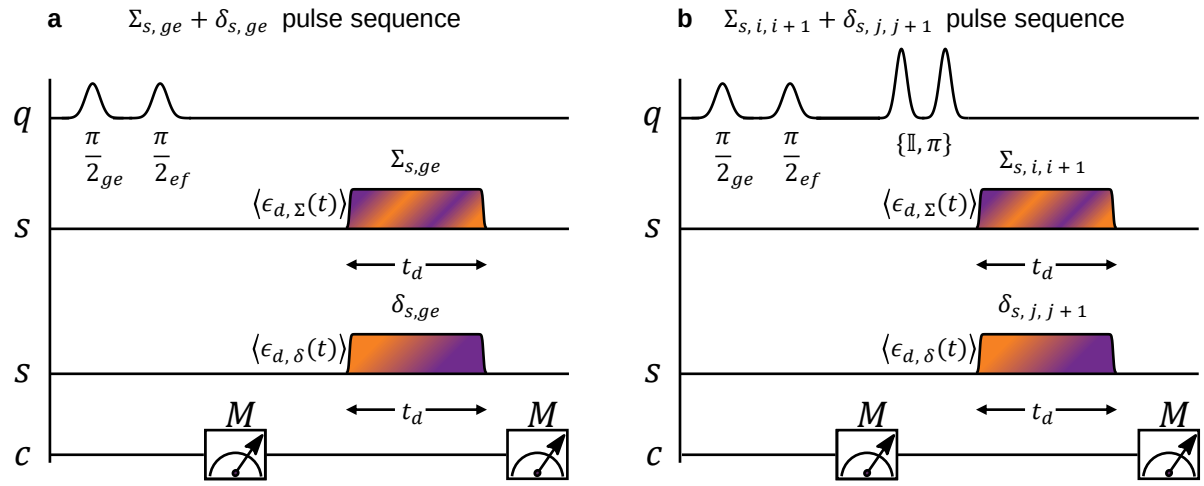


Figure 43: **Pulse sequence for multiple parametric processes** (a) For creating an admixture of $|g\rangle$ , $|e\rangle$, both $\Sigma_{s,ge}$ and $\delta_{s,ge}$ are applied to the SNAIL line for varying time. The cavity is readout at the end of the pulse sequence. (b) This pulse scheme can be generalized for any combination of parametric processes. After the initial qubit state discrimination pulses, the qubit can be prepared in any state, and then multiple parametric pumps can be applied to the SNAIL to heat (between levels $|i\rangle$ , $|i+1\rangle$) or cool (between levels $|j+1\rangle$ , $|j\rangle$).

Simultaneously pumping the $\Sigma_{s,ge}$ and $\delta_{s,ge}$ processes (Fig. 43(a)) allows us to shift the

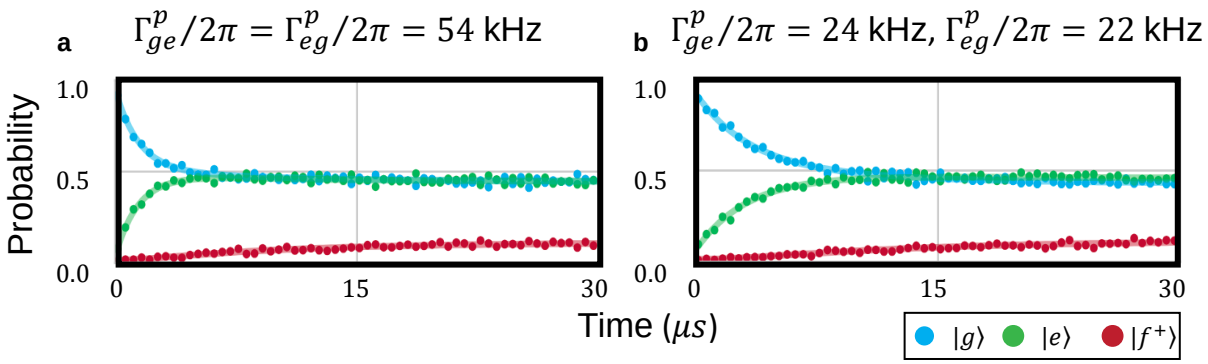


Figure 44: **Balanced $\Gamma^p_{ge}$ and $\Gamma^p_{eg}$** The transmon is prepared in $|g\rangle$ and both parametric processes are modulated at their respective frequencies and pumping rates. We tune both drives to create a qubit that relaxes to a thermally mixed $50\%\,|g\rangle\,, 50\%\,|e\rangle$ state. The same final steady state can be achieved at a rate of choice, here shown at (a) balanced 54 kHz and (b) nearly balanced $24 - 22$ kHz.

rates of qubit transition between the ground and first excited states by changing the pumping rates $g_{\Sigma_{s,ge}}$ and $g_{\delta_{s,ge}}$ for each process. Figure 44 shows how we can create an effective infinite temperature by balancing the rates between $|g\rangle$ and $|e\rangle$. This is achieved by pumping both parametric processes simultaneously, adjusting each strength $g_{\Sigma_{s,ge}}, g_{\delta_{s,ge}}$ accordingly. By modulating the up and down rates parametrically, the qubit's evolution is set by the newly engineered rates so we can also hit targeted steady state population probabilities. For some chosen combination of transition rates and population distributions, Fig. 45 can serve as a guide for pump frequencies.

Any qubit state can be accessed by adjusting the parametric process driven through the SNAIL. Each three-wave process calls for $f_d = f_s \pm f_{q_{i,i+1}}$, a unique drive frequency to actuate each unique gain or conversion. We have already seen the effect of multiple parametric drives which allow us to control the qubit's motion up and down. Extending this idea outside of the qubit's $(|g\rangle\,, |e\rangle)$ manifold, we can readily drive parametric processes that involve $|f^+\rangle$ if the correct frequency is pumped.

We can parametrically push the qubit towards $|f\rangle$ by simultaneously applying $\Sigma_{s,ge}$ and

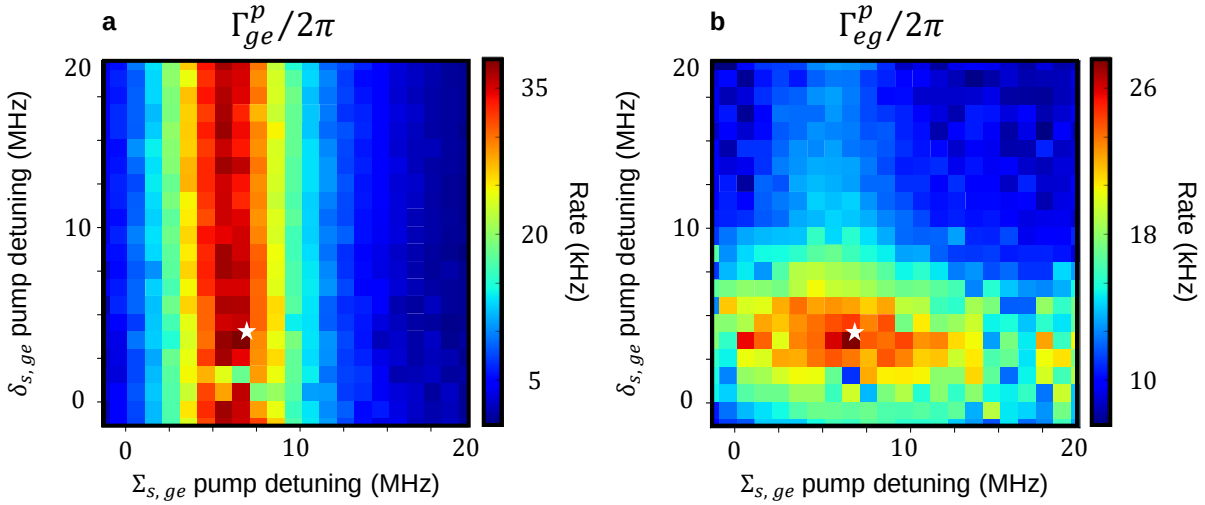


Figure 45: **Simultaneous heating and cooling** Similarly to single parametric processes, applying multiple allows for tuning of pump parameters. The $\Sigma_{s,ge}$ frequency detuning from 12.5275 GHz is swept on the horizontal axis, and $\delta_{s,ge}$ frequency detuning from 3.490 GHz on the vertical axis. Color represents the rate in kHz for the indicated transition and the white star the combination of pump frequencies that maximizes that transition rate. (a) Rate to transition from $|g\rangle \rightarrow |e\rangle$. (b) Rate to transition from $|e\rangle \rightarrow |g\rangle$.

$\Sigma_{s,ef}$, see Fig. 46. This method allows us to maintain an $|f\rangle$ state population and fight the two decay processes that would naturally occur ($|f\rangle \rightarrow |e\rangle$ and $|e\rangle \rightarrow |g\rangle$) by adding to the natural rates, rather than replacing them. When we apply these two energy-gaining parametric pumps, we are increasing the up-going rates to be greater than the naturally-occurring, uncontrolled down-going ones. Figure 46(c) is the most successful of the three experiments at maintaining the second excited state because $\Sigma_{s,ge}$ works to keep the qubit in $|e\rangle$ and reduce $T_1$ effects, and $\Sigma_{s,ef}$ pushes the qubit toward $|f\rangle$.

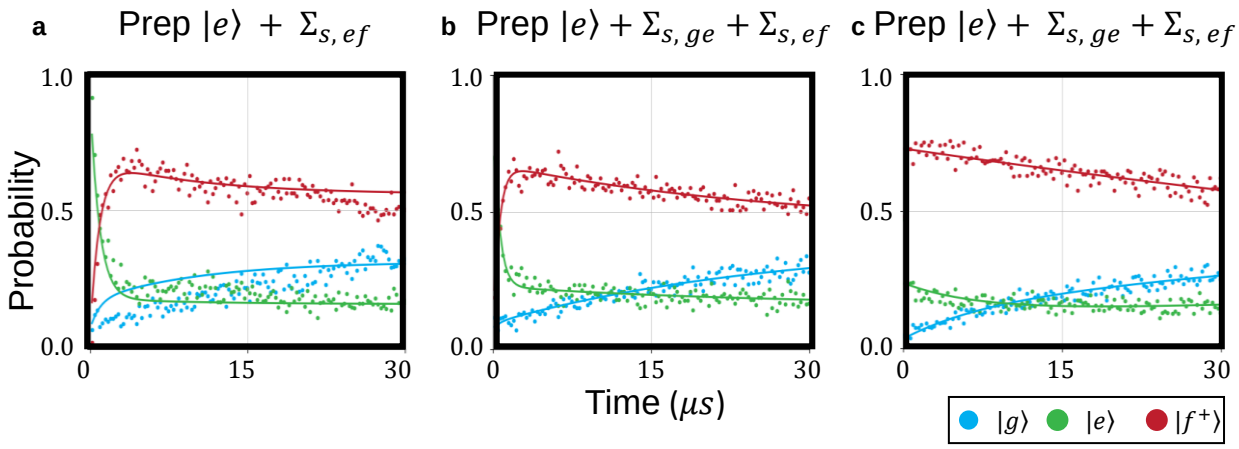


Figure 46: **Maintaining $|f\rangle$ population with parametric drives** The qubit is prepared in $|e\rangle$ and one or more parametric process can be applied to push the qubit towards $|f\rangle$. (a) Apply only $\Sigma_{s,ef}$. (b) Apply $\Sigma_{s,ge} + \Sigma_{s,ef}$ (c) Apply $\Sigma_{s,ge} + \Sigma_{s,ef}$. (b) and (c) have different pump amplitudes driven to change the relative population probabilities.

### 4.4 Bath Engineering Conclusions and Outlook

So far we have discussed situations with a definable chemical potential (Eq. 61), meaning that the transmon has population distributions commensurate with an atomic system. The chemical potential sets the level of population occupations, and levels up until that point are filled, like particles in a Fermi sea. The sign of the temperature also determines the level filling- the ground state can be empty and higher energy levels filled if the temperature negatively approaches zero, like shown in Fig. 46. It is worth noting the previously shown configurations could be nearly achieved by waiting long enough, or physically heating or cooling the qubit although this there is no guarantee of random success. The power of this parametric coupling scheme, though, shows us how we can avoid these uncontrolled processes and instead make rates and states that we want, when we want them. Additionally, our system also allows us to move outside of the chemical potential model into configurations that are not normally accessible with natural decays. This includes processes that could not

be duplicated by simply waiting long enough, as its decays are completely outside of the natural decay model.

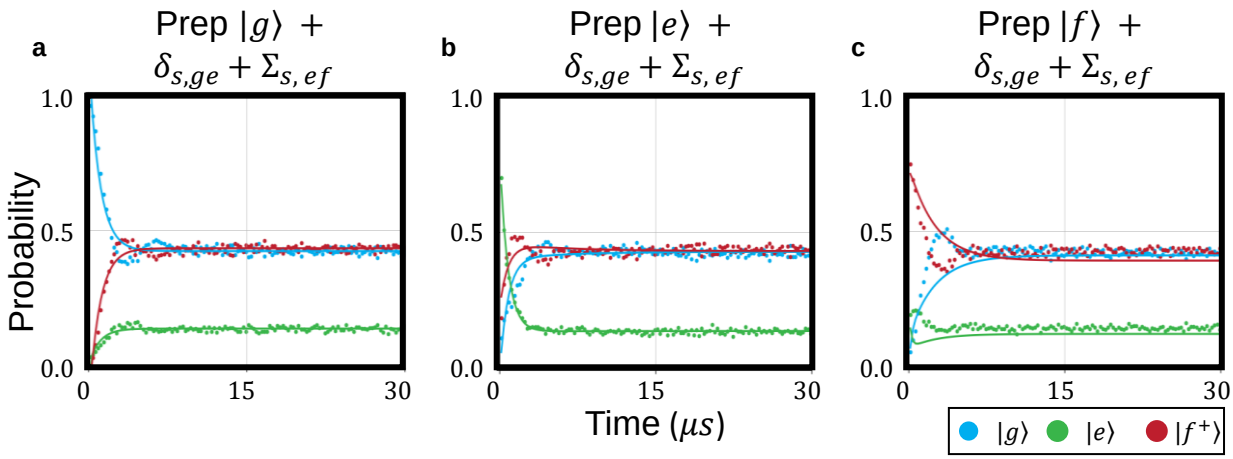


Figure 47: **Balanced $\Gamma^p_{eg}$ and $\Gamma^p_{ef}$** We demonstrate a qubit equally likely to relax to $|g\rangle$ as it is to $|f^+\rangle$, a thermalization outside of the chemical potential model we can define. In each panel, the qubit is prepared in the listed state (a) $|g\rangle$, (b) $|e\rangle$,and (c) $|f^+\rangle$ then both $\delta_{s,ge}$ and $\Sigma_{s,ef}$ are applied to push qubit relaxations away from $|e\rangle$. State balance is achieved nearly equally well for all three qubit preparations, supporting our claim of total control over the qubit's steady state dynamics.

Here we demonstrate one such example: a qubit that relaxes equally to $|g\rangle$ and $|f\rangle$, while skipping $|e\rangle$, see Fig. 47. This is achieved by matching the rates of qubit relaxation away from $|e\rangle$ by simultaneously pumping the $\delta_{s,ge}$ and $\Sigma_{s,ef}$ processes. This converts photons in $|e\rangle$ to $|g\rangle$ at rate $g_{\delta_{s,ge}}$ in $H_{\delta_{s,ge}}$ and energy is gained from $|e\rangle$ to $|f\rangle$ at rate $g_{\Sigma_{s,ef}}$ with $H_{\Sigma_{s,ef}}$.

This relaxation process is unlike any others we have previously shown because the middle level is emptied, breaking the assumed rules of a system with non-zero chemical potential. There is not usually a 'skipped' level. However with the properly tuned parametric drives, this was achieved without terrible trouble, showing that this system has useful applications outside of the chemical potential model. If any state, or collection of states, can be maintained in the qubit through continual parametric pumping, this opens up possible use cases of such a scheme.

The topics explored in this project extend beyond the data shown in this thesis. The goal of this project was to modulate couplings between qubits and their bath, but we also gained knowledge that has permeated throughout our research group as well as our peers. The SNAIL has become our parametric coupler of choice, and this project highlighted its flexibility even beyond bath engineering. In our lab alone, SNAILS are coupled to qubits in a modular quantum computer, to cavities in a modular quantum router with all-to-all coupling [96], as well as the core of quantum limited amplifiers [97].

The work explored in this project opened many doors for new research. Not only did we create an effective photonic chemical potential, but we were also able to stabilize stranger relaxation states of the transmon. Bath engineered qubits are vital to quantum simulations. If we are to simulate large, complicated quantum systems [6, 98], we must first be able to control and understand the system we have in the laboratory [55]. The work shown here is a demonstration of full control over qubit states and relaxation rates to create, ad hoc, any scenario a quantum simulator could need.

As part of my PhD, I explored many avenues with this platform. We use the knowledge gained to build a micro-maser [2] described in Chap. 5, as well as two interesting spin-off projects initially developed using this architecture. First I will discuss sub-harmonic transmon gates and conclude with transverse transmon measurement. Both experiments have since become fully independent research projects.

### 4.4.1 Sub-Harmonic Driving

Until now in this project, the SNAIL was the only circuit element driven with parametric drives, meaning the SNAIL is pumped with an off resonant tone that is some combination of the mode frequencies we wish to mix, in our case the SNAIL and qubit. When the qubit has been prepared in some state beyond $|g\rangle$, like in transmon cooling (Sec. 4.3.3), it has been driven with resonant tones to excite the mode directly. However, we do not necessarily need a nonlinear mixing element to parametrically mix modes, an example demonstrated with cavities in Ref. [99].

In this project, when the SNAIL is used for parametric mixing, one of the $s$ operators

effectively becomes a stiff, classical variable when pumped far-off resonance. The remaining operators dynamically evolve under influence of this pump (this is how we get an effective two-body interaction out of a three-wave term). This exact same style of thinking can be applied to a fourth order qubit mode directly.

The transmon's leading fourth order nonlinear term

$$H_{transmon,NL} = \frac{\alpha_q}{12}(q + q^\dagger)^4 \tag{79}$$

is typically approximated to only include the anharmonic term $\frac{\alpha_q}{2} q^\dagger q^\dagger q q$. However, if we look beyond the rotating wave approximation (which is more accurate anyway), we retain all other combinations of $q$ and $q^\dagger$ operators. These Hamiltonian terms can be activated by driving, in a similar way to how we have previously treated parametric coupling operations. One such term is:

$$H_{transmon,SH} = \frac{\alpha_q}{3}(q^\dagger q^\dagger q^\dagger q + q q q q^\dagger) \tag{80}$$

which can be activated by pumping at $f_d = \frac{f_{q,ge}}{3}$.

Qubits experience decay through their coupled channels, and the qubit's drive line must be configured to pass its resonant frequency. This gives the qubit a direct channel to decay through so we try to couple the pin as weakly as possible. But if we can drive the qubit off resonance, we can send drives down that line that shield the qubit from resonant decay and decrease the drive strength needed.

This sub-harmonic driving scheme has these advantages. First, it affords us a speed up in Rabi rate $g_{SH} = \frac{\alpha_q}{3}\eta^3$, compared to the resonant drive's $\eta$. Faster gates means higher fidelity in the face of low coherence times. Second, the qubit is driven at a different frequency to its loss, so input lines can be configured with less attenuation and decrease the heat load on our dilution refrigerator, as well as frequency filtered to reduce qubit loss through the input line.

Our sample shown here was the perfect candidate to test this driving scheme on. The first step was to see if integer fractions of driving frequencies could induce the qubit excitations we usually see resonantly ($|e\rangle \leftrightarrow |g\rangle$, $|f\rangle \leftrightarrow |e\rangle$, and $|f\rangle \leftrightarrow |e\rangle \leftrightarrow |g\rangle$). We tested this with

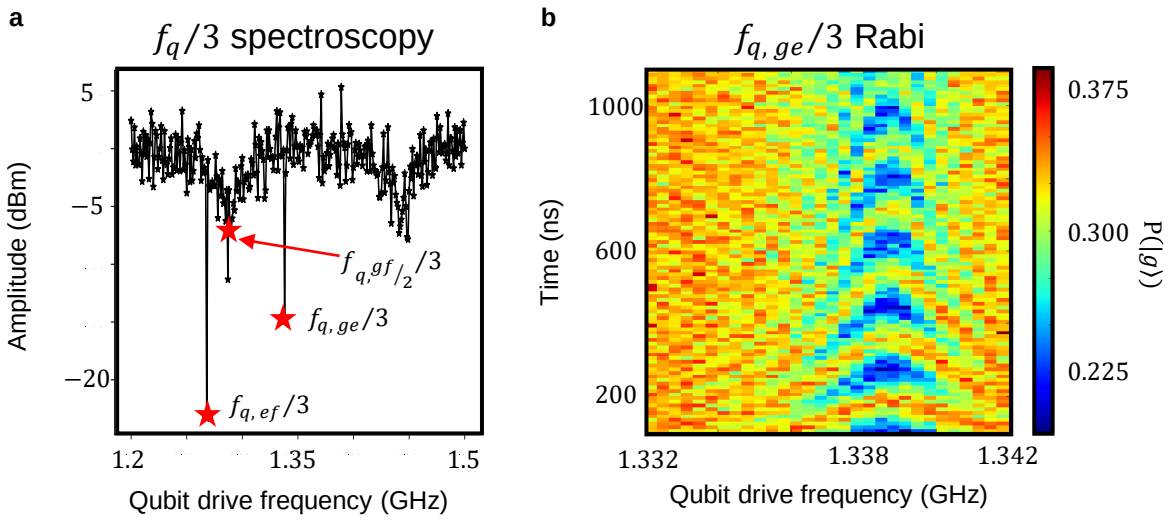


Figure 48: **Sub-harmonic qubit spectroscopy and Rabi gates** (a) The qubit's $f_{ge}$, $f_{gf/2}$ and $f_{ef}$ transitions were found at one third value compared to resonant driving. Note that the difference between $f_{ge}/3$ and $f_{ef}/3$, normally indicating $\alpha_q$, scales by 1/3 as well. (b) At $f_{q,ge}/3$, the qubit oscillates between the ground and excited state as indicated by the colored 'chevron' pattern.

frequency-domain CW spectroscopy, at $f_{CW}/3$. Figure 48(a) shows that indeed the qubit has its expected spectroscopy response, but this time when the generator was set to frequencies near one third the resonant frequency.

Next we moved to the time domain to measure the rate of Rabi oscillations between $|g\rangle$ and $|e\rangle$. In Figure 48(b), we sweep both the sub-harmonic drive frequency and time. This 'chevron'-type pattern indicates that the qubit is flopping between $|g\rangle$ and $|e\rangle$ at gate speed determined by the spacing between horizontal lines.

This result is exciting because our qubit was driven by a far-off resonant tone but yet responded at a rate faster than traditional resonant spectroscopy. After this result, we moved onto the experiment discussed in the next section. My colleague Mingkang Xia carried out this sub-harmonic experiment on a sample initially intended to be a modular qubit coupler, so with a different form factor and intended use but still (even more) successful at these sub-

harmonic gates. Our paper Ref. [93] goes into greater detail on the results of this experiment. One final note: there is nothing special or unique about either the transmon qubit design measured here or in [93]. This driving scheme would work well on just about any transmon designed for any application.

### 4.4.2 Rate Balancing and Qubit Measurement

The same sample was used to understand how the light emitted by the SNAIL can measure the qubit. Throughout this experiment, we have made thermal states with one or more parametric process. Those processes create photons in the SNAIL that are spread throughout its broad bandwidth ($\approx 12$ MHz), making them distinguishable from one another. When we control the rates in both directions to and from adjacent levels in the qubit's manifold, we can create SNAIL photons that are indistinguishable if we balance the rates. For example, we balance $\Gamma^p_{ge}$ and $\Gamma^p_{eg}$ in Fig. 44, making the SNAIL output for both individual processes the same. This leads to a special feature that we had previously not measured.

If the rates are truly balanced, and the photons produced are indistinguishable, then for states entirely along the equator with Bloch vector $\sqrt{\frac{1}{2}}\left|g\right\rangle + \sqrt{\frac{1}{2}}e^{i\phi_d}\left|e\right\rangle$, we should see a manifold of states that are 'dark' to the parametrically induced decay. This means that what we will see when measuring coherence in the $X-Y$ plane is just the raw decoherence time of the system for 'dark' states and much faster, parametrically enhanced dephasing for all others. Note that the maintained balanced rates will never give a $Z$ component decay.

We can scan through combinations of heating and cooling pumps, like in Fig. 45, to find the conditions necessary to make qubit decays dark to dephasing due to $\left|g\right\rangle \rightarrow \left|e\right\rangle$ and $\left|e\right\rangle \rightarrow \left|g\right\rangle$ mixing. The pumps carry a phase, which set the angle $\phi_d$ as the equatorial phase difference. This requires the maintenance of phase stability amongst the drives. We must be able to lock this phase for the duration of the experiment. Initial testing showed interesting results. For each detuning of the parametric drives, we swept the phase. We expect to see the same amplitudes separated by integers of $\pi$. In Fig. 49, we do not see this periodicity. This indicates phase drifting.

If the phase difference is drifting with time, then the definition of an absolute $\pi$ rotation

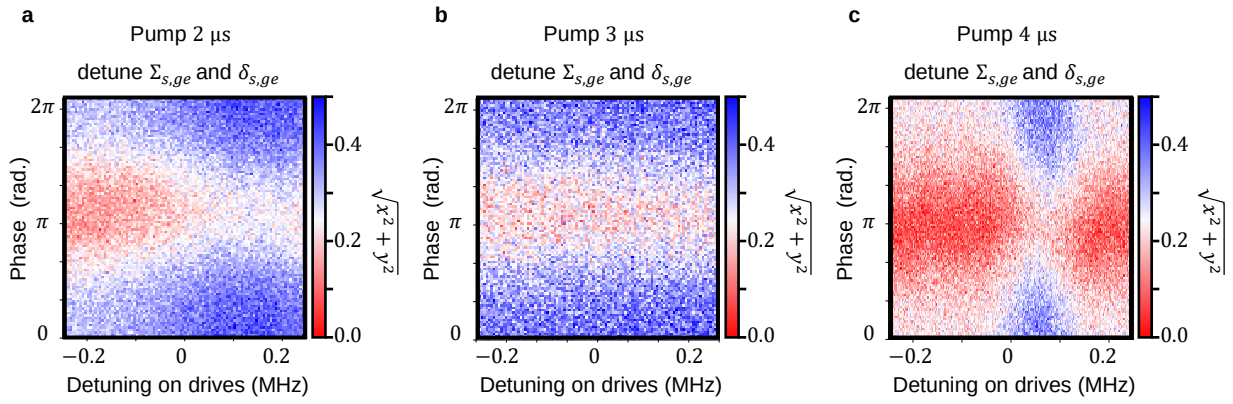


Figure 49: **Qubit measurement dark states** In each of the three panels, we detune both parametric drives and sweep the relative phase between the $\Sigma_{s,ge}$ pulse and $\delta_{s,ge}$. There should be a point where the vector distance $\sqrt{x^2+y^2}$ is maximized. (a) Apply pulses for 2 $\mu$s, (b) Apply pulses for 3 $\mu$s, (c) Apply pulses for 4 $\mu$s. All three scenarios should yield similar results: matched detunings with relative phase. However results were unstable. There appeared no combination of drives that could always produce the same results.

is not the same for each bin in the colorplot, and it does not seem to drift back into place, hence measuring for longer in panels (b) and (c) of Fig. 49. This means we cannot reliably find the pump conditions needed to make coherent dark states. This result led us to put this project aside because it required greater phase stability than we could maintain with the room temperature electronics at hand. The phase drifts present were slow enough to sometimes show an interesting measurement and sometimes show odd results such as three apparent dark states, but not fast enough to always fail.

My colleagues Chao Zhou and Girish Kumbhar carried out this project on yet another sample intended for modular quantum computing with similar SNAIL-qubit couplings. This time they fixed the phase drifting issue in their room temperature electronics, achieved by moving away from the mixer-based AWG interferometer we had been previously using. Instead they generated pulses and read out with a mixer-less platform, the QICK RFSoC. This firmware developed by quantum researchers generates all pulses on the same board so

they are locked to the same clock and therefore to one another. See [100] for greater detail on the QICK.

Additionally, they have performed novel transmon readout using this method. The SNAIL produces light with two protected coherent eigenstates are displaced from the origin in the direction determined by the qubit state, with the amplitude of displacement controlled by the parametric driving strength. The light produced by the SNAIL, which we have previously 'thrown away' or not measured, can be used to encode the qubit's information. Professor Roger Mong highlighted this feature to us, showing that we could use the SNAIL for QND longitudinal readout of the transmon. The results of qubit longitudinal measurements are found in Refs. [38, 101].

## 5.0 Single-Atom Micro-Masing: Experiment

The theoretical ABOCCs in Ref. [2] by our collaborators Chenxu Liu and Professor David Pekker were designed to fit into existing circuit architectures in our laboratory. With the knowledge gained from the bath engineered qubits project, Chaps. 3.1 and 4, we were primed to take on the challenge of building a circuit like the one shown in Fig. 21. Before an ABOCC could be built and measured, however, we needed to first answer the question: can we build a linearly coupled maser that meets the Schawlow-Townes limit on laser linewidth? This research project is still underway, but the majority has been completed and will be described in depth in this chapter. I will conclude with an outlook for the project having gained perspective on the problems at hand.

### 5.1 Maser Simulation

The linear micro-maser, shown as the top option in Fig. 21, fulfills the list of needs in List 3.2.1 with realizable values for mode parameters, seen in Fig. 22. To verify the circuits basic behavior, I started with numerical simulations of a Hamiltonian governed by these mode couplings using QuTiP.

Calculations were based on taking the rotating wave approximation, assuming the SNAIL is operating at a purely third order, zero fourth order, bias condition. Additionally, the qubit and SNAIL were both approximated as two level systems, and $\Delta_{qc} = 0$, the qubit exactly on resonance with the cavity. The goal of this was to get a sense of what coupling strengths and decay rates would lead to an output that resembles our masing ladder in Fig. 23, where the qubit is (on average) in $|e\rangle$, the SNAIL is cold and thus in $|0\rangle$, and the photon occupation in the cavity increases to some upper limit. The values listed in the 'Target value' column of Table 2 reflect some of the ideal parameters found in QuTiP with the Hamiltonian:

$$H_{QuTiP} = g_{\Sigma}(\sigma_s^+\sigma_q^+ + \sigma_s^-\sigma_q^-) + g_{qc}(\sigma_q^+ c + \sigma_q^- c^\dagger) \tag{81}$$

for parametric coupling rate $g_\Sigma$ and qubit-cavity direct exchange rate $g_{qc}$. The steady state results are shown in Fig. 24.

Such a simulation is a good starting point, but unfortunately misses the interesting dynamics of the masing process. My results show the steady state solutions to the master equation, in a truncated Hilbert space. The Hilbert space of each operator, or size of each's contribution to the overall rediagonalized solution matrix, greatly impacts the speed of each simulation. In an effort to save computing resources, the cavity mode operator was reduced to 30 in size. This artificially sets the maximum photon occupation in the cavity. Additionally, removing qubit loss (not assigning it a loss operator $\sqrt{\kappa_q}q$) is not painting the full picture- the process of adding photons to the cavity via the transmon is a function of its lifetime. This determines how effective the parametric drive can be at inverting the qubit's population. Nonetheless, this preliminary proof-of-concept test was my starting point before microwave simulations, to understand the coupling strengths and loss parameters needed to drive the photon ratchet process.

An LC oscillator will act as the cavity, and a transmon coupled to a SNAIL as our atom or gain medium. Such a circuit can be realized in the form factor of the work described in Chap. 4- in fact that sample was initially designed and intended to be this maser project. However, I did redesign the experiment with some gained knowledge and fabrication techniques.

With these ideal values of Table 3 in mind, microwave simulations were performed in Ansys' HFSS and Maxwell, shown in Fig. 50. Instead of using a 3-dimensional coaxial, $\lambda/4$ cavity mode, the masing cavity was designed as a $\lambda/2$ stripline resonator. This form more closely resembles what our qubits and SNAILs look like. This choice was for a number of reasons. First, it greatly reduces the footprint of the housing because the physical size of the cavity is significantly smaller (from three dimensional centimeters to nearly two dimensional millimeters). Second, it allows greater flexibility. Changes can be made much faster and more frequently by redoing only the nanofabrication steps, rather than having the entire housing re-machined. The aluminum housing was simulated as a block with circular holes extruded through. One tube [103], which spans the entire block, holds the SNAIL, qubit, and additional readout resonator (more details are given below). This is intersected by a

Table 3: **Goal, simulated, and measured values for the maser** The target values were determined by our intended Hamiltonian design and QuTiP evaluations of Hamiltonian dynamics. The simulated values were found either directly in HFSS using an Eigenmode solver, or HFSS data was exported and calculated with the pyEPR analysis method [102]. Measured values are typical across multiple measurements, at the bias conditions that yielded these results.

| **Parameter** | **Target value** | **Simulated value** | **Measured value** |
|---|---|---|---|
| $f_s$ | 5.0 GHz | 5.245 GHz | 5.76 GHz |
| $f_q$ | 7.0 GHz | 7.086 GHz | 6.922 GHz |
| $f_c$ | 7.0 GHz | 6.987 GHz | 6.97201 GHz |
| $f_r$ | 8.0 GHz | 8.292 GHz | 8.547 GHz |
| $\frac{\kappa_s}{2\pi}$ | $10 - 20$ MHz | 21.457 MHz | 24.56 MHz |
| $T_{1,q}$ | $\infty$ | 25.226 $\mu$s | 2.438 $\mu$s |
| $\frac{\kappa_c}{2\pi}$ | 1.4 kHz | 0.033 kHz | 19.67 kHz |
| $\frac{g_3}{2\pi}$ | $-100$ MHz | $-134$ MHz | – |
| $\frac{g_4}{2\pi}$ | 0 | 0 | $< 0$ |
| $\frac{\alpha_q}{2\pi}$ | $-180$ MHz | $-176.225$ MHz | $-163.6$ MHz |
| $\frac{g_{qc}}{2\pi}$ | 1.0 MHz | 1.569 MHz | 0.44 MHz |
| $\frac{g_{qr}}{\Delta_{qr}}$ | 0.1 | 0.0745 | 0.071 |

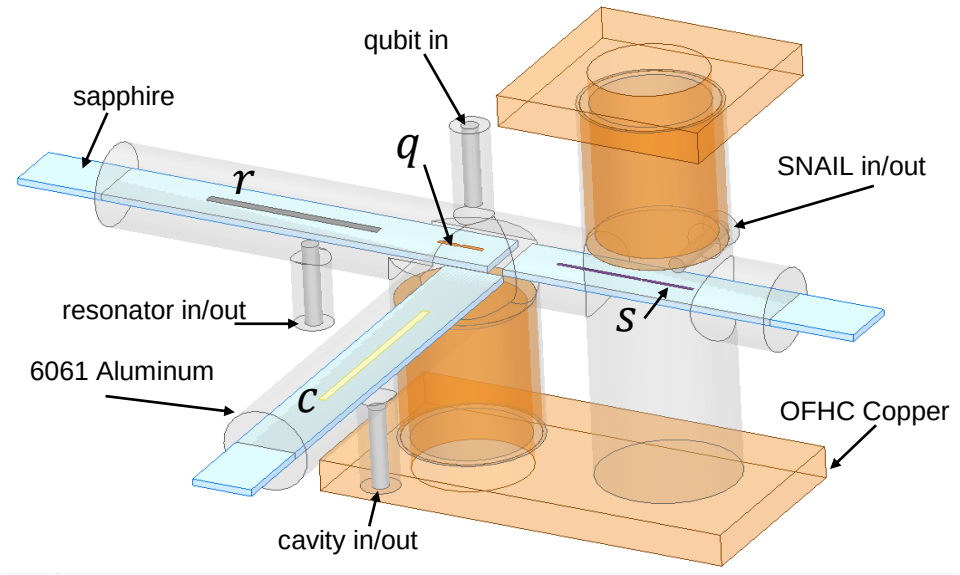


Figure 50: **Microwave simulation design** The experiment as designed in Ansys HFSS and Maxwell, with the goal values initially found in QuTiP as a guide, see Table 3. There is one 50 Ω machined pin for each circuit element connected to the input/output chain of the dilution refrigerator. The SNAIL pin is inserted far into the extruded aluminum tube for high $\kappa_s$, while the qubit and cavity's are retracted for high $Q_{q,total}$ and $Q_{c,total}$. The magnets are designed to have low cross-talk.

second tube that holds the masing cavity.

The maser cavity mode was designed to be high Q, so its RF coupling pin was receded into the housing. In this experiment, all pins are professionally fabricated to be 0.2 in (see below, Sec. 5.2), so the entire pin casing was retracted into the 'Perfect Conductor' block. To reduce its coupling with the qubit, and in turn the SNAIL, the masing cavity $c$ was simulated on a separate sapphire chip and in its own perpendicular tube. This reduces the dipole-dipole coupling between modes.

The qubit's inductance, dominated by the Josephson junction element, was set in HFSS to put the qubit on resonance with the cavity. In experiment, the transmon will be realized in a SQUID, see Sec. 2.1.2. The SNAIL's inductance was chosen to operate near 5.0 GHz. The

SNAIL-qubit coupling was achieved by making the SNAIL's large capacitor pads asymmetric, see Fig. 51. The qubit must be high Q, the $\frac{g_{sq}}{\Delta_{sq}}$ hybridization factor around 0.01, and the SNAIL must also have a low Q-factor. I found it difficult to meet all three requirements simultaneously. However by making the SNAIL pad closer to the qubit longer than the one closer to the SNAIL's coupling pin, I was able to not poison the qubit's lifetime by weakly hybridizing it with a low Q coupler. The SNAIL's loop and concentration of energy is near its strongly coupled pin, but its fields do extend towards the qubit.

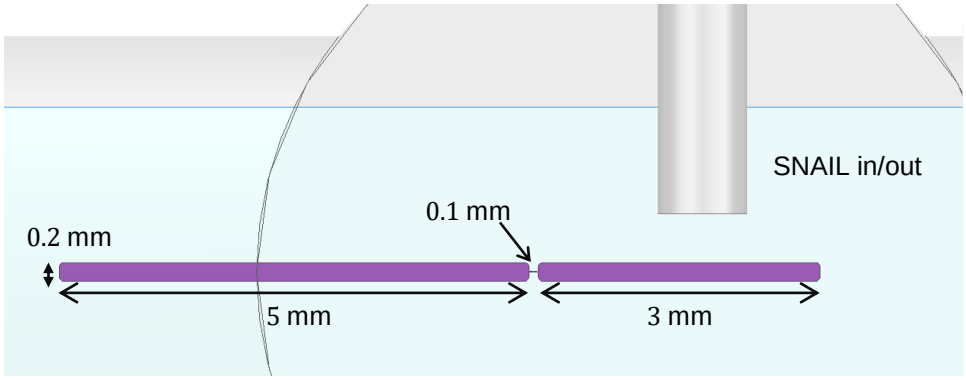


Figure 51: **Asymmetric SNAIL design** The SNAIL as designed in HFSS. The pads contribute to the mode's linear capacitance and inductance. To keep qubit lifetimes high and SNAIL lifetimes low, the SNAIL's JJ loop, where its fields are concentrated, must be far from the qubit but close to the SNAIL's dedicated RF pin. The pads were made asymmetric so SNAIL fields can extend to the qubit while maintaining its frequency and nonlinearity, and keep the linear inductance at a minimum.

Although the masing protocol (Table 1) does not require direct qubit or cavity pulses, I still want to be able to probe the qubit for diagnostics. This requires both (a) the qubit to have its own, weakly coupled drive pin and (b) a resonator with which to perform qubit readout. The high Q masing cavity $c$ would not suffice, as it being long lived makes it difficult to read quickly, and is optimized to have minimal to zero $\frac{g_{qc}}{\Delta_{qc}}$, meaning we cannot perform QND dispersive measurements [8]. This led me to add an additional stripline resonator to the circuit, labelled $r$ in Fig. 50, but placed its frequency far enough away that it would not interfere with the parametric masing process. The readout resonator was intended to have

a loss rate of $\frac{\kappa_r}{2\pi} = 1$ MHz and $\frac{\chi_{qr}}{2\pi} = 1$ MHz.

The resonators' coupling pins were placed with the design idea of WISPE [52] in mind. This means the positioning of the resonator's pin (and all other pins except the qubit's, too) is in a place of zero qubit field. This is determined by running the eigenmode solver for the qubit (or whatever circuit element one wishes to preserve the lifetime of) and plotting the electric field of that mode, see Fig. 52. There are multiple spatial positions where the qubit's field is nearly zero- these are the ideal positions for a coupled cavity's pin, minimizing the qubit's losses due to coupling to a lossy transmission line. This is in stark contrast to our previous understanding, where we assumed the best cavity port position was as far from the qubit as possible. The end of the masing cavity and readout resonator actually sit at nodes of qubit E-field, seen on the inset of Fig. 52! WISPE is a frequency dependent effect, and therefore the positioning of the ports were chosen for the qubit on resonance with the masing cavity.

Both the SNAIL and SQUID qubit must be flux tunable. In three-/quasi-two- dimensional architectures, we typically flux bias using coil magnets that are off chip and controlled with a current sent from room temperature. For a single superconducting loop, this is relatively simple to implement as the Josephson junctions are biased by the single externally controlled magnetic field, on top of any local (nearly spatially constant) magnetic field. However, for this experiment I wish to separately control the flux biases in both the SNAIL and SQUID which are only approximately 10 mm apart. Early Maxwell simulations showed equal flux coupling for both loops of Josephson junctions, as current sent through the SNAIL's dedicated magnet had an equal effect on the qubit's loop and vice versa, seen in Fig. 53(a).

To mitigate this unwanted flux cross-talk, I opened up a tube beneath one magnet in order to provide the magnetic flux an alternate path, seen in Fig. 53(b). This made the flux coupling in the qubit's JJ loop to the qubit's magnet two orders of magnitude greater than to the SNAIL's magnet. This opening was created under the SNAIL's magnet and the face was covered with copper on the opposite side of the aluminum block to concentrate magnetic field in a normal metal rather than in a block of superconductor. I chose the to open up under the SNAIL, rather than the qubit, in an effort to preserve qubit lifetimes by making a more uniform local environment.

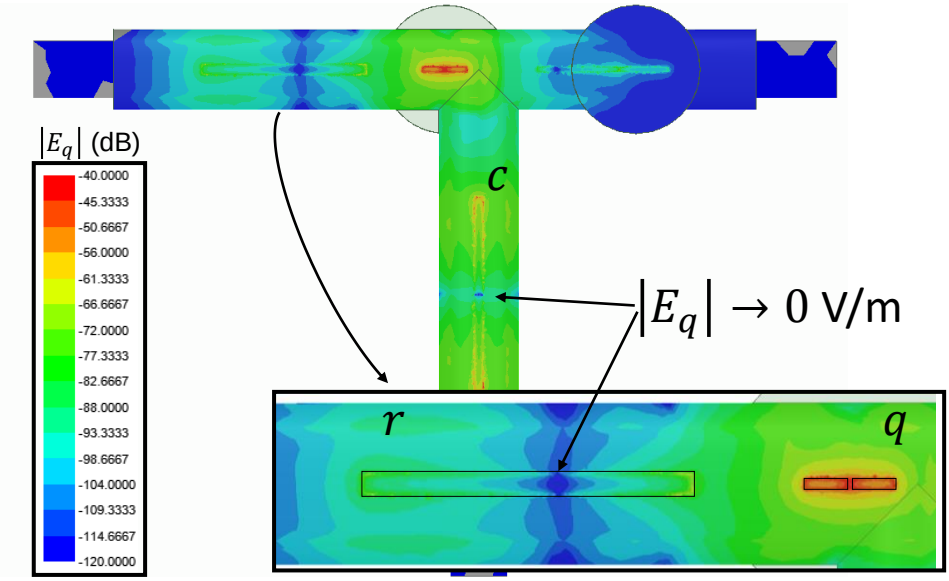


Figure 52: **Qubit WISPE** The magnitude of the qubit's electric field. The eigenmode with strongest fields in the qubit is plotted throughout the entire tube housing for the frequency bias where $\Delta_{qc}$ is nearly zero. The most ideal location to place the pin for the two resonators and SNAIL is where the qubit's field is lowest. For both $r$ and $c$, we can see the darkest blue/lowest $\left|\vec{E}_q\right|$ near the middle of the striplines, indicating that these are the best locations to place the respective coupling pins. This is a starting point for maximizing $Q_{q,total}$ before the pin's distance from the $i^{\text{th}}$ element is adjusted for the necessary $Q_{i,ext}$.

## 5.2 Maser Fabrication and Machining

Figure 54 shows the superconducting aluminum housing machined from 6061 aluminum and mirror polished using a diamond flycutter by our excellent research machinist William Strang. This experiment does not have any indium seals. We came to learn that the inherent quality of mating surfaces is better at removing unwanted loss than using soft indium to span gaps, hence the mirror finish. Sapphire chips span each extruded tube. Aluminum chip holders clamp one end of each piece of sapphire and a molybdenum pusher screw secures the chip in position. These chip holders are aligned with titanium dowel pins to ensure the chip

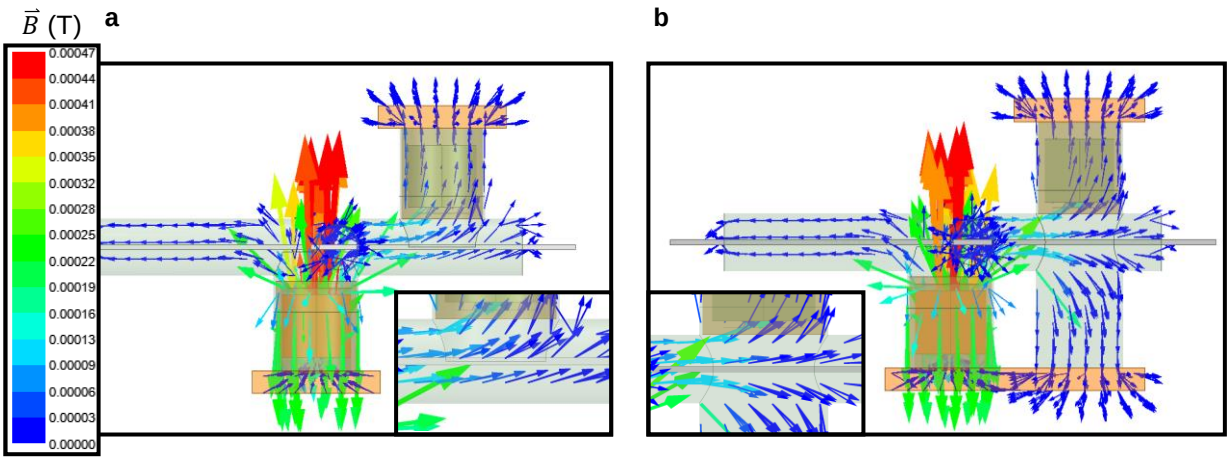


Figure 53: **Asymmetric magnet design** The magnetic field in the volume of the intersecting tubes, with $I_q = 10\ mA, I_s = 0\ mA$. (a) The field lines emanate from the qubit magnet on the left, but would be equal magnitude and opposite sign if from the right SNAIL magnet. This is not ideal. In the inset image, the field lines that pass through where the SNAIL is located have a perpendicular component to the SNAIL, causing non-negligible cross-coupling. (b) When a tube is opened up to copper below asymmetrically, the field lines are now parallel to the SNAIL's plane, meaning they will have minimal cross-talk between the qubit's magnet and the SNAIL itself.

is straight in its tube.

Another key difference with this housing, compared to that shown in Fig. 26, are the microwave coupling pins. The pins used in this experiment are 2.92 mm waveguide probes manufactured by Southwest Microwave, see Fig. 55. The BeCu pin is rigid and a fixed 0.2 in. What a difference this makes compared to homemade: while we lose the flexibility of length, we fortunately lose bending flexibility! The coupling of each pin to its respective circuit element was set by how far into the Al housing the SMA threads were cut in.

The magnets are CuNi clad superconducting NbTi wire, both spun around spindle-shaped OFHC copper pieces, shown in Fig. 56. At room temperature, their resistances are measured $\sim 40\ \Omega$. The most common failure mode of this magnet was shorting the leads to the rest of

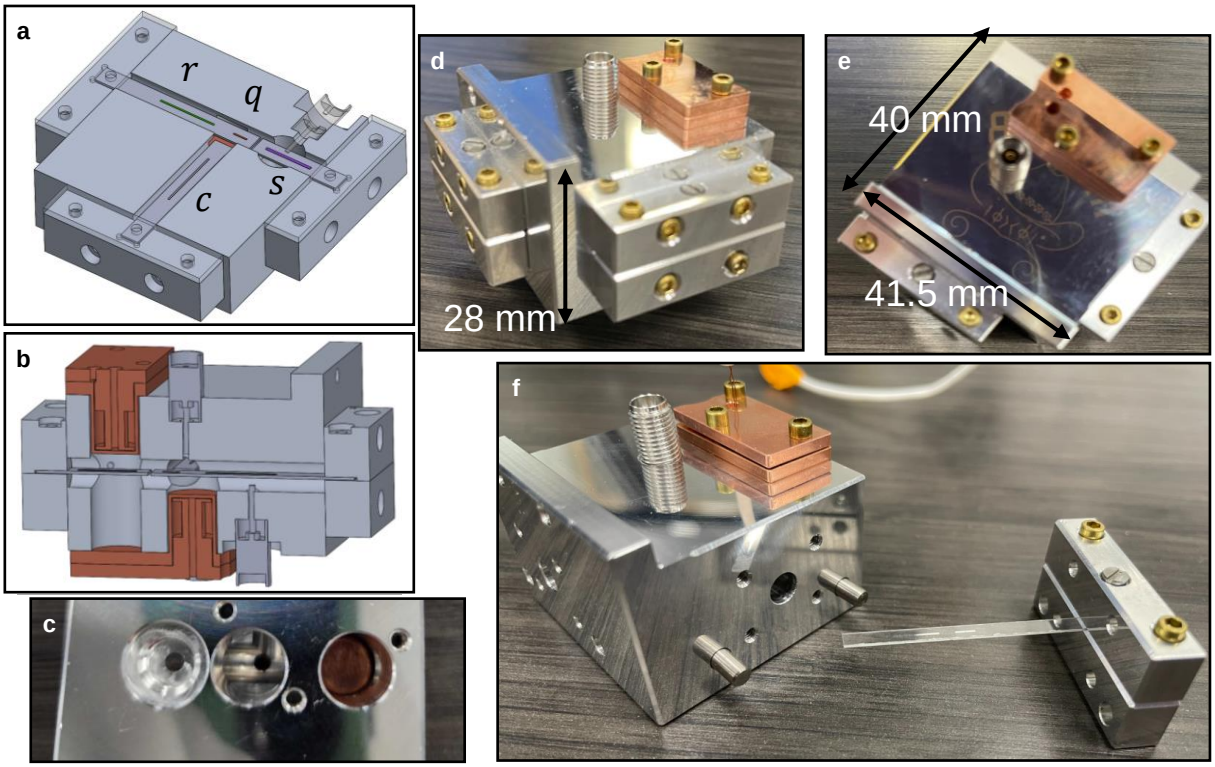


Figure 54: **Maser device photos** (a, b) 3D AUTO CAD drawings of the device, based on the microwave simulation model of Fig. 50. (c) The tube where the SNAIL, qubit, and readout resonator are slotted, as seen without the magnet with copper opening and a microwave drive pin. (d, e) The fully assembled housing, mirror polished and bolted with brass screws. (f) The chip holder fits directly onto the larger aluminum block housing, aligned with Titanium dowel pins. The sapphire chips are inserted into the extruded tubes.

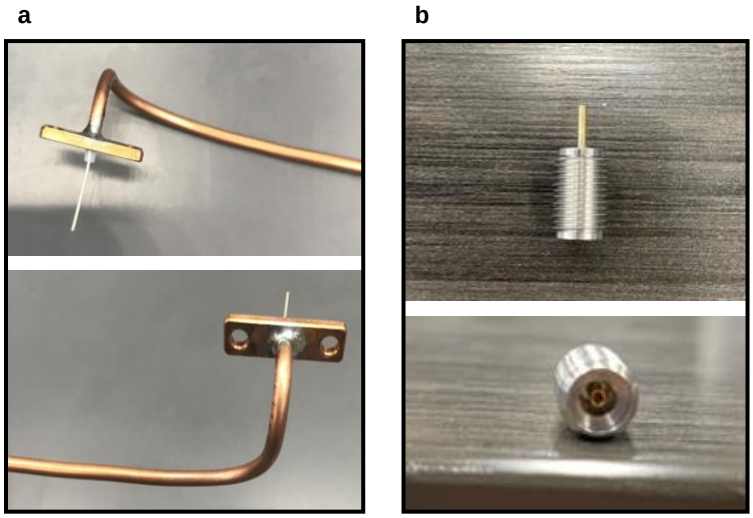


Figure 55: **Homemade vs. manufactured pins** We use microwave coupling pins to send and receive signal from our delicate quantum experiments. (a) The pins used in Chap. 4 were made by stripping away the outer jacket and insulating dielectric on a copper coaxial wire, soldered through a copper face that joins the rest of the housing. These pins allow ad hoc pin length changes, but bend under cryogenic contraction. (b) The pins used in the maser project are SMA waveguide probes manufactured to be precisely 0.2 in of BeCu, and are torqued into the aluminum housing.

the housing. The magnet spindles sit inside a copper cup, which helps flux travel through the superconducting housing (which should, in theory, expel all magnetic field). When the spindle is placed inside its cup, this can cause the magnet wire leads to get crushed against the cup wall and create a current short. This causes trouble at cryogenic temperatures, as we send mA of current through the wire loop. If this is in direct contact with the normal metal wall or too large a current is applied, it generates unwanted heat and raises the base plate temperature. Shorting was prevented by decreasing the number of wire turns around the spindle, making the magnet smaller and better able to sit inside its cup. This reduces the flux per current imparted on the Josephson junction loops, which may cause trouble if the appropriate external flux needed cannot be reasonably attained with currents that do

Figure 56: **Magnet spindles** Superconducting NbTi wire is spin around a copper spindle and two leads are fed out the top, which are then twisted and soldered to pins that mount to the dilution refrigerator's DC drive lines. This magnet has long leads that breakout at the 4 K stage of the fridge, in a single piece, so that greater magnitude current can be drawn without heating the base stage of the fridge.

not cause excessive heating. Longer leads on the spindles allow us to drive higher magnitude current because the 4 K plate of the fridge can tolerate a higher heat load compared to the 20 mK plate. The 4 K plate has a nominal 1.5 W cooling power through the pulse tube cooler, while the base stage has only $\approx 12$ $\mu$W rated for 20 mK. This means that magnets that breakout at the 4 K plate can be biased with nearly $\pm 100$ mA of current before heating, as opposed to those at base tolerating $\pm 20$ mA. The ability to bias at higher currents means we can always apply the bias needed to operate at our ideal $\Delta_{qc} = 0$.

The SQUID, SNAIL, masing cavity, and readout resonator are all optically defined and etched superconducting tantalum on a sapphire substrate. There is not a defined ground plane or inner/outer conductor. The geometry of the tantalum largely defines the capacitance and linear inductance of each element, and those with Josephson junctions, the SQUID and SNAIL, are dominated by the nonlinear inductance of their JJs.

The qubit must be on resonance with the cavity to utilize the always-on direct coupling between the two, in order to exchange each qubit photon into the cavity. In simulation we can set this condition, but this is much harder to perfectly hit in fabrication, necessitating

the frequency-tunable SQUID. It was fabricated such that the critical current of each of the two Josephson junctions were half that needed to make a single JJ with the same effective Josephson inductance. I needed the total inductance of the SQUID to be 4.8 nH. If I were fabricating a single JJ with 4.8 nH inductance, it would have a critical current of 0.0685 $\mu$A based on the Josephson relation:

$$L_J = \frac{\Phi_0}{2\pi I_c} \tag{82}$$

for flux quantum $\Phi_0$. However, to make a symmetric SQUID, I split this into two identical Josephson junctions which inversely add inductance in parallel. Therefore, each Josephson junction was designed for $L_J = 9.6$ nH and $I_c = 0.0343$ $\mu$A. This was chosen because this $L_J$, at $\Phi = 0$, sets the maximum frequency. SQUIDS and SNAILs can only be tuned down in frequency from their $\Phi_{total} = 0$ bias. This ensures that I could bias the SQUID to a $\Phi_{ext}$ that would make the qubit cross in frequency with the masing cavity. All Josephson junctions in this project are made of aluminum/aluminum oxide/aluminum and in the bridge-free 'Manhattan' style [104].

The SNAIL has two large JJs, instead of three, and has an inductive energy ratio of $\alpha_s = 0.3$. To operate at 5.0 GHz with $g_3 \neq 0, g_4 = 0$, the critical current for each large Josephson junction was fabricated at 0.159 $\mu$A and for the small 0.0476 $\mu$A.

It became difficult to meet all of the requirements that I had set for this experiment, as changing one physical parameter changes the entire mode structure of the experiment due to circuit re-hybridization. The effects of particular design choices can be tested by removing, one by one, each element to find its contribution to the mode landscape. Simulations showed that despite my efforts to put the readout resonator's pin at a desirable WISPE spot, this was still what limited $Q_{q,total}$. In an effort to increase qubit $T_1$, I added one to two 0.01 in thick molybdenum washers under the readout resonator's RF pin. Adding machined washers between the aluminum housing and bottom of the SMA threads precisely shortens the pin length reaching into the tube. Unfortunately, this is not seem to alter qubit lifetimes in any significant way, indicating that there are other sources of loss and noise causing low qubit lifetimes.

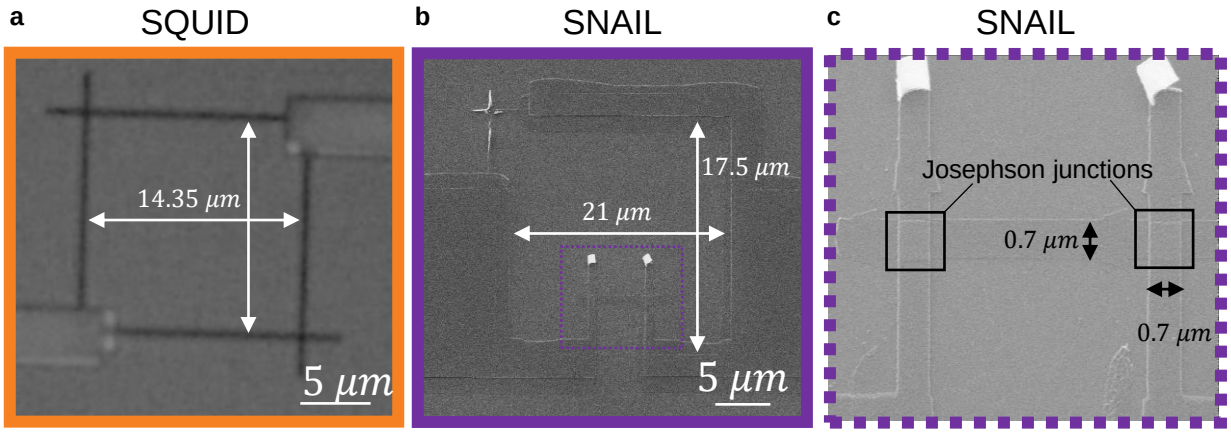


Figure 57: **SEM of qubit and SNAIL** SEM images taken of SQUIDs and SNAILs from the same round of fabrication as those used to collect data. (a) The SQUID features two identically small Josephson junctions. Flux is threaded through the space between them to change $f_q$. (b) The SNAIL features two identical large Josephson junctions in parallel with one smaller by ratio $\alpha_s$. Flux is threaded through the space between to change $f_s$ and $g_n^s$ nonlinearity of the $n^{\text{th}}$ order. (c) Zoomed in on the two large Josephson junctions of the SNAIL. Junctions are made in a bridge-free geometry.

### 5.3 Frequency Domain Measurements

All measurements are taken in reflection. The experiment was first measured using frequency domain spectroscopy, a task more complicated than in Sec. 4.2 because now there are two frequency tunable components. First, we measured the masing cavity on the VNA at $\Phi_{ext} = 0$, which is not necessarily true to $\Phi_{total} = 0$ due to uncontrolled flux trapping. Because the cavity is high Q with a narrow linewidth, even before the masing process is turned on, it requires careful searching in frequency space as its mode signature can be smaller than the frequency spacing on the VNA. Once the mode is identified, the cavity initially exhibits a high power response which gives us hope that the neighboring qubit is functioning.

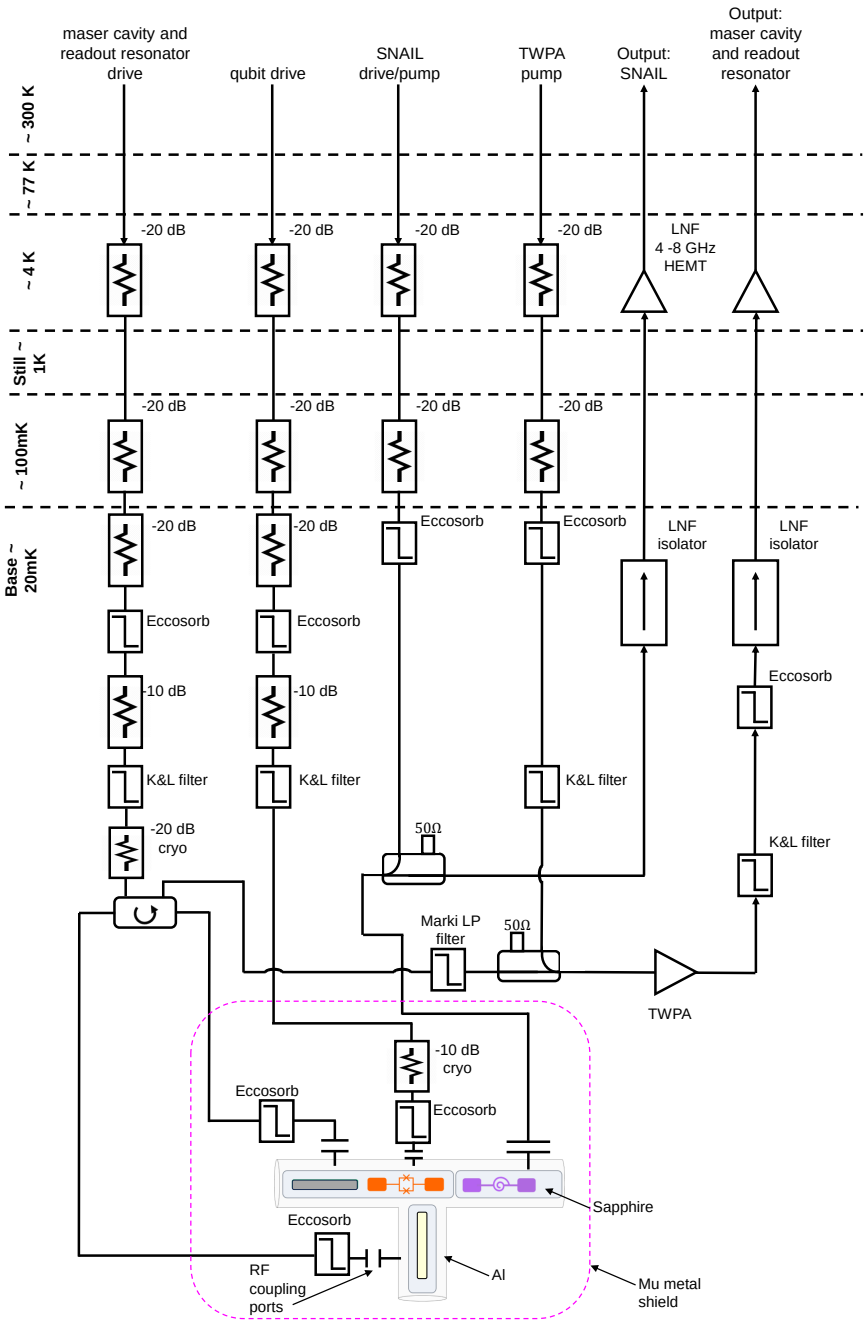


Figure 58: **Cryogenic diagram** A diagram of the full cryogenic input and output setup for our maser. The masing cavity and readout resonator are chained on the same input/output chain because they are spectrally separated and never simultaneously measured. The qubit is only driven and the SNAIL read for diagnostics. During the masing process, only two pumps are driven: the TWPA and $\Sigma$ down the SNAIL line, and the masing cavity is read on its output line.

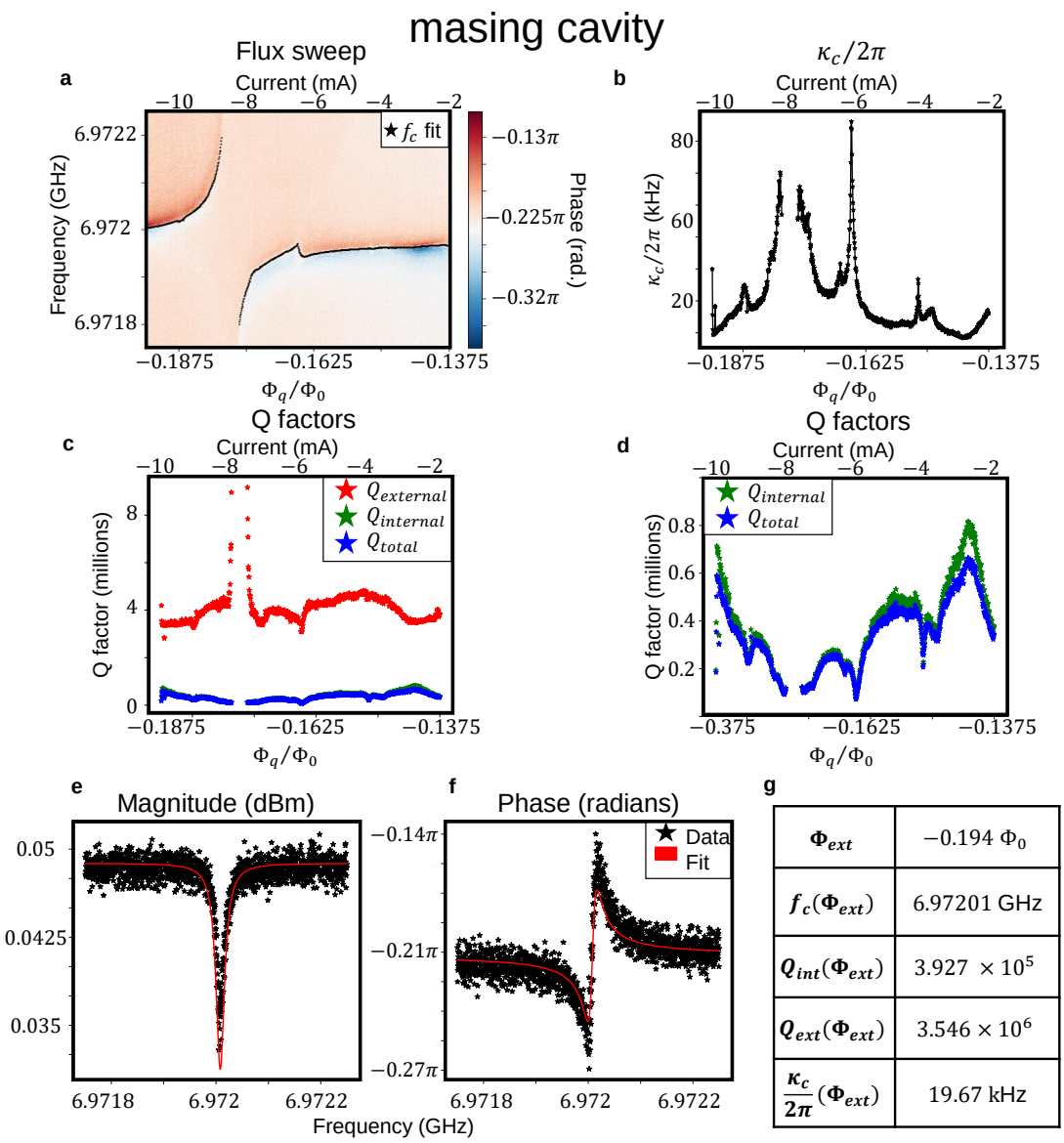


Figure 59: **Flux sweep and fit parameters: masing cavity** A sweep of the qubit magnet's current changes the externally applied flux to the SQUID loop, and we can observe its hybridization with the masing cavity when it approaches in frequency. (a) Single tone spectroscopy of the cavity, showing two avoided crossings where the qubit would intersect with the cavity. (b) A fit for $\frac{\kappa_c}{2\pi}$ vs. flux. The cavity increases in linewidth as it hybridizes with the transmon. (c, d) A fit for the Q factors of the cavity vs. flux. (e, f) A data cut at a single bias flux. (g) The cavity's magnitude and phase response are fit to extract typical cavity parameters.

To find the qubit bias condition where the qubit's unhybridized frequency should match that of the cavity, we sweep the external flux applied through the qubit's magnet. We perform single-tone spectroscopy by weakly probing the cavity on the VNA and sweeping the output of a room temperature current source (YOKOGAWA GS200) connected to the magnet directly over the SQUID, see Fig. 59(a-d). When the two modes hybridize, we see an avoided level crossing, or a divergence in the mode frequency that appears on the VNA. This is the point where the Jaynes-Cummings Hamiltonian

$$H_{int} = g_{qc}(q^\dagger c + q c^\dagger) \tag{83}$$

is valid, causing a re-diagonalization of the the system where now one eigenmode goes up in frequency by $g_{qc}$, and one goes down by $g_{qc}$. However, at this point, the two modes (qubit and cavity) are no longer distinguishable. Rather we are now in this 'quton' and 'phobit' regime [105] where neither mode exists as its own entity. We can fit this avoided crossing to extract $\frac{g_{qc}}{2\pi} = 0.44$ MHz in Fig. 60(a).

Moving the qubit's frequency through the cavity's shows us what current must be supplied to induce the masing procedure, as well as an initial guide for where the SQUID is located in frequency space. SQUIDs follows a $\sqrt{I_c|\cos\Phi_{ext}|/\Phi_0}$ trajectory vs. flux/applied current but we do not know of any offset fluxes. With the flux sweep as a guide, we can more easily probe the qubit in spectroscopy and pulsed measurements rather than blindly searching through potential qubit frequencies at a particular applied flux bias.

The resonator's frequency also varies with qubit flux, and must be measured at unique bias conditions. We can perform a flux sweep of the qubit magnet while measuring the readout resonator on the VNA. The qubit and resonator do not cross in frequency, as the qubit's highest frequency was designed to be below that of the resonator. Although there is not an avoided level crossing, we can see the resonator shifted up in frequency when the qubit is nearest, see Fig. 61.

The qubit's frequency can be found in CW spectroscopy. At different applied currents, we perform two-tone spectroscopy by weakly probing the readout resonator and varying the frequency of a tone sent down the qubit's injection line. Higher qubit drive powers show

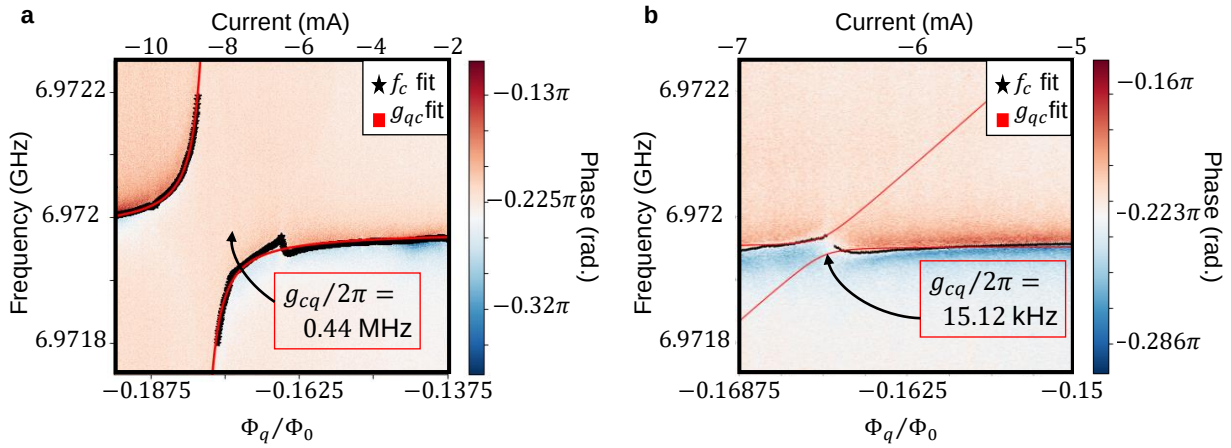


Figure 60: **Avoided crossing: qubit and cavity** Weakly measuring the cavity while sweeping the SQUID's flux brings the qubit into resonance with the cavity. When they hybridize, their coupling Hamiltonian of Eq. 83 is rediagonalized with one eigenvalue shifted by up $g_{qc}$ and the other down by $g_{qc}$. (a) When the qubit's $f_{ge,\text{bare}} = f_{c,\text{bare}}$ they couple with strength $\frac{g_{qc}}{2\pi} = 0.44$ MHz. (b) When $f_{gf/2,\text{bare}} = f_{c,\text{bare}}$ they couple with strength $\frac{g_{qc}}{2\pi} = 15.12$ kHz.

higher order qubit transitions, showing an anharmonicity of $\frac{\alpha_q}{2\pi} = -163.6$ MHz, and a two-photon $f_{gf/2}$ halfway between $f_{ge}$ and $f_{ef}$. CW spectroscopy data allows us to map the qubit's frequency to bias conditions. With a handful of discrete data points, we can fit qubit frequency vs. flux $\propto \sqrt{I_c|\cos\Phi_{ext}|/\Phi_0}$. In the region where we will operate the maser, the curve is fairly linear.

The qubit's frequency trajectory allows us to understand the cavity flux sweep. We are primarily concerned with the qubit's $f_{ge}$ crossing the cavity, but cannot forget that the transmon is not just a two level qubit! In the flux sweep of Fig. 59(a), we note secondary and even small tertiary splittings that were are first unexplained, fit in Fig. 60. We overlay the qubit's $f_{ge}$ frequency path on top of the flux sweep colorplot, finding the qubit fit frequency equal to the cavity's unperturbed frequency at the same flux bias where the largest avoided

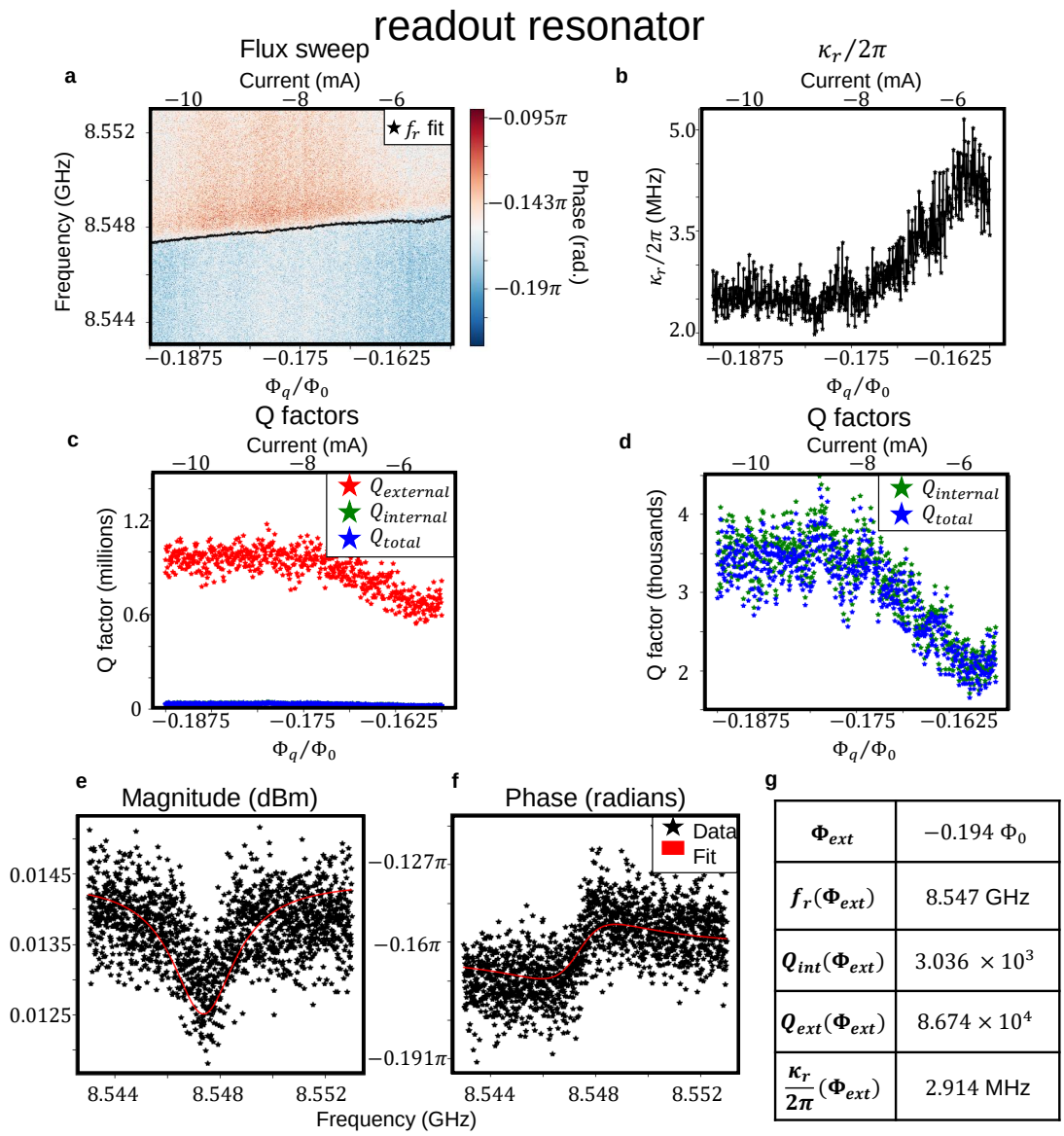


| | |
|---|---|
| $\boldsymbol{\Phi_{ext}}$ | $-0.194\ \Phi_0$ |
| $\boldsymbol{f_r(\Phi_{ext})}$ | 8.547 GHz |
| $\boldsymbol{Q_{int}(\Phi_{ext})}$ | $3.036 \times 10^3$ |
| $\boldsymbol{Q_{ext}(\Phi_{ext})}$ | $8.674 \times 10^4$ |
| $\boldsymbol{\frac{\kappa_r}{2\pi}(\Phi_{ext})}$ | 2.914 MHz |

Figure 61: **Flux sweep and fit parameters: readout resonator** A sweep of the qubit magnet's current changes the externally applied flux to the SQUID loop, and we observe its effect on the readout resonator on the VNA. (a) Single tone spectroscopy of the resonator. It is not constant vs. flux, indicating non-negligible coupling to the qubit, allowing for dispersive readout. (b) A fit for $\frac{\kappa_r}{2\pi}$ vs. flux. The cavity increases in linewidth as it approaches the transmon. (c, d) A fit for the Q factors of the resonator vs. flux. (e, f) A data cut at a single bias flux. (g) The resonator's magnitude and phase response are fit to extract typical resonator parameters.

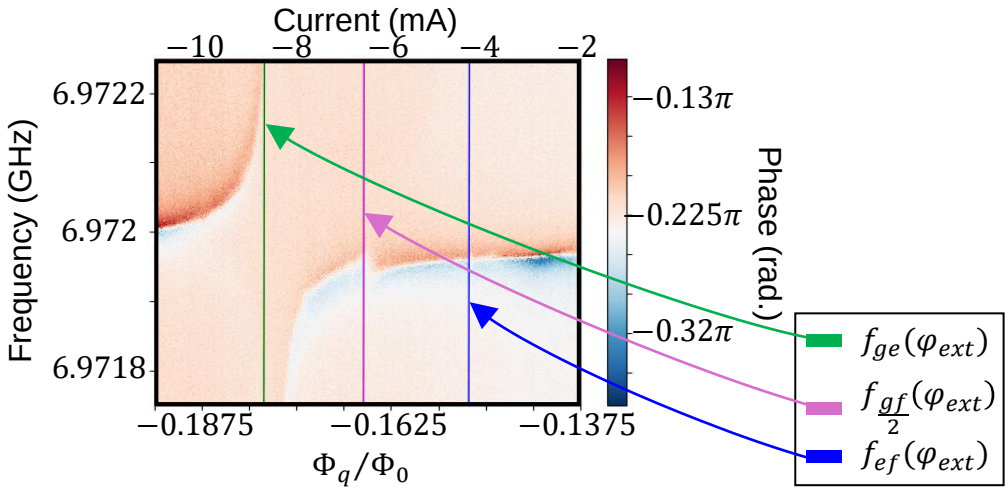


Figure 62: **Flux sweep vs. qubit spectroscopy** The qubit frequencies found in spectroscopy are fit $\propto \sqrt{I_c|\cos\Phi_{ext}|/\Phi_0}$ and projected over the flux sweep probing the masing cavity. The avoided crossings nearly align with the qubit's frequency trajectory. This will guide us in choosing a qubit magnet bias.

crossing occurred in Fig. 62 in green. We also overlay the qubit's $f_{gf/2}$ and $f_{ef}$ frequencies on top of the flux sweep colorplot in pink and blue respectively, and find the second and third smaller splittings occur at the same bias conditions where the qubit's $f_{gf/2}$ and $f_{ef}$ fit equal the unperturbed cavity. These unintended but, in retrospect, predictable cavity splittings will play an important role in the masing procedure.

The qubit frequency trajectory plotted in Fig. 62 is from a single fridge cycle, but typical for the response seen in multiple cooldowns. An issue we sometimes encountered was flux offsets varying from run to run. In a number of cooldowns, the bias condition needed for $\Delta_{qc} = 0$ was at a current that caused the magnet to physically heat the sample and the entire fridge. The period of a flux quantum for the SQUID was greater than designed and small offsets in flux period produce large offsets in frequency. In more recent cooldowns, we changed the qubit magnet to breakout at the 4 K stage of the fridge to bias at higher currents, see Fig. 56.

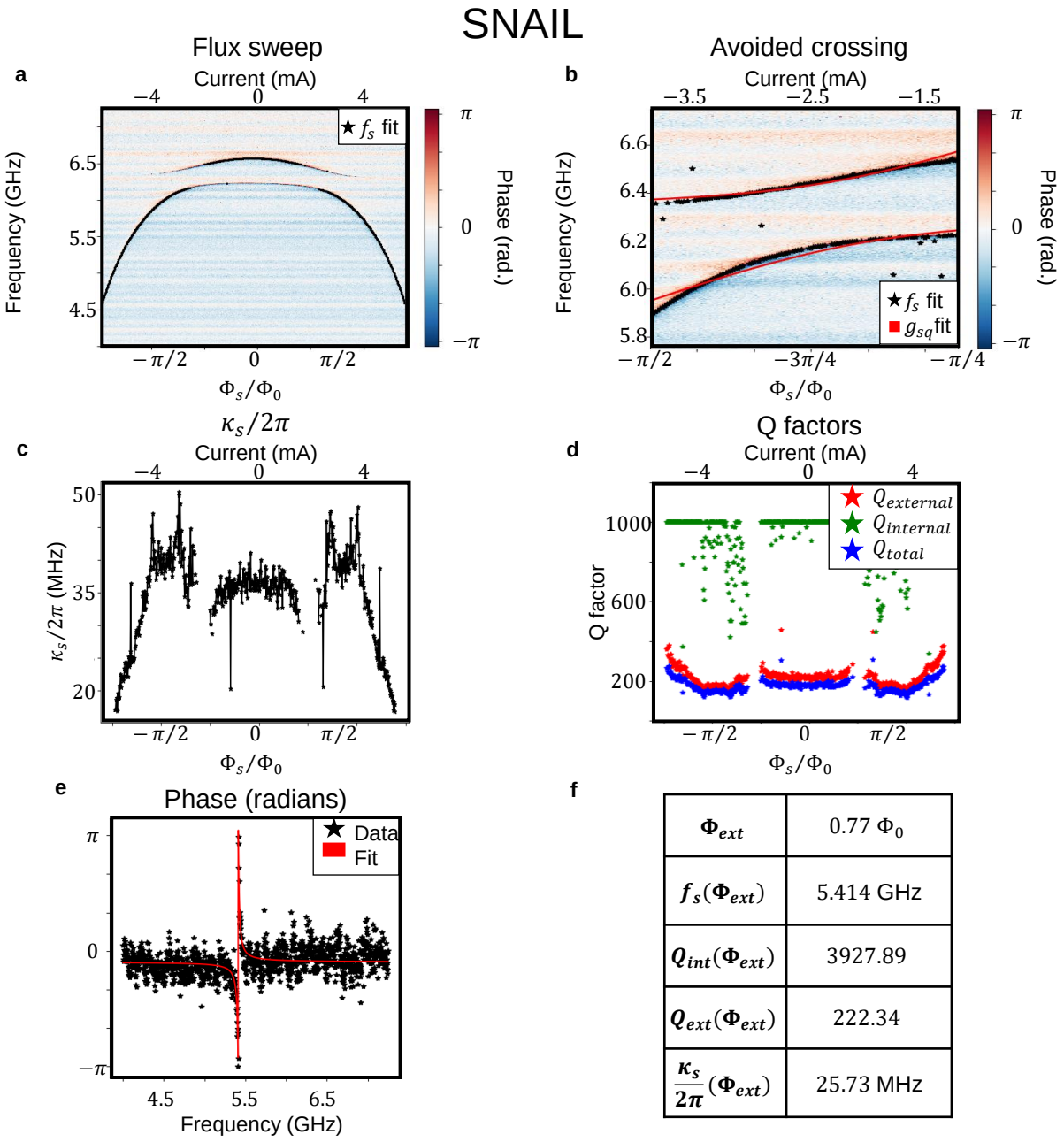


| | |
|---|---|
| $\boldsymbol{\Phi_{ext}}$ | 0.77 $\Phi_0$ |
| $\boldsymbol{f_s(\Phi_{ext})}$ | 5.414 GHz |
| $\boldsymbol{Q_{int}(\Phi_{ext})}$ | 3927.89 |
| $\boldsymbol{Q_{ext}(\Phi_{ext})}$ | 222.34 |
| $\boldsymbol{\frac{\kappa_s}{2\pi}(\Phi_{ext})}$ | 25.73 MHz |

Figure 63: **Flux sweep and fit parameters: SNAIL** We sweep the bias on the SNAIL's magnet and probe the mode on the VNA. (a, b) There is an avoided crossing near the top of the SNAIL's trajectory where it would intersect with the transmon at its particular bias. This allows us to fit the direct $\frac{g_{qs}}{2\pi} = 138.8$ MHz. (c, d) The bandwidth $\kappa_s$ and Q factors vary with external bias. The $Q_{s,int}$ factor dominates the expression for $Q_{s,total}$. (e, f) Typical parameters from a single bias condition.

Next, we measure the SNAIL on the VNA in Fig. 63. Similarly, it has a high power response and moves in frequency with external bias through the SNAIL's magnet. Unlike a harmonic cavity, the SNAIL's nonlinear coefficients change with flux. We wish to operate the SNAIL at a bias of high $g_3$ and minimal $g_4$. Experimentally we can choose this bias in multiple ways. A sweep for duffing oscillator behavior, with a secondary tone sent in at $5 \times \kappa_s$, shows how the mode frequency bends with increased power. Kerr minimization corresponds with minimized mode bending, which is achieved in this experiment at nearly 4.5 GHz in Fig. 64. We also can model the SNAIL's coefficients using the equations listed in Ref. [14], mapping a fit of the frequency modulation from the flux sweep with known parameters like $\alpha_s, L_{lin}$, and $C_{lin}$.

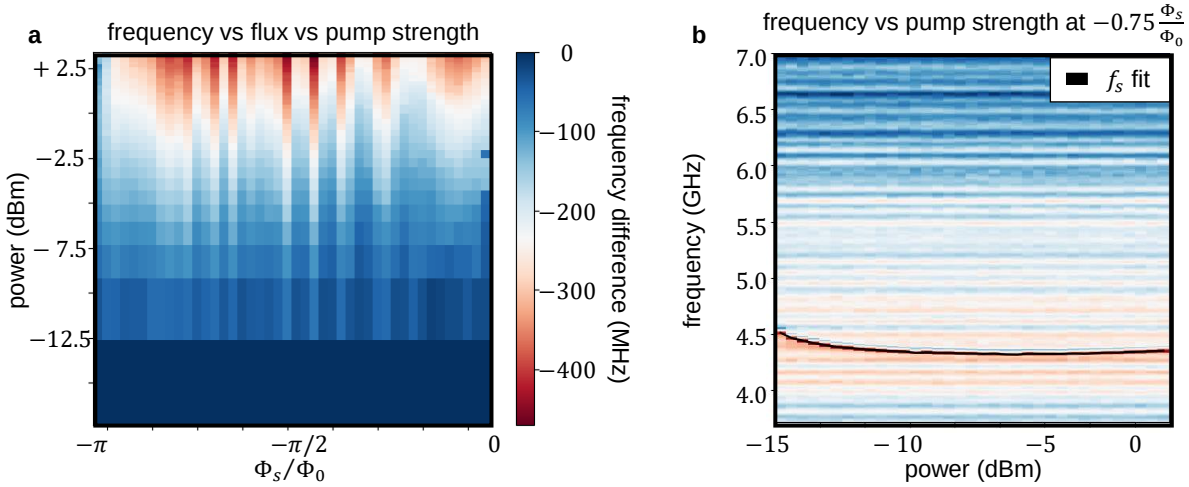


Figure 64: **Duffing sweep on the SNAIL** (a) At each SNAIL magnet bias (x-axis) and detuned continuous tone power (y-axis) we measure the SNAIL mode on the VNA and fit for its frequency. The color represents the difference from the lowest power per current. This shows where the SNAIL has minimal self-Kerr, in the vertical stripes where the frequency changes the least from bottom (lowest powers) to top (highest powers). (b) At nearly $-0.75\frac{\Phi_s}{\Phi_0}$, the downward bend in frequency is at a minimum. This should be the SNAIL's $g_4 = 0$ operation point.

The SNAIL and qubit do show some flux cross-talk in experiment. At a fixed SNAIL

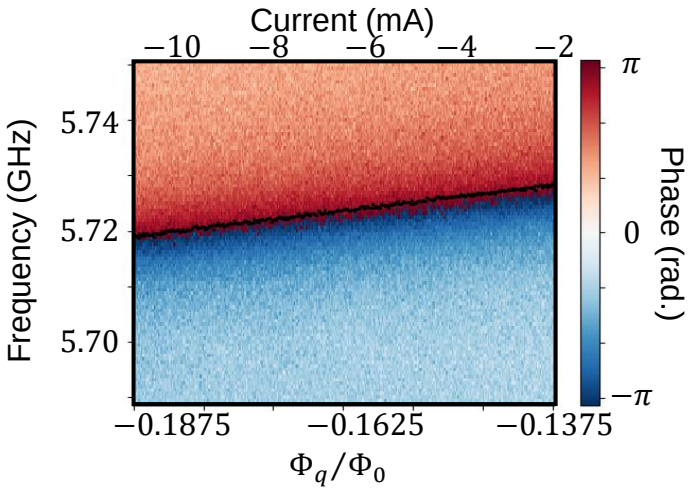


Figure 65: **Qubit flux sweep affecting the SNAIL** We sweep the bias on the qubit's magnet and probe the SNAIL mode on the VNA. At this particular SNAIL bias used throughout the experiment, the SNAIL moves nearly 9.45 MHz by changing the qubit's magnet and keeping the SNAIL's fixed. This can be significant to the detuning needed in $f_d = f_s + f_{q,ge} + \gamma_d$.

magnet current, we swept the qubit's magnet in the current range near qubit-cavity resonance in Fig. 65. We see the SNAIL move in frequency, on order of its bandwidth $\kappa_s$. Our parametric pump, actuated through the SNAIL at a three-wave mixing point, is driven at $f_d = f_s + f_{q,ge} + \gamma_d$, so we need to know $f_s$ for a particular $\Phi_{total}$, which is the total externally applied flux and a function of both magnets. Therefore at each qubit current, we must make a small correction to the SNAIL magnet's current to keep its frequency and nonlinearity fixed. This correction factor was measured by manually adjusting SNAIL flux at discrete qubit flux such that the SNAIL's frequency remained unchanged, and fit to a line using $\Phi_{s,new} = m\Phi_q + b$ for slope $m$ and offset $b$.

A TWPA [92] also backed the masing cavity and readout resonator, which are on the same readout chain. Its pump conditions were chosen such that the signal was amplified by 20dB at the masing cavity's frequency. The SNAIL is unaffected by the TWPA. The readout resonator frequency is also amplified near 20dB. This amplifier was chosen because

its dispersive feature and the necessary pump are well separated from any mode in the system. Such a backing amplifier means we can perform less averages for readout, crucial if watching the cavity as it mases and evolves on short time scales.

## 5.4 Maser Pulsed Measurements

### 5.4.1 Qubit Diagnostic Measurements

Qubit lifetimes and performance was measured using the QICK platform [100] on a Xilinx ZCU111 board. Special care must be taken to operate the DAC and ADC at the correct frequencies per Nyquist zone to avoid issues like aliasing. See Chao Zhou's thesis [38] for a full explanation of this issue. The room temperature measurement apparatus for this experiment uses both generators (SignalCore SC5511A) and mixers for both input and digitized output, see Fig. 66.

We started with qubit measurement, a task made easier by knowing the qubit frequency per bias based on CW spectroscopy (Fig. 62). We probe the qubit by dispersively measuring the readout resonator. A snapshot of typical qubit measurements is shown in Fig. 67, when the qubit is off resonance from the masing cavity. We note that qubit lifetimes are significantly shorter than expected, compared to Table 3. This is likely due to imperfections in the metal housing, fabrication, and misalignment of the sapphire chips within their tubes. We also measure the qubit's performance across a span of flux biases in Fig. 68. The qubit seems to improve in energy decay lifetime $T_1$ near the secondary small qubit-cavity splitting seen in Fig. 60(b). Dephasing times $T_{2,R}$ and $T_{2,E}$ remain low but show modest improvement near the $f_{q,ge}$ cavity crossing (Fig. 60(a)). It is not surprising that this qubit has coherence times- SQUIDs are highly sensitive to changes in local magnetic flux. This leads to dephasing because our qubit is susceptible to low frequency noise.

Qubit lifetimes contribute to maser performance. First, the parametric pump to invert qubit population is working against qubit energy decay, shown in detail in Sec. 4.3.2 on our first generation experiment. Second, if the qubit is not frequency stable, as our low

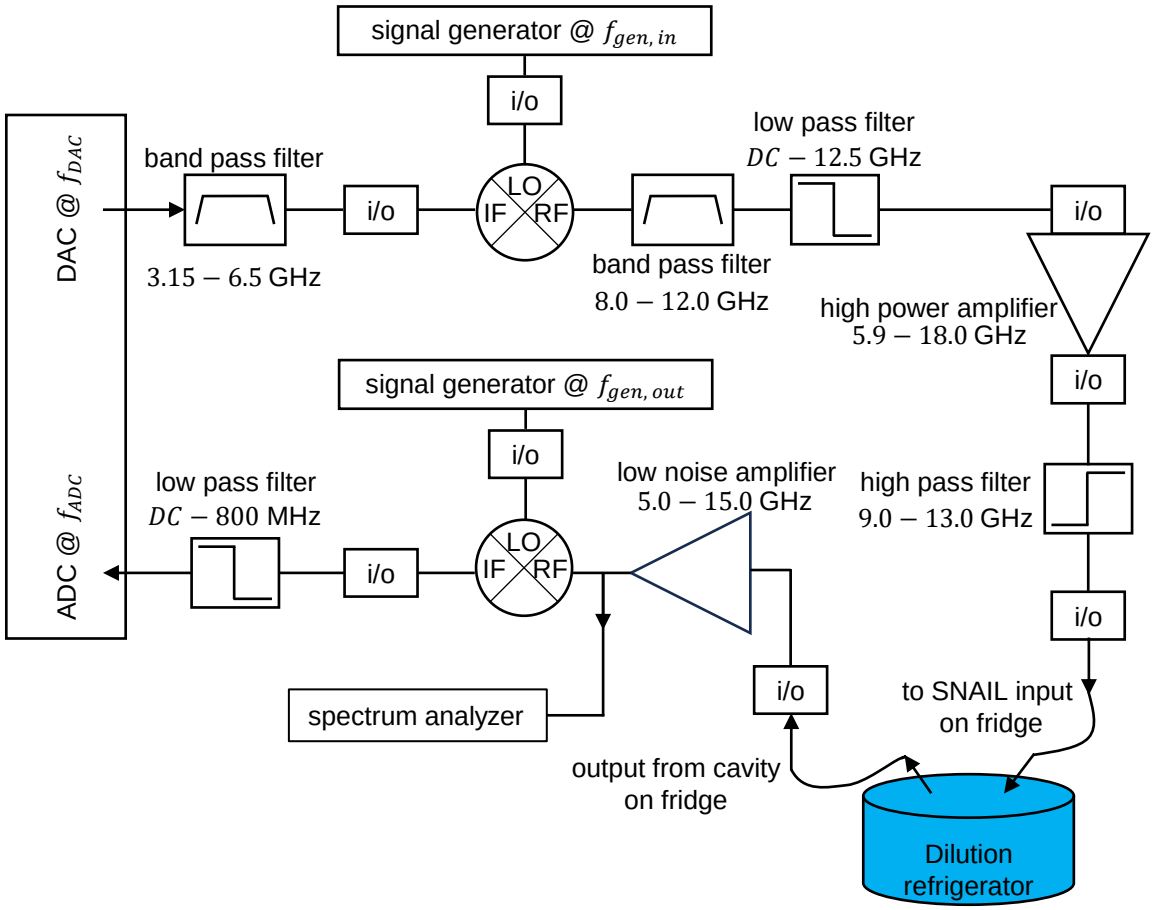


Figure 66: **Room temperature microwave electronics** The input for the parametric pump $\Sigma$ drive down the SNAIL input line, and output from the masing cavity on its dedicated output line. Signals are generated by the DAC at $f_{DAC}$, which mixes with an LO $f_{gen,in}$ to send frequency into the fridge at $f_{DAC} - f_{gen,in} = f_d = f_s + f_q + \gamma_d$. There are a series of filters to prevent unwanted sidebands and AWG aliasing tones from going into the fridge, which can potentially interfere with the intended processes. To read out the signal from the cavity, we can choose two options. We can measure broad band responses on the spectrum analyzer, and/or can we digitize the signal by mixing the cavity output signal $f_c$ with generator tone $f_{gen,out}$ to reach the ADC at $f_c - f_{gen,out} = 90$ MHz.

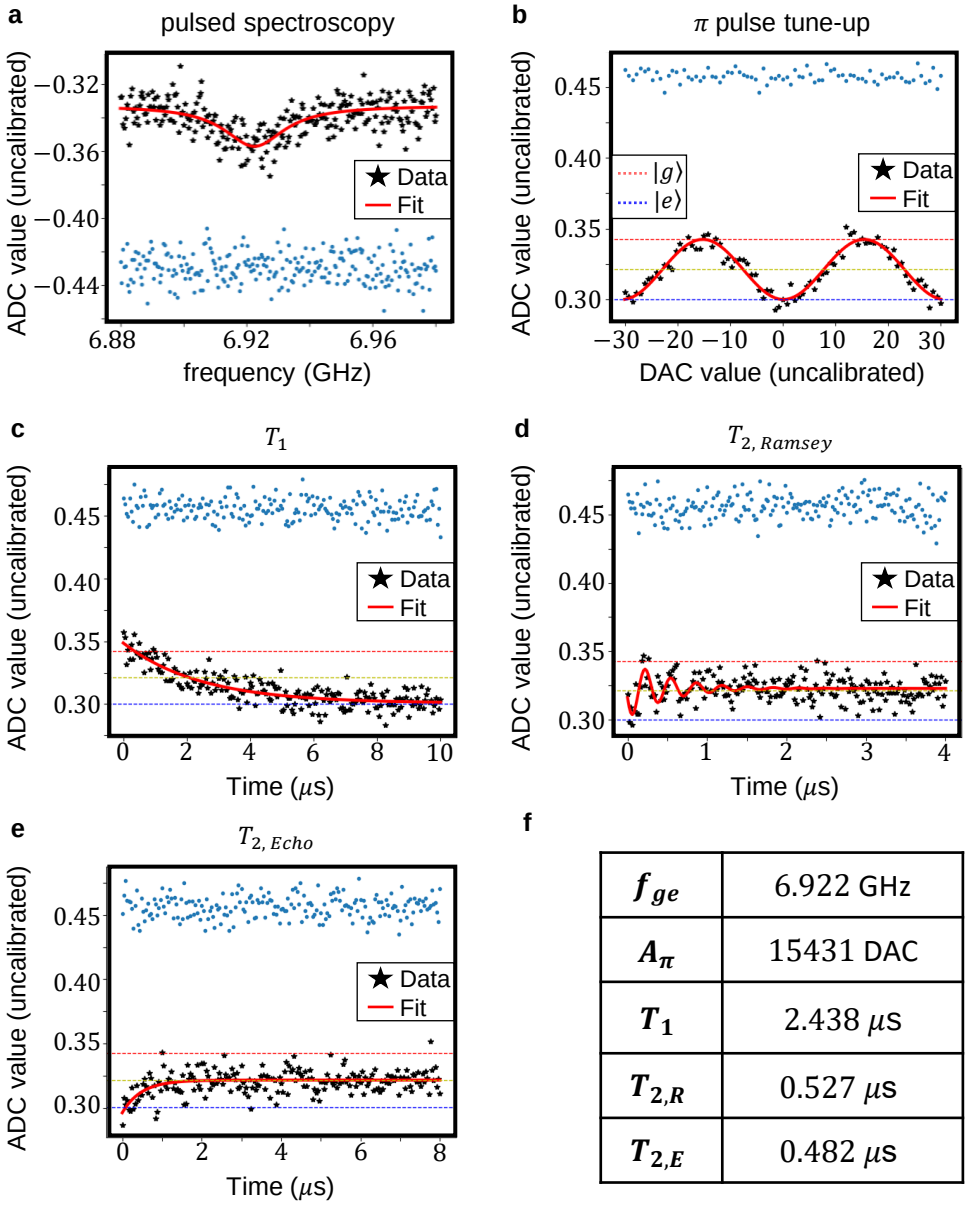


| | |
|---|---|
| $f_{ge}$ | 6.922 GHz |
| $A_\pi$ | 15431 DAC |
| $T_1$ | 2.438 μs |
| $T_{2,R}$ | 0.527 μs |
| $T_{2,E}$ | 0.482 μs |

Figure 67: **Typical qubit measurements** The qubit is measured at nearly $\Delta_{qc} = 50$ MHz. Following the pulse sequences in Fig. 32, we measure the qubit by dispersively measuring the readout resonator. Fitted values are listed in (f).

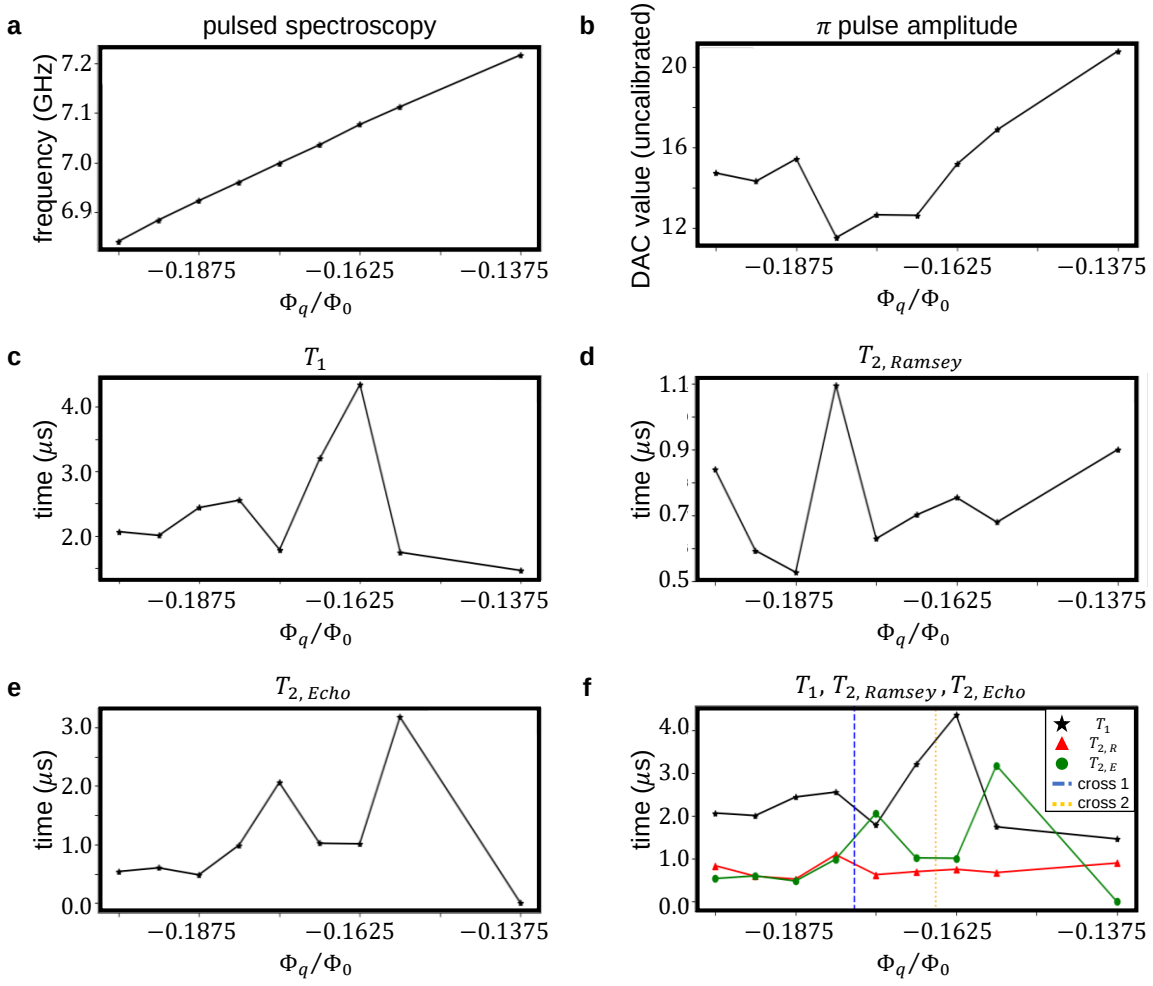


Figure 68: **Typical qubit measurements vs. flux** Qubit performance changes with qubit-cavity detuning. (a) In this small region of flux, the qubit's trajectory is linear. (b) $\pi$ pulse amplitude (c) $T_1$ improves near the second small qubit-cavity crossing. (d, e) $T_{2,Ramsey}$ improves near the primary largest qubit-cavity crossing. (f) All qubit lifetimes compared. The vertical lines correspond to the bias conditions where $f_{q,ge}$ (blue) and $f_{gf/2}$ (yellow) cross the cavity frequency.

$T_{2,R}$ suggests, then the parametric pump is difficult to tune. We want to pump at $f_d = f_s + f_{q,ge} + \gamma_d$, and any detuning $\gamma_d$ should ideally be understood, rather than random with qubit frequency fluctuation. Flux noise follows a $1/f$ trend. If the noise does not fit to this loss frequency model, flux noise is not the source of our trouble and there is some other source of dephasing.

To understand how the qubit is fluctuating with time, we repeat the measurement sequence $[T_1, T_{2,R}, T_{2,E}, \Sigma_{s,ge}]$ at a single bias condition over the course of many hours. This data shows the qubit undergoes significant changes in its performance over time, a possible contributing factor to the masing data that will be shown in Sec. 5.4.3. The lifetimes change within a factor of two over short time scales, and the frequency of the qubit (represented by the detuning measured from Ramsey beating $f_{\delta,Ramsey}$) fluctuates on order of 200 kHz. This can cause trouble, as our parametric pump can change efficacy at a fixed frequency if the qubit itself is changing frequency. Our room temperature electronics in Fig. 66 are contained in a temperature stabilized box like in Ref. [93]. See Sec. 5.4.3.6 for greater detail. The temperature of the box still changes on order of 0.006° C which can alter the performance of its internal components.

### 5.4.2 Qubit Inversion

Next we measure qubit inversion rates. Using the same technique for transmon heating as in the bath engineered qubits project, Sec. 4.3, we apply the $\Sigma_{s,ge}$ pump to the SNAIL to bring the qubit from $|g\rangle \rightarrow |e\rangle$, and then dispersively measure the qubit through the readout resonator. During the masing process, described below, we do not directly drive the qubit, measure it, or involve the readout resonator at all. This exercise in measuring transmon heating rates tells us the viability of masing in our system.

Much like a traditional maser/laser system, we require a population inverted gain medium that emits multiple photons, which populate the masing cavity. Our gain medium, the transmon, is inverted by the parametric heating process. Masing occurs when the transmon is sufficiently inverted, or its $|e\rangle$ population is replenished before directly exchanging its photon with the cavity. We cannot measure the rate of inversion in this method when the

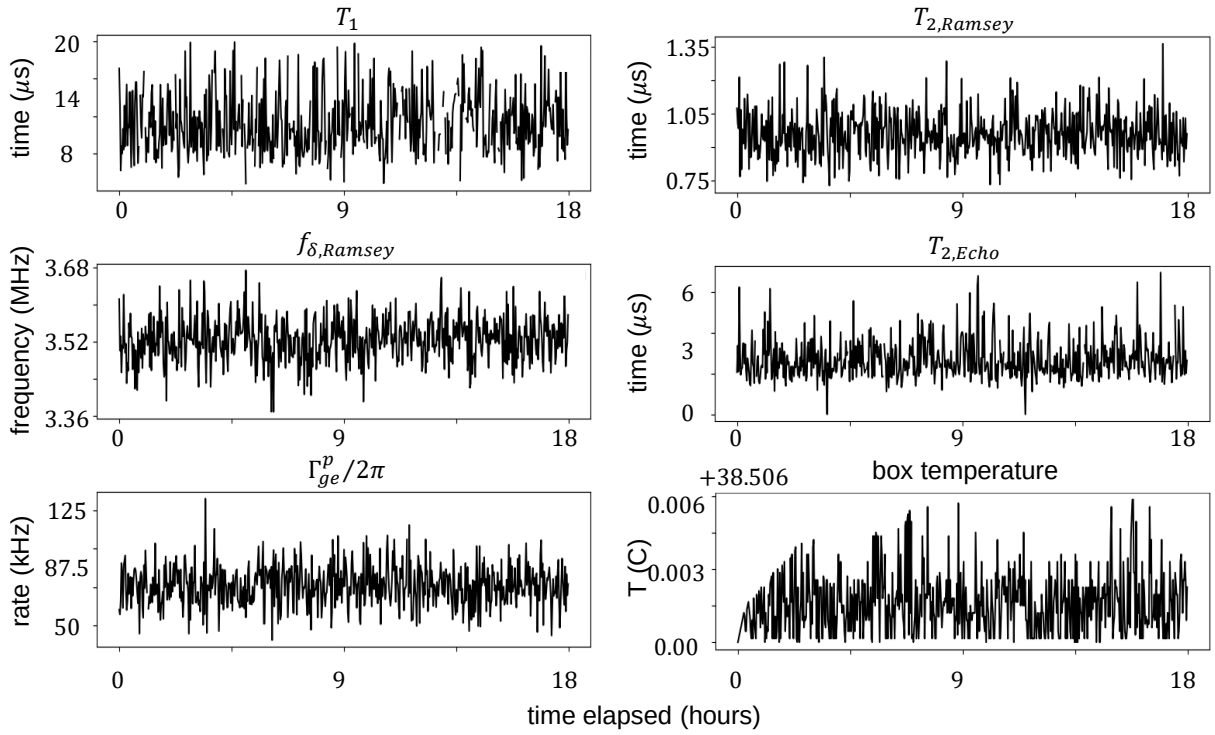


Figure 69: **Qubit measurements vs. time** The qubit is measured for 18 hours at a fixed $\Phi_{ext,total}$, so fixed SNAIL and qubit biases. The lifetimes $T_1, T_{2,R}$, and $T_{2,E}$, qubit frequency, and inversion rate $\Gamma_{ge}^{p}$ fluctuate with time, indicating the performance of the maser will be impacted by qubit performance unless corrected.

qubit is nearly resonant with the cavity, so we measure its inversion rate at nearby bias conditions (Fig. 70). This gives us a sense of what pump conditions will successfully drive masing. We can control the pump frequency $f_d(\Phi_{ext}) = f_s(\Phi_{ext}) + f_q(\Phi_{ext}) + \gamma_d$ and pump amplitude $\epsilon_d$ for each bias condition, or rather $f_s(\Phi_{ext})$ and $f_q(\Phi_{ext})$.

At each bias, we see the inversion rate $\Gamma_{ge}^{p}$ follow [63]:

$$\Gamma_{ge}^{p} = \frac{4g_{\Sigma_{s,ge}}^{2}}{\kappa_s} \tag{84}$$

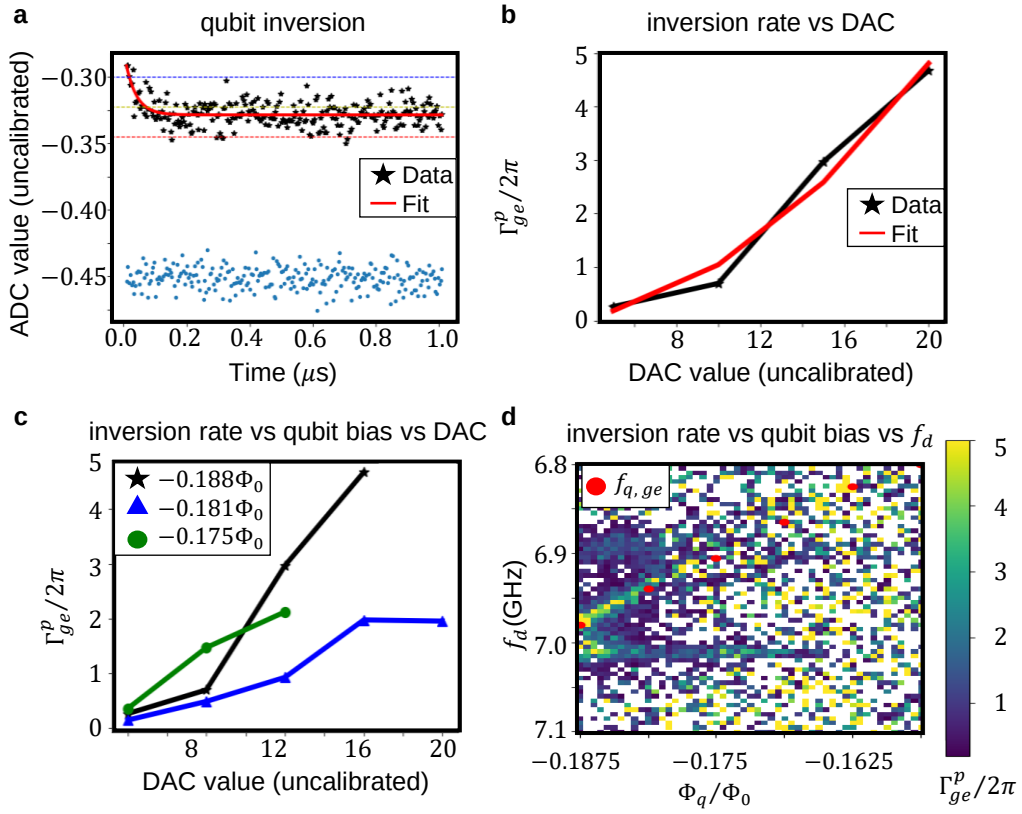


Figure 70: **Qubit inversion** (a) At a fixed $\Phi_{ext,total}$, $f_d$, $\epsilon_d$, we apply the parametric pump and dispersively measure qubit state using the pulse sequence of Fig. 36(a). We measure $\Gamma^p_{ge}/2\pi = 4.67$ MHz. (b) At that same $\Phi_{ext,total}$, $f_d$, we increase the pumping strength $\epsilon_d$ through increasing the DAC output on our AWG. This increases $g_{\Sigma_{s,ge}}$. The curve follows a quadratic speed up with respect to $g_{\Sigma_{s,ge}}$. (c) Repeating the experiment of (b) at different qubit bias conditions. Some qubit points are better inverted than others, due to improper detunings in our pump frequency. (d) Sweep qubit bias (x-axis) and pump frequency difference from $f_d - f_s$ (y-axis) to find the maximum inversion rates follow the qubit's frequency trajectory (red circles).

in the limit $\kappa_s \gg g_{\Sigma_{s,ge}}$. At a fixed $\Phi_{ext}$ and $f_d$, varying the pump strength $\epsilon_d$ linearly varies $g_{\Sigma_{s,ge}}$. We need to maintain

$$\kappa_s \gg \Gamma_{ge}^{p} > g_{qc,\text{effective}} \gg \Gamma_c. \tag{85}$$

The rates $\kappa_s, \Gamma_{ge}^{p}, g_{qc,\text{effective}}$, and $\Gamma_c$ are also all a function of bias condition, $\Phi_{ext}$. When the qubit and cavity are detuned, their hybridization factor decreases and their effective direct coupling becomes $g_{qc,\text{effective}} = \frac{g_{qc}}{\Delta_{qc}}$. Decreasing this term means the rates higher than it may also decrease while still masing. We typically do not want to send too strong of drives into the fridge, and therefore this control knob is helpful in finding the correct balance of rates amongst the entire experiment.

### 5.4.3 Masing

#### 5.4.3.1 Steady State Masing

After confirming the qubit inversion process indeed works, successfully bringing the qubit from $|g\rangle \rightarrow |e\rangle$, we look for light coming out of the masing cavity. In resonantly driven reflection measurements, we typically send a weak probe to the cavity and excite the cavity's electromagnetic mode(s) this way, like an experiment shown in Fig. 71(a, b). On the VNA, we observe the steady state response, looking for the frequency that shifts the reflected tone back to the VNA. On an AWG/digitized rig, we observe how the cavity's response in the IQ plane evolves with time. In either case, we send some type of excitation to the cavity and it responds accordingly. But this is NOT how we will make light come out of our maser.

The qubit and masing cavity are coupled with an always-on exchange at rate $g_{qc,\text{effective}}$. The qubit exchanges energy with the cavity, leading to photons building up in the cavity, which leave at rate $\Gamma_c$. As long as the qubit is population inverted, it will always have the necessary photon to exchange with the cavity. Through this process, we are exciting the cavity through indirect drives. We can measure the cavity's output on a spectrum analyzer because it is a one port received, rather than two port reflected, signal to the analyzer (Figs. 66, 71(c)). Additionally, we expect the output frequency of the maser to be shifted based on factors like its photon number occupation and qubit-cavity detuning. With all of

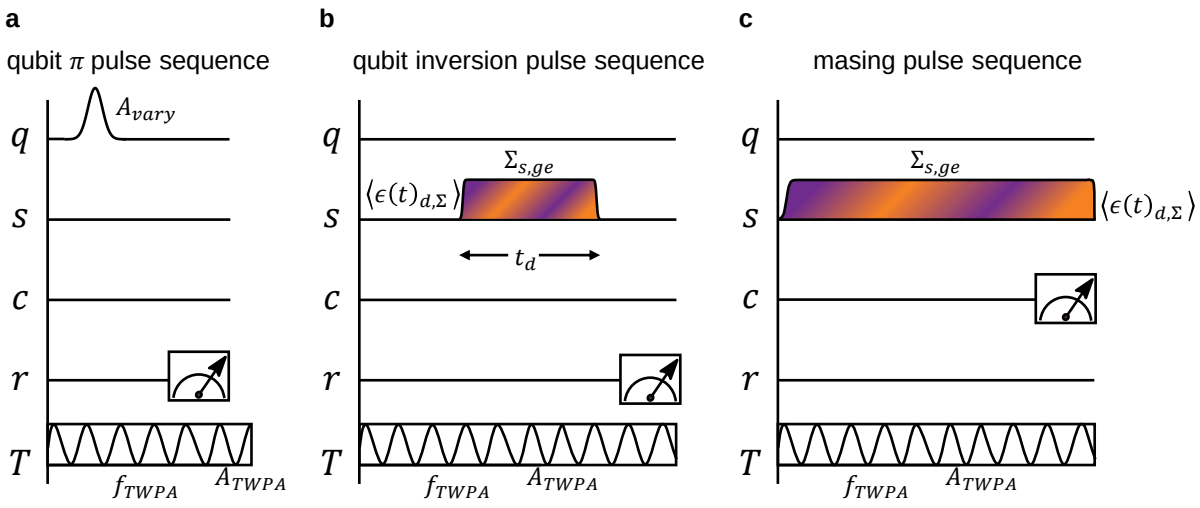


Figure 71: **Microwave pulse sequence for the maser** (a) A typical pulse sequence to drive and measure a qubit. (b) The pulse sequence used to measure qubit inversion rates. The readout resonator shifts its response based on the effect of the $\Sigma_{s,ge}$ drive. (c) In our masing experiment, we send a continuous $\Sigma_{s,ge}$ drive and observe what is emitted by the cavity after some time.

the correct bias conditions and the parametric pump turned on, we connect the output of the masing cavity to the spectrum analyzer and observe a narrow emission spectrum, some typical values shown in Fig. 72. We measure both the amplitude $P_c^{masing}$ and full width at half maximum (FWHM) linewidth $\Gamma_c^{masing}$. This is masing!

The bias and drive conditions on the maser are also not trivial to optimize. I will now walk through the efforts taken to find combinations of system parameters that induce (to varying levels of success) the masing process, and what conclusions we draw about our experiment based on these needs. There are a number of experimental controls that I can change in situ, causing the response of the entire system to shift. I can directly change: $\Phi_s,\ \Phi_q,\ f_d,\ \eta_d/\epsilon_d$. This in turn affects: $f_s,\ f_q,\ f_c,\ \kappa_s,\ \kappa_q,\ \kappa_c,\ g_3,\ g_4,\ g_{s^n},\ \Gamma_{ge}^p$ and ultimately $\Gamma_c^{\text{masing}}$ and $P_c^{\text{masing}}$. None of these measured changes are completely independent of one another. While I can independently tune, for example, $\Phi_s$, this causes changes to not only the SNAIL's properties,

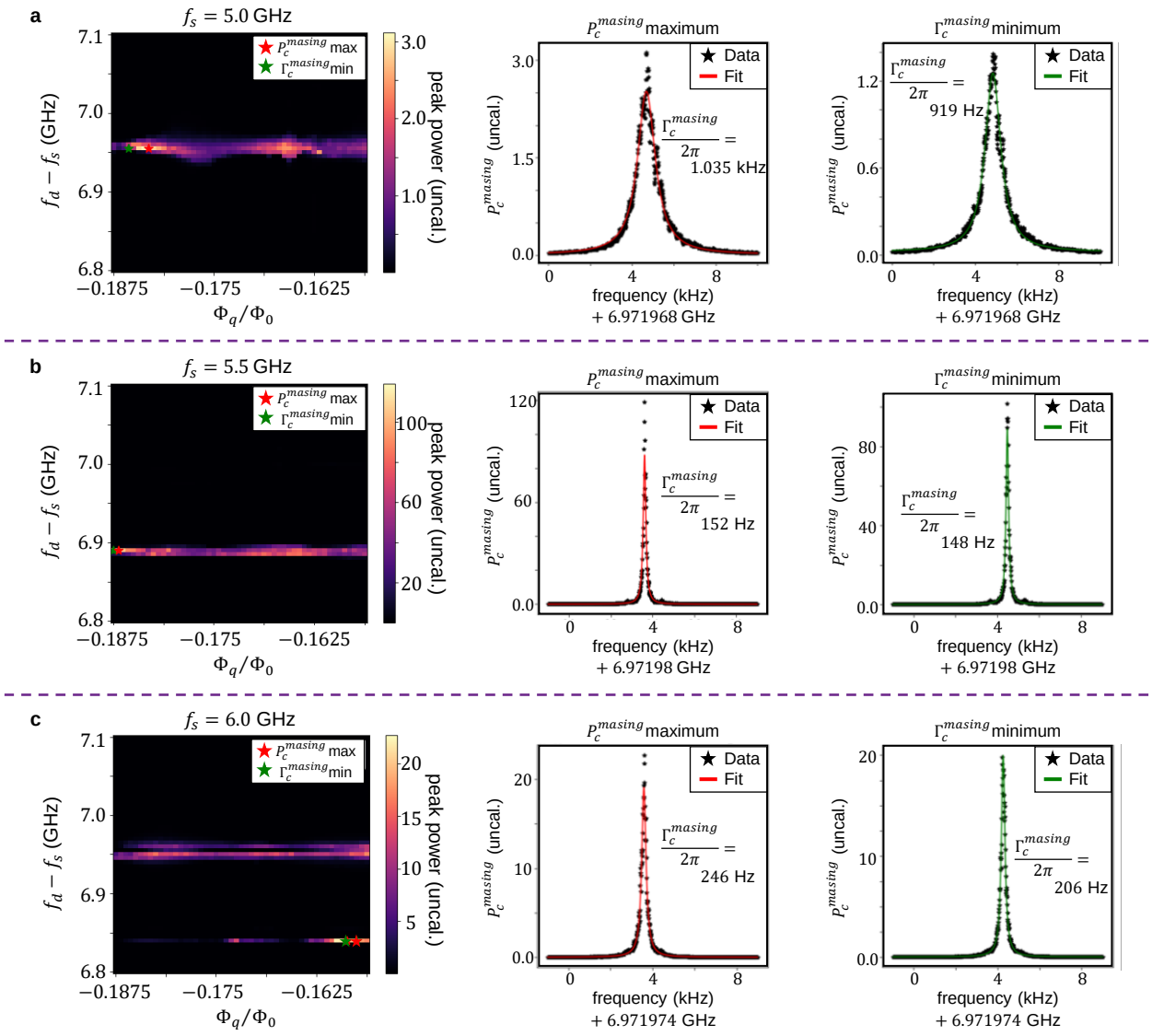


Figure 72: **Masing vs. SNAIL bias, qubit bias, pump frequency** In each colorplot, we vary flux through the qubit magnet ($\Phi_q$) at a fixed $f_s, g_3, g_4$, and $\epsilon_d$. We also vary the pump frequency, here marked as the difference in $f_d - f_s$. We measure the cavity's output on the spectrum analyzer, and note bright emissions across biases. The maximum brightness output in the sweep $P_c^{masing}$ is marked in red and the minimum bandwidth in the sweep $\Gamma_c^{masing}$ marked in green. Top to bottom we vary SNAIL bias to change its frequency and nonlinear coefficients (a) $f_s = 5.0$ GHz (b) $f_s = 5.5$ GHz, and (c) $f_s = 6.0$ GHz.

$f_s$, $g_3$, $g_{s^n}$, and $\kappa_s$, it also causes changes to the qubit and cavity modes. This requires tuning multiple parameters in order to reach the maser state we desire due to hybridization. Some of these effects can be predicted, but most are not and so I have spent a good amount of time 'wrangling' the system into order.

I started with the SNAIL at a fixed $f_s \approx 5.5$ GHz, see Fig. 72(b). Although this bias condition is not where we find minimal static Kerr (see Fig. 64), it is a bias point that produced fast and clean qubit inversions, so it likely maximizes $g_3$. The qubit has a maximum $g_{qc,\text{effective}} = g_{qc}$ when its frequency equals that of the cavity, which is near 6.9719 GHz across multiple cooldowns. This makes the pump without detuning $f_d = f_s + f_q = 11.919$ GHz far from any other known modes or combinations of modes throughout the circuit. There are only two drives in this scheme: the TWPA (which should be far detuned and not an interacting pump) and the SNAIL's parametric pump, see Fig. 71(c). We do not drive the cavity directly!

The cavity emits light that we can observe on the spectrum analyzer. This light peak is a Lorentzian, corresponding to the coherent state it produces via masing. From the spectrum analyzer data, we extract the frequency $f_c^{\text{masing}}$, power output $P_c^{\text{masing}}$ and FWHM to fit for the linewidth $\Gamma_c^{\text{masing}}$ using the formula:

$$\mathcal{L} = \frac{1}{\pi}\frac{\Gamma}{2}\frac{1}{((f-f_0)^2 + \frac{\Gamma}{2}^2)} \tag{86}$$

for a Lorentzian with bandwidth $\Gamma$ and center frequency $f_0$. This gets scaled by:

$$\mathcal{L}_{\text{linear}} = A\mathcal{L} + c \tag{87}$$

to fit the Lorentzian power spectrum in linear units, as our analyzer produces data is in dBm.

We look to see $\Gamma_c^{\text{masing}}$ decrease while $P_c^{\text{masing}}$ increases until we reach the Schawlow-Townes limit:

$$\Gamma_c^{\text{masing}}(STL) = \frac{\Gamma_c}{4\langle n\rangle}. \tag{88}$$

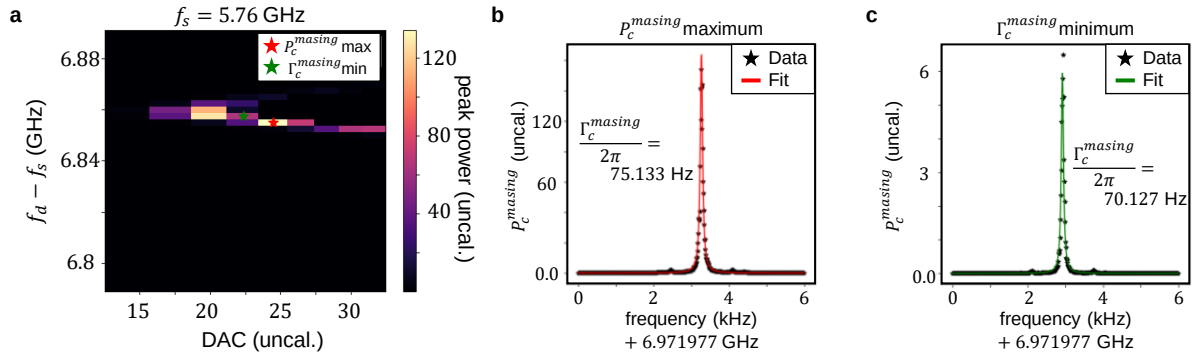


Figure 73: **Masing vs. DAC: fixed $\Phi_{ext}$** (a) At a fixed SNAIL bias and qubit bias, we change the DAC and thus $g_{\Sigma_{s,ge}}$ and $\epsilon_d$. The fits from the brightest (b) and narrowest (c) are shown. The minimum bandwidth is $\frac{\Gamma_c^{masing}}{2\pi} = 70.127$ Hz!

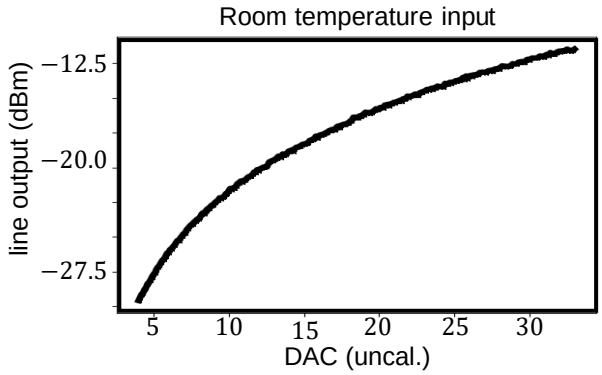


Figure 74: **Room temperature drive strength** The signal sent into the fridge in Fig. 66 increases in amplitude for increased DAC value sent from the AWG. This curve does not yet saturate or decrease in slope before reaching the maximum DAC value. This is in contrast to Fig. 39 where the electronics saturate before filling the DAC. This shows us that our room temperature electronics could be driven harder or amplified without degradation of signal.

for average cavity photon occupation $\langle n \rangle$. We have already measured $\Gamma_c$ on the VNA, considering its bandwidth when the qubit is nearby in frequency but not quite zero detuning because at that point the cavity and qubit are indistinguishable from one another.

Three parameters we swept were the pump amplitude $\epsilon_d$ by changing our AWG's DAC value, the pump frequency with finite detuning $f_d = f_s + f_q + \gamma_d$, and qubit-cavity detuning $\Delta_{qc}$ by changing the qubit magnet's current. These were chosen for a number of reasons. First, we wanted to watch $P_c^{\text{masing}}$ increase and $\Gamma_c^{\text{masing}}$ decrease with higher photon population in the cavity. We expect $\Gamma_{ge}^{p}$ to increase quadratically with $\epsilon_d$, and likewise expect a 'better maser', see Figs. 73 and 75. 'A better maser' means brighter, narrower, and more stable output than at other bias and drive conditions.

Second, we account for small detunings on the SNAIL and qubit in the presence of the parametric pump and increased photon number, so some detuning is to be expected for the pump. This is assuming the SNAIL is not perfectly Kerr-free, and the qubit might be Stark shifted.

At a fixed $\Phi_{total}, f_d$ for fixed static frequencies, we sweep the input amplitude of the drive $\epsilon_d$. We find $\Gamma_c^{\text{masing}}$ reach its minimum and $P_c^{\text{masing}}$ reach its maximum before turning around. This peak in maser performance at a fixed set of particular driving frequency and mode frequencies can tell us about the overall performance of our system. The first question we can address, and the most straightforward to overcome, is the saturation of our microwave electronics. Our drives can only supply input power up to a certain amplitude, and in this experiment we are using a different set up compared to the bath engineered qubits project and so the saturation problem seen in Fig. 39 must be reconfigured for this experiment. Figure 74 shows that we are not yet hitting a saturation point, so the behavior of our cryogenic sample is not limited with diminishing returns on input signal with increased $\epsilon_d$/DAC.

Second, the modes of the system are not necessarily static in frequency with different driving conditions, no matter how much we would like them to be. Pump detuning $\gamma_d$ to optimize the maser at a particular $\Phi_{total}$ is not constant for all $\epsilon_d$. This can be attributed to mode heating and shifting with changes to photon number in each oscillator. Sweeping $f_d$ is the most efficient way to find the conditions needed in the presence of shifting.

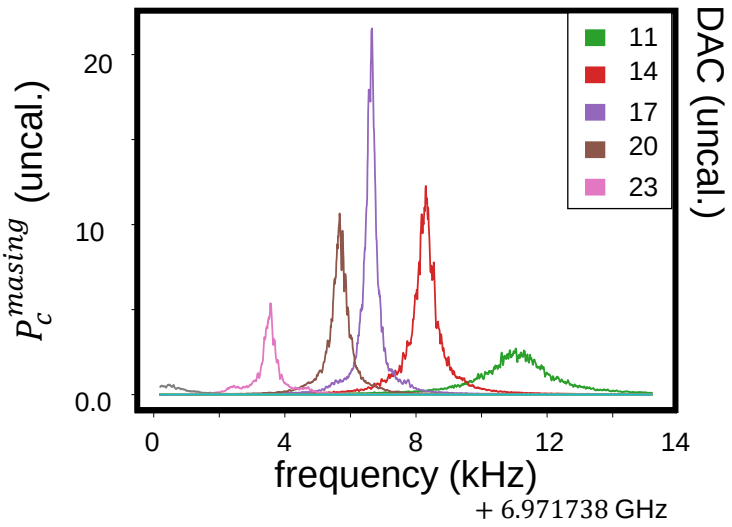


Figure 75: **Masing vs. DAC: fixed $f_d$, $\Phi_{ext}$** At a fixed SNAIL bias, qubit bias, and pump frequency, we change the DAC. The maser becomes 'better': gets brighter (higher in power output) and narrower (smaller bandwidth in frequency space) for increased DAC until 17 A.U., before getting 'worse' at higher DAC. This is likely because the pump becomes detuned with increased drive power and photon number.

These results did not produce what we expected. The light emitted by the cavity varies greatly in how bright and narrow it is compared to the 'natural' response of the cavity $\Gamma_c$, shown in Fig. 59(b). We had expected a small subset of conditions that would produce a good maser, at the predicted bias conditions and pump frequencies. Looking at the bias and drive conditions that produced the most promising results, this caused us to reevaluate the experiment. The broadened search of the large parameter space produced many 'viable' masers, but it was not apparent what made some better than others.

One search was amongst different SNAIL bias conditions, shown in Fig. 72(a, c). As long as the qubit's population is inverted with a three-wave mixing term when the qubit is near resonance with the cavity, we considered it a candidate for masing. This lead us to trying near $f_s = 5.0$ and 6.0 GHz. At all of these SNAIL frequencies, the sum frequencies also

do not collide with other known processes and are well within the pass band of our room temperature electronics. Surprisingly, moving the SNAIL away from 5.5 GHz produces interesting, sometimes better, masers with $f_s = 5.76$ GHz in Fig. 73 showing our narrowest and brightest maser results.

#### 5.4.3.2 Time Resolved Masing

The spectrum analyzer is a useful tool to find the maser output when we do not know its exact frequency at the start of an experiment. This is well illustrated by the variation in frequency center along the x-axis of Fig. 75. However, if we know what the steady state solution for the maser looks like, we can trace out the timed dynamics by digitizing the cavity's output. From time domain measurements of the maser, we can understand its decay better. This requires an exact knowledge of the output frequency $f_c^{\text{masing}}$ in order to down convert this frequency and have the ADC process data at the correct frequency. See Fig. 66 for the room temperature electronics setup used.

To digitize the masing cavity's output, we first measure the mode on the spectrum analyzer with fine frequency precision at a particular set of driving conditions. We find the frequency of the central peak and set our digitizing generator to $f_c^{\text{masing}} - 90$ MHz. Our digitizer is set to sample at 90 MHz, so the signal it processes must be exactly at 90 MHz as well. We use an IR mixer to reach this, feeding the RF port with the cavity's signal at $f_c^{\text{masing}}$ and the LO with $f_c^{\text{masing}} - 90$ MHz, converting the IF to 90 MHz. The digitizer or ADC on the QICK ZCU111 board samples every 2.6 ns and generates a set of I and Q points for every measurement. This data is acquired with a digital signal processing algorithm on the FPGA. Every 2.6 ns, we learn about the state of the maser, both amplitude $A_c^{\text{masing}}$ and phase $\phi_c^{\text{masing}}$. Figure. 76 shows IQ-plane histograms from windows of data collection times that are short compared to maser coherence time.

This is exciting because we now can understand maser evolution on time scales much shorter than its decoherence time. We can watch it take a random walk in the IQ plane, as a coherent light source, before eventually becoming incoherent due to phase noise, see Fig. 77. This is measured as the point at which the random walk forms a complete ring in

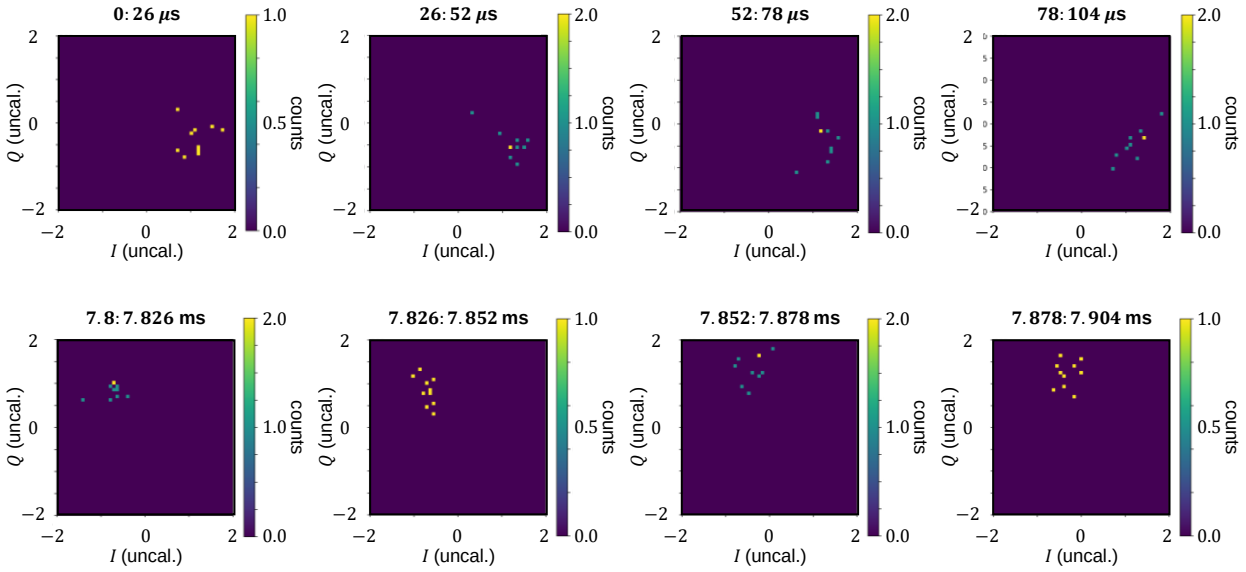


Figure 76: **The maser's output on short time scales** We can watch the maser evolve every 2.6 ns by digitizing its output. Plotted here are snapshots of the maser every 10,000 shots. In each histogram, the I and Q coordinates of the digitized signal are counted for the previous 26 $\mu$s and reset in each panel.

the IQ plane, when we can no longer verify its path compared to its starting point. This is provided the amplitude of the maser's output is stable and only the phase or frequency is changing with time, which we do see as the ring has constant radius. Through this method, we can measure the two-time correlation function:

$$G(t) = \langle c^\dagger(t')c(t)\rangle \sim e^{-i\omega_c|t'-t|} \tag{89}$$

which tells us how points at time $t'$ compare to those at time $t$. In our model, it follows an exponential decay. From $G(t)$ we can extract a coherence linewidth. The value from the time evolution method should match that of the steady state frequency measurement, but it can show us the maser with finer coherence on shorter time scales compared to its long-time solution.

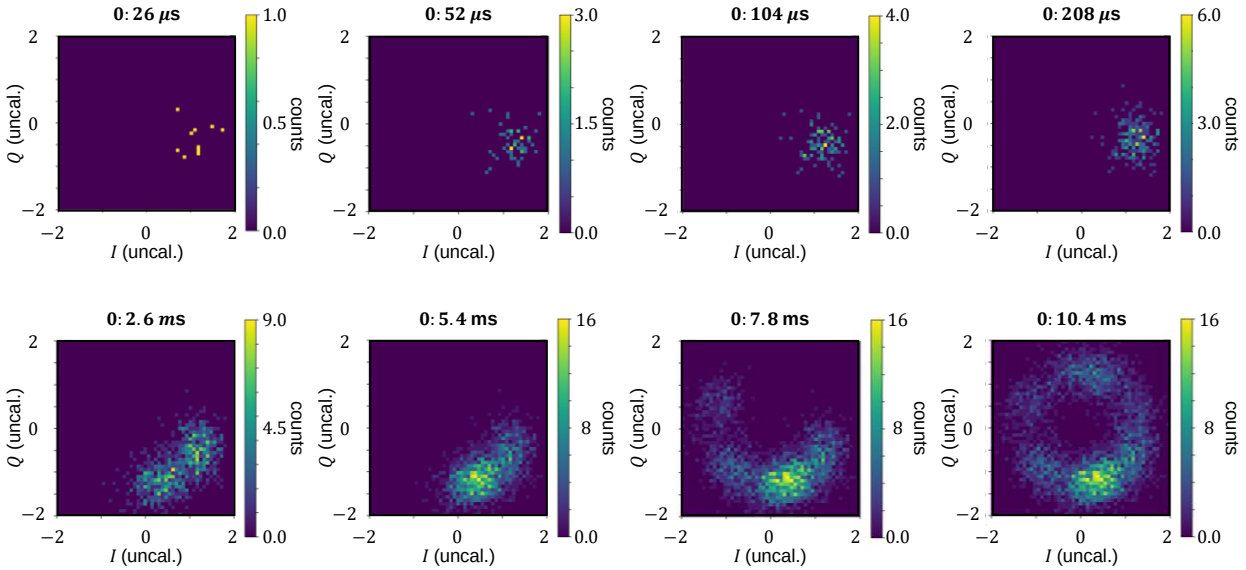


Figure 77: **The maser's output on long time scales** The output of the maser tracked cumulatively over time. The maser evoloves around the IQ plane, taking a random walk before diffusing out to a full ring.

The minimum value we measure for the maser linewidth is

$$\frac{\Gamma_c^{\text{masing}}}{2\pi}(\text{minimum}) = 57.67 \text{ Hz!} \tag{90}$$

As a reminder, the cavity has a bandwidth of $\frac{\Gamma_c}{2\pi} = 10 - 25$ kHz when measured on the VNA without the masing process. This is over $400\times$ the decrease in $\Gamma_c^{\text{masing}}$ vs. $\Gamma_c$, achieved by indirectly putting photons into the cavity through a population inverted, artificial atom transmon. It's a maser!

#### 5.4.3.3 Maser Photon Number

As of now, we do not know the lower limit on maser bandwidth for our experiment. Are we halted by the standard quantum limit on laser linewidth or some other physics of the transmon and/or SNAIL? Is it the stability of our control electronics? The missing piece of Eq. 88 is photon number $\langle n \rangle$, which would tell us how close we are to $\Gamma_c^{\text{masing}}(STL)$. Measuring photon number in strong coupling resonant systems in cQED is difficult, but possible in the dispersive regime with Stark shifting the transmon frequency by $\chi_{qc}$ for every photon number in the cavity using the methods developed in Ref. [30]. We can tune the qubit out of resonance with the masing cavity to increase their cross-Kerr $\chi_{qc}$ to perform this QND measurement of cavity occupation. While these photons will be excited in the cavity through direct driving, we can use this method as a proxy for the photons generated in the masing process. Using the dispersive measurement technique, we can get its input drive strength vs. $\langle n \rangle$. Then when we are masing, we can correlate its pump amplitude to the photon number associated with the cavity having the same input strength.

Unfortunately, this measurement scheme did not work for our experiment. Reference [30] increases the drive power on the cavity while performing qubit spectroscopy. This makes the spectroscopy peaks form a Poisson distribution for a coherent state and Bose-Einstein distribution for a thermal state, allowing us to assign each peak of shifted qubit frequency to a particular photon number. Our $\frac{g_{qc}}{2\pi} \leq 1$ MHz makes it difficult to find a detuning $\Delta_{qc}$ that separates each shifted spectroscopy peak from one another. We cannot fit the spectroscopy peak to any distribution that provides a meaningful approximation of photon number.

The ring formed in the IQ plane (Fig. 77) could also be used to calculate photon number in a masing cavity, if we know the noise temperature of the output chain. The radius of the ring tells us the average coherent amplitude $A_c^{masing} = \sqrt{\bar{N}}$. This measurement must

be calibrated. The maser's output at the base of the fridge goes through lossy elements like cables, circulators, and filters, and also through a series of amplifiers: a TWPA at 20 mK, a HEMT at 4 K, and a low noise amplifier at 300 K. This means the amplitude we measure, after this chain of microwave components, is higher than that at its direct output. Therefore this method is unreliable without proper calibration of the amplifier chain.

Finding good maser points has required combing through a large parameter space and finding combinations of conditions that produce a bright and narrow maser. We had expected masing via the purely three-wave parametric pump to invert the qubit to $|e\rangle$ by driving at $f_s + f_{q,ge}$ and for the qubit's $|g\rangle \leftrightarrow |e\rangle$ transition to resonantly couple with the cavity. However, in searching all degrees of freedom in our circuit, we have discovered other (sometimes better) masing points. I will now discuss the more curious behavior of our experiment, highlighting the versatility of our system featuring the principles of cQED.

#### 5.4.3.4 Other Qubit Transitions

Recalling our single tone spectroscopy sweep on the masing cavity vs. $\Phi_{ext}$, we found a second and third avoided crossing (Fig. 60), where the qubit's $f_{gf/2}$ and $f_{ef}$ each cross with the cavity (Fig. 62). Surprisingly, these points often make for a brighter, narrower maser! The $f_{ef}$ crossing is simple to understand under a generic three-wave mixing term $\propto s^\dagger q^\dagger$ because if the qubit is in $|e\rangle$ and then heated from there to $|f\rangle$, the decay from $|f\rangle \rightarrow |e\rangle$ could reasonably couple to the cavity. This transition's coupling rate $g_{qc,ef} \ll g_{qc,ge}$ so the rate structure $\kappa_s \gg \Gamma_{ge}^p > g_{qc,\text{effective}} \gg \Gamma_c$ of Eq. 85 is boosted with lower $g_{qc,\text{effective}}$. What does not fit our model is the $f_{gf/2}$ crossing.

For a harmonic oscillator, and the weakly anharmonic transmon, the transition $|g\rangle \leftrightarrow |f\rangle$ is a two photon transition. Our qubit operator in our simple Hamiltonian model, $q$ represents a single photon. Only one $q$ is involved in the SNAIL-qubit parametric heating process and the Jaynes-Cummings qubit-cavity direct exchange. This means a total of three photons are involved in the process, one $s$ for pumping, one $s$ for the SNAIL's dynamics, and $q_{ge}$. Therefore the addition of $q_{ef}$ does not add up. In many experiments, varying $\epsilon_d$, $f_d$, $\Phi_{total}$, and $f_s$, we see the maser narrower and brighter than the point involving only the $f_{ge}$ frequency.

We are still actively searching for an explanation for this phenomenon.

#### 5.4.3.5 SNAIL Kerr

Good masing was also produced when the SNAIL was biased with substantial fourth order nonlinearity. Our model for the parametric heating process:

$$H_{sq} = g_{\Sigma}(s^{\dagger}q^{\dagger}e^{-i\phi_d} + sqe^{i\phi_d}) \tag{91}$$

only involves three wave mixing and is achieved by biasing the SNAIL to a $\Phi_{total}$ that maximizes $g_3$ and brought its even order coefficients towards zero. The bare SNAIL acts as an effective harmonic mode. However, we found that when the SNAIL is brought to a flux condition that yields a self-Kerr term for the SNAIL, $K_{ss}$, our SNAIL is now more 'transmon-like' with an anharmonic mode structure. Now the total effective masing Hamiltonian takes the form:

$$H_{\text{masing, total}} = g_{\Sigma}(s^{\dagger}q^{\dagger}e^{-i\phi_d} + sqe^{i\phi_d}) + g_{qc}(q^{\dagger}c + qc^{\dagger}) - \frac{\alpha_q}{2}q^{\dagger}q^{\dagger}qq - \frac{K_{ss}}{2}s^{\dagger}s^{\dagger}ss \tag{92}$$

We find that the maser works well at these conditions, away from $K_{ss} = 0$, because it helps keep the SNAIL mode cold. This behavior was unexpected. Our three-wave drive should only at most put one photon in the SNAIL before it decays at leading rate $\kappa_s$. The regeneration rate $g_{\Sigma_{s,ge}}$ is limited by $\kappa_s$, so the process can only go as fast as the SNAIL decays in order to repump the ratchet towards target state $|0, e, n\rangle$. If the SNAIL is anharmonic, our parametric pump only excites the SNAIL within its $|0\rangle \leftrightarrow |1\rangle$ manifold, and therefore lets us repopulate the qubit faster. These conditions do require greater detuning in the pump frequency $\gamma_d$ which we attribute to Kerr-shifting and the AC Stark Effect. Additionally, we are not driving a four-wave parametric process with the SNAIL, but rather using the SNAIL for three-wave mixing and its always-on anharmonic self-Kerr term.

These unplanned behaviors can be modeled numerically. Our initial model in Sec. 5.1 left out SNAIL Kerr and did not account for multiple qubit-cavity crossings with different $g_{qc,i,i+1}$. After taking this data, which we found phenomenologically, we went back to QuTiP to try justifying what we found. Using a full numerical model, without any approximations, we

diagonalize and solve the master equation for a transmon qubit with fourth order nonlinearity $\frac{\alpha_q}{12}q^\dagger q^\dagger qq$ as in Eq. 79, coupled to an originally linear cavity and a SNAIL with third and fourth order nonlinearity of the form $g_3(s+s^\dagger)^3 + g_4(s+s^\dagger)^4$. The results in QuTiP with Eq. 92 more closely match our measured data than the initial model, highlighting the ways that approximations can obfuscate the true behavior of our circuits.

#### 5.4.3.6 Room Temperature Stabilization

Throughout this chapter, I have described our search for pump and bias conditions that induce masing. However we found that these conditions were not always consistent with time. Often we would return to the same conditions at a later time, within the same cooldown, and find that the maser's output behavior was not even remotely close to what it had been. This can be partially attributed to qubit frequency drifting vs. time. If the qubit changes frequency, it effectively induces an unknown detuning on the pump frequency because we cannot measure the qubit directly to detect this frequency shift while it is used in the masing process. We could take measures to reduce qubit dephasing, including reducing the size of the SQUID's Josephson junction loop, but unfortunately cannot completely eliminate it. It also can be attributed to unstable control and readout electronics.

At room temperature our drive and readout circuit consists of the DAC, the ADC, the spectrum analyzer, current source, generators, amplifiers, filters, and mixers seen in Fig. 66. All of these components must a) agree in frequency and b) remain stable in their output or signal passing with time. All components, when possible, are locked to the same 10 MHz Rubidium frequency standard so the generator and spectrum analyzer 'agree' on what a Hertz is. Additionally, we took great care to stabilize the temperature of every component so their output in the entire circuit is consistent.

The SignalCore generators, amplifiers, mixers, and filters were all bolted to a rack mount box with optical board inside, and the box was insulated with Styrofoam [93]. Inside the box was a temperature sensor read through a Raspberry Pi, and outside the box is a water cooled Peltier cooler. We set the temperature that we want the box to be inside, and the Pi uses a PID loop to control the cooler, which is temperature controlled with chilled water. We

can track the output of the drive line vs. time, finding it stable to within 1% over roughly an hour. This new generation of stabilizing electronics was built with the aid of my colleagues Boris Mesits and Gaurav Agarwal.

As a physicist I would like all of my problems to be fixable at 300 K and my results to be reliable at 20 mK. This is tremendously helpful in understanding our experiment; is the behavior we see because of fixable control and readout inconsistencies, or due to interesting quantum effects? Stabilizing the temperature of our components outside of the fridge is our best shot at uncovering the quantum.

## 5.5 Maser Outlook and Next Steps

Through this chapter, I have shown our work on building a maser with linear inter-element couplings using superconducting quantum circuits. We can make light come out of a masing cavity that was not directly excited. This light is narrower and brighter than when we probe the cavity directly.

In comparison to the bath engineering project of Chap. 4, this project calls for similar requirements in circuit parameters and only uses a single parametric drive. We could not have performed this maser experiment without having first understood the SNAIL-transmon coupling schemes that produce various thermalized transmons. The maser proved a great challenge because there are many moving parts. Not only does every mode shift with the various bias and drive conditions, but the output of the experiment was almost never where we thought it would be.

We still have some open questions for our maser experiment. We must calibrate for photon number output of the cavity when masing to compare the masing we achieve to the standard quantum limit on maser linewidth. We also need to predict the detuning $\gamma_d$ needed to optimize masing at chosen drive and bias conditions. Additionally, the frequency at which we digitize the cavity's output is not precise enough.

When we digitize the maser, we first measure its steady state on the spectrum analyzer, fit the peak's central frequency, and then set that as the mixer's LO frequency with a finite

single sideband. While we collect this data, enough time passes that the maser undergoes a phase decoherence process in which its frequency changes. Ideally we could set its output to a known value. This process is called 'Injection Locking,' where a nearby, narrow tone is sent in and the maser would 'lock' to this second tone and oscillate at the same frequency and with a narrowed linewidth. This is not only seen in lasers/masers, but also in classical systems: two out-of-sync pendulums suspended from the same beam will eventually find their way to matched resonance.

Once these topics are addressed, we can calculate how close our maser is to matching the Schawlow-Townes limit. The theory proposal that inspired this experimental work in Ref. [2] shows a $1/\langle n \rangle^2$ improvement in linewidth with the introduction of non-linear coupling elements between the atom and cavity, and the cavity and output, shown as the bottom 'ABOCC' option in Fig. 21. The 'Approximately Bare Operator Coupling Circuit' proposed in this work is feasible in the lab, suggested as an RF SQUID and $\pi$-junction. The maser built in this thesis has taught us how to design, measure, and control a maser with nonlinearity in its artificial atom, but not yet in its couplings. We learned how to use nonlinear parametric mixing to invert a nonlinear transmon. The addition of more nonlinearity will introduce more degrees of freedom that must be characterized and conquered, but this flexible circuit has shown us that with enough manipulation of its variables, even a frequency shifted, low coherence transmon can make a cryogenic light source.

## 6.0 Thesis Conclusions, Outlook, and Perspectives

This thesis details the work of two major experiments. First, we built a controllable qubit-bath coupling for transmons with their microwave environment. This was achieved with parametric three-wave mixing to heat and cool the transmon. We controlled the rates of qubit transitions between neighboring excitation states, as well as the final probabilities of finding the qubit in a particular state. Single parametric processes allow us to control a single, uni-directional transition, and multiple processes allow us to control multiple transitions. The results from this project, plus greater explanation of the tunable chemical potential, are described in our paper, Ref. [72].

This level of control provides great flexibility in designing quantum circuits. We can adjust the coupling of qubits to other elements and to their environment by modulating parametric couplings with microwave drives. This means for any combination of drives at $f_{\Sigma_{s,\ i,\ i+1}} = f_s + f_{q,\ i,\ i+1}$ and $f_{\delta_{s,\ j,\ j+1}} = f_s - f_{q,\ j,\ j+1}$, we choose $\Gamma^p_{i,\ i+1}$ and $\Gamma^p_{j+1,\ j}$. These parametric rates are the effective transition rates observed as the addition of native rates plus any parametrically driven processes.

We showed a great enhancement of rates for a single transmon, coupled to one cavity and one SNAIL. This scheme can also be extended to include more qubits and cavities. In systems with two qubits, Bell states can be created with entanglement. Imagine a scenario with two transmons, on resonance with one another so $\Delta_{q_a,\ q_b} = 0$ for bare frequencies $f_{q_a}$ and $f_{q_b}$. Each Bell state

$$\left|\Phi^{\pm}\right\rangle = \frac{1}{\sqrt{2}}(|g,g\rangle \pm |e,e\rangle) \tag{93}$$

$$\left|\Psi^{\pm}\right\rangle = \frac{1}{\sqrt{2}}(|g,e\rangle \pm |e,g\rangle) \tag{94}$$

in the basis $|q_a,\ q_b\rangle$ has a unique frequency thanks to mode hybridization and transmon anharmonicity. The eigen spectrum of the system will have unique splittings between levels, shown on the left of Fig. 78, and so our parametric heating and cooling processes can be individually driven at non-degenerate pump frequencies. We can also control the population probabilities of each, altering the coefficient for each ket in Eqs. 93, 94 and thus our ability

to heat and cool within a complicated two-qubit manifold. This scheme requires only one qubit to be coupled directly to the SNAIL, and that qubit coupled to both its own cavity and a secondary qubit-cavity system. On the right of Fig. 78 the heating process is shown, but this same logic can be applied to parametric cooling and any combination of the two.

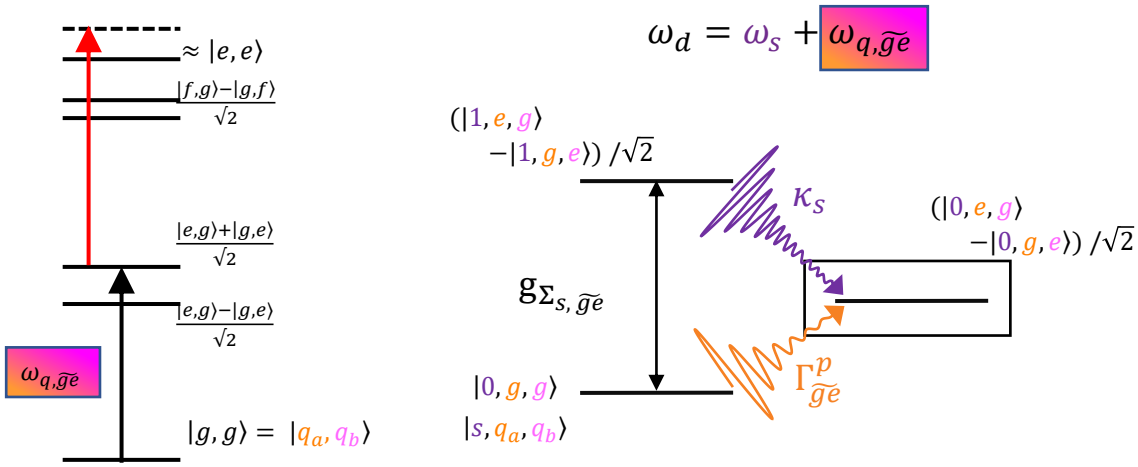


Figure 78: **Bath engineering for multiple qubits** The eigen energy spectrum on the left shows how two transmons with $\Delta_{q_a,\ q_b} = 0$ will rehybridize to have an anharmonic dressed level structure. The $|\Psi^{\pm}\rangle$ lowest energy states are distinct, and the difference of differences between all other levels are unique, allowing us to parametrically pump for specific state transition rates. On the right, we can apply the parametric process at rate $g_{\Sigma_{s,\tilde{ge}}}$ for this new 'ground to first excited' transition.

The ability to set qubit(s) in particular relaxation states is greatly useful for quantum simulations. We understand and turn all of the controls for our local, small quantum system in the laboratory, which varies the in situ relaxations of our qubit. This can be used to study larger, more complicated quantum models where we do not have such levels of control. In order to simulate a system with advantage over classical supercomputing or one that is inherently quantum mechanical in nature, we need to model the behavior of quantum states with variable probabilities or create admixtures of states that form to the problem at hand [106]. Our experiment does exactly this- we control how states are created and what

they decay to, without destroying relaxation to other states.

Our work is unique because our heating and cooling processes are smoothly varying with respect to time. When the pump is turned off, the qubit freely evolves and tends towards the ground state, or whatever state is preferred for its physical temperature. When the pump is on for increased time, as seen in Figs. 37, 41 for single processes and Fig. 44 for multiple processes, the qubit takes a steady exponential population probability vs. time path. This makes its effect tractable and prevents potential unwanted behavior from rapid state switching.

Additionally, our bath engineered qubit sees a lossy SNAIL mode. There are no uniquely specified frequencies or requirements on our pump or mode configuration. This provides flexibility in project design and allows us to implement such a coupling scheme without disrupting other circuit elements or processes. In our work, combinations of parametric heating and cooling require (a) a transmon, (b) a SNAIL with decay $\kappa_s$ greater than its total effective parametric process rate, and (c) the ability to drive frequencies within a broad band of values near SNAIL and qubit sum and difference frequencies. We do not require our loss channel to be narrow band to collect our 'thrown away' light [60]. We do not require pump frequencies at very specific spacings [66]. We don't even require our qubit to be that cold [107]. Our drives can be applied within a large detuning of $f_d = f_s + f_q + \gamma_d$, shown in Figs. 38, 42, and 45. Our pumps can be applied separate or together and have detunings on order of the SNAIL's bandwidth and still produce the desired effect. As long as our pump does not accidentally cause some other process, it can be driven. And our qubit can tolerate moderate heating because our parametric drive can rapidly cool it! We have built a system that is straightforward to implement with great payoff: qubit admixture states can be quickly created and maintained with a broad, re-configurable parametric three-wave mixer.

The second project in this thesis is really a proof-of-application of the first. Parametric drives can heat the transmon to a population inverted state, making it a candidate for single-atom masing with a high Q cavity. The inverted atom exchanges energy with the cavity,

repeatedly, because we maintain the hierarchy of rates

$$\kappa_s \gg \Gamma_{ge}^{p} > g_{qc,\text{effective}} \gg \Gamma_c \tag{95}$$

through tuning our circuit into the correct parameter space. The cavity must always be fed another photon by the qubit before it decays, requiring the qubit to always be populated, requiring the qubit inversion rate to be less than the SNAIL's decay rate. This prevents the maser ratchet in Fig. 23 from going backwards, or rather from light exchanging in the direction we do not want it to.

With this SNAIL-qubit-cavity coupling scheme, we achieve masing with great success at a number of bias and drive conditions. The output of the maser is significantly narrower and brighter than it is when directly driven, and the frequency response of the output light is also different than the cavity's VNA response. This opens up use cases for this experiment. We can make the cavity produce light within a window of frequencies, at an output amplitude and linewidth that we control with the strength and bias of our parametric drives.

This means that if a particular application requires a specific frequency, amplitude, and/or linewidth cavity, it can be created in situ. Fabrication inconsistencies and mode shifting due to drives and hybridization mean that we do not always have the level structure needed for particular experiments. However, those values can be created with adjusted drives and biasing.

The maser shown in this thesis will not replace manufactured signal generators. Microwave signal generators, at room temperature, can be bought for under $\$5,000$ with excellent frequency and phase stability. My maser is coherent for milliseconds at best, and has required countless hours of work and study. My PhD was not meant to produce a commercially viable product, but rather to study the power of parametric mixing and superconducting qubits as a flexible platform on which some interesting physics can be built.

The maser project shows how variability in circuit input AND output can be a daunting reality, however it highlights the richness we have access to within the circuit QED platform. I was able to make an artificial atom with the frequency and couplings I wanted, masing through a cavity I precisely designed, and apply broadband drives through an in situ, reconfigurable parametric multi-wave mixer. If one element wasn't to my liking, I could swap

it out with a quick trip to the nanofab. And this flexibility does not only apply to building a maser, but rather to any circuit one wishes to design using a superconducting RF modality.

If anything is to be taken away from this thesis, it is how powerful a tool three-wave mixing is. In both projects, I have coupled a fragile transmon, whose lifetime we would like to preserve, to a lossy SNAIL that gets driven as strongly as we can. The lifetime of our qubit remained modest in the bath engineering project, and stable enough to repeatedly probe and pulse. Lifetimes were quite low in the maser project, but likely due to phase noise rather than parametric driving. We were still successful in achieving our goals for both projects, showing how our transmons were not destroyed by strong couplings to the dump mode. This work introduced loss as one of the key components to realize our target states. We need the SNAIL to rapidly lose its photon(s) in order to reset the protocol. This is unlike other SNAIL-qubit coupling implementations which use only the parametric mixing properties of the SNAIL for gate operations.

Initially, the maser project was planned to be built with two cavities with a frequency tunable qubit in between them, which would be pumped at $f_d = f_{q,\ gf/2}$, and the cavity at $f_{ef}$ would act as the dump mode. This idea was replaced with the one implemented in this thesis because we realized three-wave couplings could make the process possible without continually Rabi driving the qubit or relying on resonance conditions to remove unwanted excitations. Generally, three-wave parametric couplings have become a mainstay of the Hatlab because they are flexible, can be turned on and off in situ, and provide opportunities to study interesting quantum information effects. Three-wave mixing is central to our lab's efforts in building quantum limited amplifiers [62], noise-reduced readout [108], performing qubit readout with a SNAIL [38], realizing modular multi-qubit gates [96], and building increasingly complicated quantum machines [109]. We have also used parametric multi-wave mixing to perform novel qubit gates without involving the SNAIL [93].

The work in this thesis is limited by our inferred knowledge of the circuit elements involved in the parametric processes. When the qubit is nearly on resonance with the masing cavity and its inverted population is feeding the cavity, we cannot measure it. The masing cavity is meant to hold onto its photons and not be read out, and in the strong coupling regime it would not give us useful information about the qubit other than the Rabi exchange

rate. The readout resonator cannot distinguish qubit from masing cavity state, so we cannot use that. Instead we perform qubit lifetime and inversion rate measurements at the bias conditions nearby ($|\Delta_{qc}| \gg g_{qc}$) as a system diagnostic.

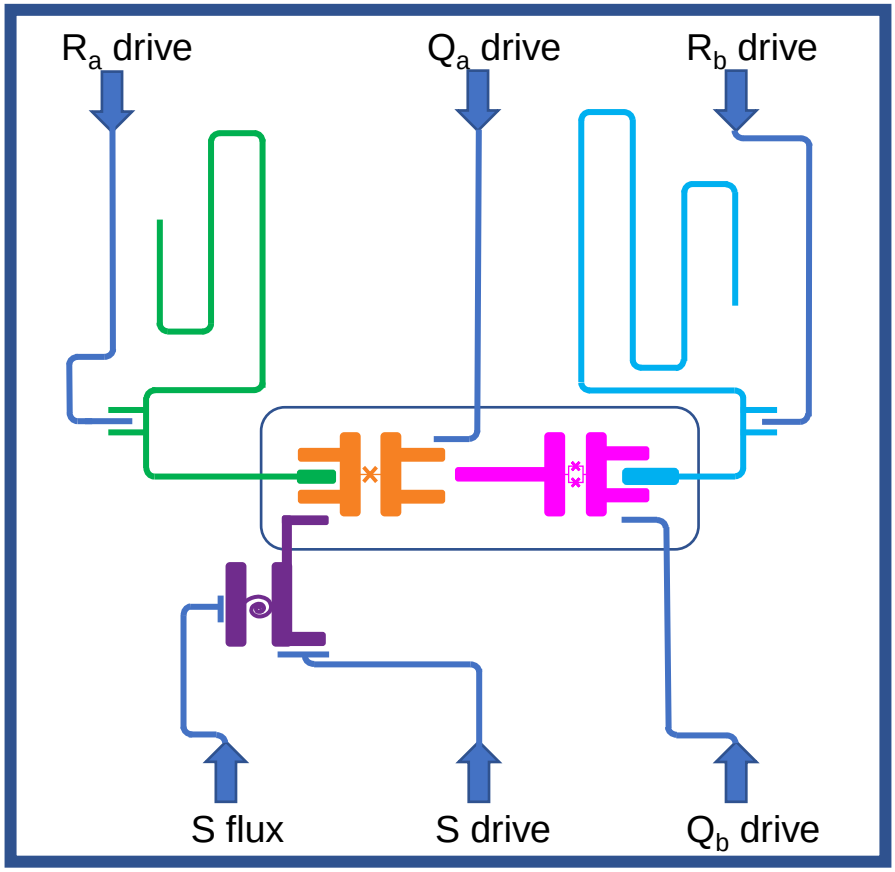


Figure 79: **Multi-qubit circuit** A mock circuit layout for a 2-qubit, 2-cavity realized in a 2D architecture. The qubit directly coupled to the SNAIL is fixed frequency, while the other is a frequency tunable SQUID. Each qubit is coupled to its own cavity. Such a layout can be used in an extension of both projects presented in this thesis. We can realize the Bell State stabilization of Fig. 78 or a two-qubit maser. In both scenarios, only one SNAIL is used as the generator of the parametric ratcheting process. This type of 2D circuit is more readily re-configured and more compact than the designs presented in Chaps. 4 and 5.

This can cause problems because we are working with limited information. We do not

know, with certainty, the frequency of the SNAIL or qubit mode separately in the presence of the strong parametric pump. We are not able to measure any shifting that occurs with high photon number occupation, physical heating, or frequency drifting due to noise and decoherence, and therefore can only make strong guesses as to the pump frequency and output frequency of the maser. This has taken more time to search our parameter space and lead us to potentially hunting for bias conditions that might not produce the same results some time later. In hindsight, we could use more parametric mixing to probe our system. We could apply a transmon cooling tone to the SNAIL at the end of each experiment, which would empty both the SNAIL and qubit. This would tell us the state of the SNAIL due to the qubit inversion process; if the qubit is cold then so is the SNAIL, following the logic of Sec. 3.1.4.

Bath engineering is a growing field as quantum error detection and correction increases its scope, and more sophisticated algorithms for quantum simulation are designed. Future work can build upon this thesis by including more of each circuit component, as shown in Fig. 79. More qubits to thermalize, more cavities to store and readout, and more SNAILs to perform increasing numbers of inter-elemental parametric couplings. One could readily insert a lossy SNAIL to a system with one or more qubits and apply parametric interactions to create the

Figure 80: **Schrödinger's Hat**

qubit states desired. The output of a cryogenic maser can be fed as a light source to another cavity or qubit, especially if they call for very specifically tuned input frequencies, which we can tune the maser to produce with varying bias and driving conditions. The circuit drawing in Fig. 79 is one way we can expand upon the projects presented in this thesis. We could heat and cool Bell states by tuning the qubit's on resonance with one another, and drive our parametric heating and cooling plus engineered loss process through the SNAIL. We could also use this circuit as a maser where the qubits' joint light is what feeds the masing cavity. This provides an opportunity for entanglement studies and further propagation of quantum states as needed in quantum simulations.

The act of measuring a quantum system forces probabalistic outcomes. The entanglement of our qubits with our measurement apparatus is unavoidable. This thesis shows how we can variably control the probabilities of measurement outcomes. We cannot remove the poison that kills Schrödinger's cat, but rather we can design how quickly and with what probability it does. I have shown how I can manipulate qubit and cavity states into what I want them to be, almost instantaneously, with a handful of microwave drives. Throughout my PhD, I have worked on harnessing these parametric processes to find a final, steady state solution of my choosing. This has been done in spite of, or in addition to, any losses and native rates of the circuit. Lastly, I have realized and measured short scale evolution of complicated state configurations for bath engineered qubits.

## Bibliography


[1] M Hafezi, P Adhikari, and JM Taylor. Chemical potential for light by parametric coupling. *Physical Review B*, 92(17):174305, 2015.

[2] C Liu, M Mucci, X Cao, M V G Dutt, M Hatridge, and D Pekker. Proposal for a continuous wave laser with linewidth well below the standard quantum limit. *Nature Communications*, 12(5620), 2021.

[3] M A Nielson and I L Chuang. *Quantum Computation and Quantum Information*. Cambridge University Press, 2000.

[4] J von Neumann. *The Mathematical Foundations of Quantum Mechanics*. 1932.

[5] A. Montanaro. Quantum algorithms: an overview. *npj Quantum Information*, 2(15023), 2016.

[6] R P Feynman. Simulating physics with computers. *International Journal of Theoretical Physics*, 21:467–488, 1982.

[7] D P DiVincenzo. The physical implementation of quantum computation. *Fortshritte der Physik*, 48(9-11):771–783, 2000.

[8] A Blais, R-S Huang, A Wallraff, S M Girvin, and R J Schoelkopf. Cavity quantum electrodynamics for superconducting electrical circuits: An architecture for quantum computation. *Phys. Rev. A*, 69(062320), 2004.

[9] T Connolly, P Kurilovich, C Boettcher, H Nho, A Z Ding, S Diamond, V Fatemi, and M H Devoret. Transmon readout in the large detuning limit – part 1 / 2: Design of the experiment. *March Meeting*, G47.00005, 2024.

[10] H Zhang, S Chakram, T Roy, N Earnest, Y Lu, Z Huang, D K Weiss, J Koch, and D I Schuster. Universal fast-flux control of a coherent, low-frequency qubit. *Phys. Rev. X*, 11(1):011010, 2021.

[11] J F Poyatos, J I Cirac, and P Zoller. Quantum reservoir engineering with laser cooled trapped ions. *Physical Review Letters*, 77(23):4728, 1996.

[12] M Mirrahimi, Z Leghtas, and U Vool. Quantum reservoir engineering and single qubit cooling. *IFAC Proceedings Volumes*, 46(23):424–429, 2013.

[13] J Koch, T M Yu, J Gambetta, A A Houck, D I Schuster, J Majer, A Blais, M H Devoret, S M Girvin, and R J Schoelkopf. Charge insensitive qubit design derived from the cooper pair box. *Physical Review A*, 76(4):042319, 2007.

[14] N E Frattini, U Vool, S Shankar, A Narla, K M Sliwa, and M H Devoret. 3-wave mixing josephson dipole element. *Applied Physics Letters*, 110(22):222603, 2017.

[15] Measuring and manipulating individual quantum systems. *The Nobel Prize*, 2012.

[16] IBM Quantum. Quantum roadmap. 2022.

[17] C S Smith. Top 10 quantum computing companies making change. *Forbes*, 2023.

[18] Quantum technology sees record investments, progress on talent gap. *McKinsey and Co.*, 2023.

[19] National quantum initiative supplement to the president's fy 2024 budget. 2023.

[20] S M Girvin. Circuit qed: superconducting qubits coupled to microwave photons. *Proceedings of the 2011 Les Houches Summer School on Quantum Machines*, 2014.

[21] B D Josephson. Possible new effects in superconductive tunnelling. *Physics Letters*, 1(7):251–253, 1962.

[22] D W Snoke. *Solid state physics: Essentail concepts*. Cambridge University Press, 2020.

[23] V Bouchiat, D Vion, P Joyez, D Esteve, and M H Devoret. Quantum coherence with a single cooper pair. *Physica Scripta*, 1998(165), 1998.

[24] Y Nakamura, Y A Pashkin, and J S Tsai. Coherent control of macroscopic quantum states in a single-cooper-pair box. *Nature*, 398:786–788, 1999.

[25] W E Lamb Jr and R C Retherford. Fine structure of the hydrogen atom by a microwave method. *Phys. Rev.*, 72:241, 1947.

[26] A I Braginski and J Clarke. *The SQUID handbook*. Wiley-VCH Verlag GmbH Co. KGaA, 2004.

[27] M Reagor, H Paik, G Catelani, L Sun, C Axline, E Holland, I M Pop, N A Masluk, T Brecht, L Frunzio, M H Devoret, L Glazman, and R J Shoelkopf. Reaching 10 ms single photon lifetimes for superconducting aluminum cavities. *Applied Physics Letters*, 102(19):192604, 2013.

[28] A Wallraff, D I Schuster, A Blais, L FRunzio, J Majer, M H Devoret, S M Girvin, and R J Schoelkopf. Approaching unit visibility for control of a superconducting qubit with dispersive readout. *Physical Review Letters*, 95(6):060501, 2005.

[29] E T Jaynes and F W Cummings. Comparison of quantum and semiclassical radiation theories with application to the beam maser. *IEEE Proceedings*, 51:89–109, 1963.

[30] D I Schuster, A A Houck, J A Schreier, A Wallraff, J M Gambetta, A Blais, L Frunzio, J Majer, B R Johnson, M H Devoret, S M Girvin, and R J Schoelkopf. Resolving photon number states in a superconducting circuit. *Nature*, 445:515–518, 2007.

[31] B R Johnson, M D Reed, A A Houck, D I Schuster, L S Bishop, E Ginossar, J M Gambetta, L DiCarlo, L Frunzio, S M Girvin, and R J Schoelkopf. Quantum non-demolition detection of single microwave photons in a circuit. *Nature Physics*, 6:663–667, 2010.

[32] K L Geerlings. *Improving coherence of superconducting qubits and resonators*. PhD thesis, Yale University, 2013.

[33] Backronym. *Wikipedia*.

[34] J D Teufel, T Donner, D Li, J W Harlow, M S Allman, K Cicak, A J Sirois, J D Whittaker, K W Lehnert, and R W Simmonds. Sideband cooling of micromechanical motion to the quantum ground state. *Nature*, 475:359–363, 2011.

[35] B J Chapman, S J de Graaf, S H Xue, Y Zhang, J Toeh, J C Curtis, T Tsunoda, A Eickbusch, A P Read, A Koottandavida, S O Mundhada, L Frunzio, M H Devoret, S M Girvin, and R J Schoelkopf. High-on-off-ratio beam-splitter interaction for gates on bosonically encoded qubits. *PRX Quantum*, 4:020355, 2023.

[36] N Bergeal, F Schackert, M Metcalfe, R Vijay, V E Manucharyan, L Frunzio, D E Prober, R J Schoelkopf, S M Girvin, and M H Devoret. Phase-preserving amplification near the quantum limit with a josephson ring modulator. *Nature*, 465:64–68, 2010.

[37] A Blais, A. L. Grimsmo, S. M. Girvin, and A Wallraff. Circuit quantum electrodynamics. *Reviews of Modern Physics*, 93(2):025005, 2021.

[38] Chao Zhou. *Superconducting quantum routers, modules, gates, and measurements based on charge-pumped parametric interactions*. PhD thesis, University of Pittsburgh, 2023.

[39] V V Sivak, N E Frattini, V R Joshi, A Lingenfelter, S Shankar, and M H Devoret. Kerr-free three-wave mixing in superconducting quantum circuits. *Physical Review Applied*, 11(054060):5, 2019.

[40] J Gambetta, A Blais, D I Schuster, A Wallraff, L Frunzio, J Majer, M H Devoret, S M Girvin, and R J Schoelkopf. Qubit-photon interactions in a cavity: Measurement-induced dephasing and number splitting. *Phys. Rev. A*, 74(4):042318, 2006.

[41] M Kjaergaard, M E Schwartz, J Braumüller, P Krantz, J I J Wang, S Gustavsson, and W D Oliver. Superconducting qubits: Current state of play. *Annual Review of Condensed Matter Physics*, 11:369–395, 2020.

[42] J Preskill. Quantum computing in the nisq era and beyond. *Quantum 2*, 2:79, 2018.

[43] P W Shor. Scheme for reducing decoherence in quantum computer memory. *Phys. Rev. A*, 52(4):R2493(R), 1995.

[44] E M Purcell, H C Torrey, and R V Pound. Resonance absorption by nuclear magnetic moments in a solid. *Phys. Rev.*, 69:37–38, 1946.

[45] J Clarke and F K Wilhelm. Superconducting quantum bits. *Nature*, 453:1031–1042, 2008.

[46] N F Ramsey. A new molecular beam resonance method. *Phys. Rev.*, 76:996, 1949.

[47] E L Hahn. Spin echoes. *Phys. Rev.*, 80:580–594, 1950.

[48] A P M Place, L V H Rodgers, P Mundada, B M Smitham, M Fitzpatrick, Z Leng, A Premkumar, J Bryon, A Vrajitoarea, S Sussman, G Cheng, R Madhavan, H K Babla, X H Le, Y Gang, B Jäck, A Gyenis, N Yao, R j Cava, de Leon N P, and A A Houck. New material platform for superconducting transmon qubits with coherence times exceeding 0.3 milliseconds. *Nature Communications*, 12, 2021.

[49] Y Sunada, S Kono, J Ilves, S Tamate, T Sugiyama, Y Tabuchi, and Y Nakamura. Fast readout and reset of a superconducting qubit coupled to a resonator with an intrinsic purcell filter. *Physical Review Applied*, 17:044016, 2022.

[50] C Wang, X Li, H Xu, X Li, J Wang, Z Yang, Z Mi, X Liang, T Su, C Yang, G Wang, W Wang, Y Li, M Chen, C Li, K Linghu, J Han, Y Zhang, Y Feng, Y Song, T Ma, J Zhang, R Wang, P Zhao, W Liu, G Xue, Y Jin, and H Yu. Towards practical quantum computers: transmon qubit with a lifetime approaching 0.5 milliseconds. *npj Quantum Information*, 8, 2022.

[51] S Ganjam, Y Wang, Y Lu, A Banerjee, C U Lei, L Krayzman, K Kisslinger, C Zhou, R Li, Y Jia, M Liu, L Frunzio, and R J Schoelkopf. Surpassing millisecond coherence in on chip superconducting quantum memories by optimizing materials and circuit design. *Nature Communications*, 15, 2024.

[52] P Patel and et al. Wispe. *In Prep*, 2024.

[53] S M Girvin. Extending superconducting qubit lifetimes: What's next? *Journal Club for Condensed Matter Physics*, 2021.

[54] D L Underwood, W E Shanks, J Koch, and A A Houck. Low-disorder microwave cavity lattices for quantum simulation with photons. *Physical Review A*, 86(2):023837, 2012.

[55] A A Houck, H E Türeci, and J Koch. On-chip quantum simulation with superconducting circuits. *Nature Physics*, 8(4):292–299, 2012.

[56] K W Murch, U Vool, D Zhou, S J Weber, S M Girvin, and I Siddiqi. Cavity-assisted quantum bath engineering. *Physical Review Letters*, 109(18):183602, 2012.

[57] M E Kimchi-Schwartz, L Martin, E Flurin, C Aron, M Kulkarni, H E Tureci, and I Siddiqi. Stabilizing entanglement via symmetry-selective bath engineering in superconducting qubits. *Physical Review Letters*, 116(24):240503, 2016.

[58] Y Lu, S Chakram, N Leung, N Earnest, R K Naik, Z Huang, P Groszkowski, E Kapit, J Koch, and D I Schuster. Universal stabilization of a parametrically coupled qubit. *Physical Review Letters*, 119(150502), 2017.

[59] R Ma, C Owens, A Houck, D I Schuster, and J Simon. Autonomous stabilizer for incompressible photon fluids and solids. *Physical Review A*, 95(4):043811, 2017.

[60] R Ma, B Saxberg, C Owens, N Leung, Y Lu, J Simon, and D I Schuster. A dissipatively stabilized mott insulator of photons. *Nature*, 566:51–57, 2019.

[61] P M Harrington, E J Mueller, and K W Murch. Engineered dissipation for quantum information science. *Nature Reviews Physics*, 4(10):660–671, 2022.

[62] T-C Chien, O Lanes, C Liu, X Cao, P Lu, S Motz, G Liu, D Pekker, and M Hatridge. Multiparametric amplification and qubit measurement with a kerr-free josephson ring modulator. *Phys. Rev. A*, 101(042336), 2020.

[63] E Kapit, M Hafezi, and S E Simon. Induced self-stabilization in fractional quantum hall states of light. *Physical Review X*, 4(3):031039, 2014.

[64] M D Reed, B R Johnson, A A Houck, L DiCarlo, Chow J M, D I Schuster, L Frunzio, and R J Shoelkopf. Fast reset and suppressing spontaneous emission of a superconducting qubit. *Applied Physical Letters*, 96(203110), 2010.

[65] K Geerlings, Z Leghtas, I M Pop, S Shankar, L Frunzio, R J Shoelkopf, M Mirrahimi, and M H Devoret. Demonstrating a driven reset protocol for a superconducting qubit. *Physical Review Letters*, 110(12):120501, 2013.

[66] J M Gertler, B Baker, J Li, S Shirol, J Koch, and C Wang. Protecting a bosonic qubit with autonomous quantum error correction. *Nature*, 590:243–248, 2021.

[67] N Ashcroft and N Mermin. *Solid State Physics*. Holt-Saunders, 1976.

[68] M Planck. *The theory of heat radiation*. Blakiston, 1914.

[69] C H Henry and R F Kazarinov. Quantum noise in photonics. *Reviews of Modern Physics*, 68(3):801, 1996.

[70] J Klaers, J Schmitt, F Vewinger, and M Weitz. Bose-einstein condensation of photons in an optical microcavity. *Nature*, 468(7323):545–548, 2010.

[71] J Klaers, J Schmitt, T Damm, F Vewinger, and M Weitz. Statistical physics of bose-einstein-condensed light in a dye microcavity. *Physical review letters*, 108(16):160403, 2012.

[72] X Cao, M Mucci, G Liu, D Pekker, and M Hatridge. Engineering a multi-level bath for transmon with three-wave mixing and parametric drives. *ArXiv*, (2407.21765), 2024.

[73] A Einstein. *On a heuristic point of view concerning the production and yransformation of light.* Annalen der Physik, 1905.

[74] N Bohr. On the constitution of atoms and molecules: I, xxxvii, lxxiii. *The London, Edinburgh, and Dublin Philosophical Magazine and Journal of Science*, 26(151, 153, 155), 1913.

[75] G N Lewis. The conservation of photons. *Nature*, 118(874-875), 1926.

[76] J P Gordon, H J Zeiger, and C H Townes. The maser—new type of microwave amplifier, frequency standard, and spectrometer. *Phys. Rev.*, 99:1264–1274, 1955.

[77] M O Scully and M S Zubairy. *Quantum optics.* Cambridge University Press, 1997.

[78] C Fabry and A Perot. Théorie et applications d'une nouvelle méthode de spectroscopie interférentielle. *Ann. de Chim. et de Phys.*, 7, 1899.

[79] C Liu. Theoretical investigation of photon manipulation for quantum computing and quantum information processing. *Doctoral Thesis*, 2020.

[80] H M Wiseman. Light amplification without stimulated emission: Beyond the standard quantum limit to the laser linewidth. *Phys. Rev. A*, 60(4083), 1999.

[81] A L Schawlow and C H Townes. Infrared and optical masers. *Phys. Rev.*, 112(6):1940–1949, 1958.

[82] O Astafiev, K Inomata, A O Niskanen, T Yamamoto, Y A Pashkin, Nakamura Y, and J S Tsai. Single artificial-atom lasing. *Nature*, 449(588–590), 2007.

[83] M C Cassidy, A Bruno, S Rubbert, M Irfan, J Kammhuber, R N Schouten, A R Akhmerov, and L P Kouwenhoven. Demonstration of an ac josephson junction laser. *Science*, 355(6328):939–942, 2017.

[84] S H Simon and N R Cooper. Theory of the josephson junction laser. *Physical Review Letters*, 121:027004, 2018.

[85] F Chen, J Li, A D Armour, e Brahimi, J Stettenheim, A J Sirois, R W Simmonds, M P Blencowe, and A J Rimber. Realization of a single-cooper-pair josephson laser. *Phys. Rev. B*, 90(020506(R)), 2014.

[86] S Ashhab, J R Johansson, A M Zagoskin, and F Nori. Single-artificial-atom lasing using a voltage-biased superconducting charge qubit. *New Journal of Physics*, 11(023030), 2009.

[87] J Q You, Y-X Liu, C P Sun, and F Nori. Persistent single-photon production by tunable on-chip micromaser with a superconducting quantum circuit. *Phys. Rev. B*, 75(104516), 2007.

[88] T J Baker, S N Saadatmand, D W Berry, and H M Wiseman. The heisenberg limit for laser coherence. *Nature Physics*, 17:179–183, 2021.

[89] S E Nigg, H Paik, B Vlastakis, G Kirchmair, S Shankar, L Frunzio, M H Devoret, R J Schoelkopf, and S M Girvin. Black-box superconducting circuit quantization. *Physical Review Letters*, 108:240502, 2012.

[90] H J Korsch, H-J Jodl, and T Hartmann. *Chaos*. Springer Berlin, Heidelberg, 2007.

[91] M D Reed. *Entanglement and quantum error correction with superconducting qubits*. PhD thesis, Yale University, 2013.

[92] C Macklin, K O'Brien, D Hover, M E Schwartz, V Bolkhovsky, X Zhang, W D Oliver, and I Siddiqi. A near–quantum-limited josephson traveling-wave parametric amplifier. *Science*, 350(6258):307–310, 2015.

[93] M Xia, C Zhou, C Liu, P Patel, X Cao, P Lu, B Mesits, M Mucci, D Gorski, D Pekker, and M Hatridge. Fast superconducting qubit control with sub-harmonic drives. *ArXiv*, (2306.10162), 2023.

[94] N E Frattini, V V Sivak, A Lingenfelter, S Shankar, and M H Devoret. Optimizing the nonlinearity and dissipation of a snail parametric amplifier for dynamic range. *Phys. Rev. Applied*, 10:054020, 2018.

[95] J-H Yeh, J LeFebvre, S Premaratne, F C Wellstood, and B S Palmer. Microwave attenuators for use with quantum devices below 100 mk. *J. Appl. Phys.*, 121, 2017.

[96] C Zhou, P Lu, M Praquin, T-C Chien, R Kaufman, X Cao, M Xia, R S K Mong, W Pfaff, D Pekker, and M Hatridge. Realizing all-to-all couplings among detachable quantum modules using a microwave quantum state router. *npj Quantum Information*, 9, 2023.

[97] Tzu-Chiao Chien. *Creating directional quantum-limited amplification using multiple parametric*. PhD thesis, University of Pittsburgh, 2020.

[98] S Lloyd. Universal quantum simulators. *Science*, 273(5278):1073–1078, 1996.

[99] C J Axline, L D Burkart, W Pfaff, M Zhang, K Chou, P Campagne-Ibarcq, P Reinhold, L Frunzio, S M Girvin, L Jiang, M H Devoret, and R J Schoelkopf. On-demand quantum state transfer and entanglement between remote microwave cavity memories. *Nature Physics*, 14(705-710), 2018.

[100] L Stefanazzi, K Treptow, N Wilcer, C Stoughton, C Bradford, S Uemura, S Zorzetti, S Montella, G Cancelo, S Sussman, A Houck, S Saxena, H Arnaldi, Agrawal A, H Zhang, C Ding, and D I Schuster. The qick (quantum instrumentation control kit): Readout and control for qubits and detectors. *Rev. Sci. Instrum.*, 93(4):044709, 2022.

[101] C Zhou and et al. *In Preparation*, 2023.

[102] Z K Minev, Z Leghtas, S O Mundhada, L Christakis, I M Pop, and M H Devoret. Energy-participation quantization of josephson circuits. *npj Quantum Information*, 7, 2021.

[103] C Axline, M Reagor, R Heeres, P Reinhold, C Wang, K Shain, W Pfaff, Y Chu, L Frunzio, and R J Schoelkopf. An architecture for integrating planar and 3d cqed devices. *Applied Physical Letters*, 109(042601), 2016.

[104] A Potts, P R Routley, G J Parker, J J Baumber, and P A J de Groot. Novel fabrication methods for submicrometer josephson junction qubits. *Journal of Materials Science: Materials in Electronics*, 12:289–293, 2001.

[105] A Wallraff, D I Schuster, A Blais, L Frunzio, R-S Huang, J Majer, S Kumar, S M Girvin, and R J Schoelkopf. Strong coupling of a single photon to a superconducting qubit using circuit quantum electrodynamics. *Nature*, 431:pages162–167, 2004.

[106] A J Daley, I Bloch, C Kokail, S Flannigan, N Pearson, M Troyer, and P Zoller. Practical quantum advantage in quantum simulation. *Nature*, 607:667–676, 2022.

[107] M Lucas, A V Danilov, L V Levitin, A Jayaraman, A J Casey, L Faoro, A Y Tzalenchuk, S E Kukatkin, J Saunder, and S E de Graaf. Quantum bath suppression in a superconducting circuit by immersion cooling. *Nature Communications*, 14:3522, 2023.

[108] G Liu, X Cao, T-C Chien, C Zhou, P Lu, and M Hatridge. Noise reduction in qubit readout with a two-mode squeezed interferometer. *Physical Review Applied*, 18:064092, 2022.

[109] E McKinney, M Xia, C Zhou, P Lu, M Hatridge, and A K Jones. Co-designed architectures for modular superconducting quantum computers. *International Symposium on High-Performance Computer Architecture*, 2023.